Brittle deformation and hydrothermal alteration in the Barra Velha Formation, Santos Basin, offshore Brazil

Rodrigo dos Santos Maia Corrêa, Bruno Carvalho, Estibalitz Ukar, Stephen E. Laubach, André L. S. Pestilho, András Fall, Toti Larson, Daniel Stockli, Lisa Stockli, Volker Lüders, Samuel Niedermann, and David A. Banks

ABSTRACT

The Barra Velha Formation is a prolific Aptian (Lower Cretaceous) oil and gas producer located in the Santos Basin, southeastern Brazilian coast. We used structural core description, petrography, geochemistry, and geochronology to show evidence from drill cores that the Barra Velha Formation was affected by several events of brittle deformation and interacting hydrothermal alteration. The U-Pb geochronology provides an age of ca. 116 Ma for depositional host rock calcites, although recrystallization is possible. An early brecciation event occurred at ca. 108 Ma. Recracked fractures (>10 cm wide) are interpreted as spring mound vents. A dolomite fault mineralization is dated at ca. 95 Ma. Events affecting fractures include widespread dissolution, with secondary porosity filled by barite, quartz, and solid bitumen. Fluid inclusion geochemistry suggests that diagenesis occurred with the participation of seawater. We show a timeline of diagenetic events and infer that fracture porosity is more likely to be preserved where deep faults enabled fluids from greater depths to ascend into the reservoir, where they created large vuggy cavities by dissolution of host rock.

INTRODUCTION

Fractured carbonates are a type of subsurface reservoir that currently store a large portion of oil and gas resources worldwide

Manuscript received February 1, 2024; provisional acceptance April 23, 2024; revised manuscript received September 1, 2024; revised provisional acceptance November 27, 2024; second revised manuscript received December 13, 2024; final acceptance December 19, 2024.
DOI:10.1306/03182524012

AUTHORS

Rodrigo dos Santos Maia Corrêa ~ *Department of Geological Sciences and Bureau of Economic Geology, The University of Texas at Austin, Austin, Texas; Petrobras S.A., Rio de Janeiro, Rio de Janeiro, Brazil; rodrigo.correa@petrobras.com.br*

Rodrigo dos Santos Maia Corrêa is a structural geologist who has been associated with Petrobras S.A. since 2010. His research integrates brittle deformation, diagenesis, and modeling in carbonate reservoirs. He earned a B.S. degree in geology from the Federal University of Rio de Janeiro in 2009, an M.S. degree in geomechanics from Pontifical Catholic University of Rio de Janeiro in 2016, and a Ph.D. in geosciences from The University of Texas at Austin in 2023. He is the corresponding author of this paper.

Bruno Carvalho ~ *Petrobras S.A., Rio de Janeiro, Rio de Janeiro, Brazil; brcarvalho@petrobras.com.br*

Bruno Carvalho holds an M.S. degree in geology from the Federal University of Rio de Janeiro, specializing in microtectonics. He has been with the Petrobras Research Center since 2011, focusing on structural analysis, structural diagenesis, and fracture modeling. He lectures and coordinates research projects at Petrobras S.A. and in partnership with Brazilian institutions.

Estibalitz Ukar ~ *Bureau of Economic Geology, The University of Texas at Austin, Austin, Texas; esti.ukar@beg.utexas.edu*

Estibalitz Ukar is a research associate professor at The University of Texas at Austin. Her research integrates small-scale structural petrology with large-scale deformation processes and fluid–rock interactions in the upper continental crust. She received her Ph.D. from The University of Texas at Austin in 2010 and her B.S. degree in geology from the University of the Basque Country (Spain) in 2003.

Stephen E. Laubach ~ *Bureau of Economic Geology, The University of Texas at Austin, Austin, Texas; steve.laubach@beg.utexas.edu*

Stephen E. Laubach is a professor (research) and Fellow, Albert W. & Alice M. Weeks Centennial Professorship in Geological Sciences in the Jackson School of Geosciences at The University of Texas at Austin. Laubach was a member of the AAPG Executive Committee and AAPG Elected Editor from 2010 to 2013.

ANDRÉ L. S. PESTILHO ~ *Petrobras S.A., Rio de Janeiro, Rio de Janeiro, Brazil; andrepestilho@usp.br*

André L. S. Pestilho received his B.Sc. and M.Sc. degrees from the University of Campinas and his Ph.D. from the University of São Paulo (USP). He worked as a research geologist specializing in fluid inclusions and organic geochemistry at Petrobras S.A. for 12 years. Currently, he is an assistant professor at USP, focusing on the study of geofluids and their applications to mineral and energy resources.

ANDRÁS FALL ~ *Bureau of Economic Geology, The University of Texas at Austin, Austin, Texas; andras.fall@beg.utexas.edu*

András Fall is a research associate professor at the Bureau of Economic Geology, Jackson School of Geosciences, The University of Texas at Austin. He received a B.S. degree from Babeș-Bolyai University, Cluj-Napoca, Romania, and an M.S. degree and a Ph.D. in geosciences from Virginia Tech. His current research focuses on the nature, properties, and role of fluids in structural diagenesis and in carbon mineralization and natural hydrogen generation in (ultra)mafic rocks.

TOTI LARSON ~ *Bureau of Economic Geology, The University of Texas at Austin, Austin, Texas; toti.larson@beg.utexas.edu*

Toti Larson is a research associate at the Bureau of Economic Geology, The University of Texas at Austin. In his research, Larson applies geochemistry, geology, and machine learning tools to develop predictive subsurface characterization models. He received his Ph.D. in geochemistry from the University of New Mexico in 2003.

DANIEL STOCKLI ~ *Department of Geological Sciences, The University of Texas at Austin, Austin, Texas; stockli@jsg.utexas.edu*

(e.g., Nelson, 2001; Narr et al., 2006; Garland et al., 2012). One of the most prolific discoveries of recent decades is in the Santos Basin, southeastern Brazil. These discoveries are part of the giant Brazilian pre-Salt oil fields that are within Aptian (Lower Cretaceous) lacustrine carbonates of the Barra Velha Formation (e.g., Moreira et al., 2007; Carminatti et al., 2009; Carlotto et al., 2017; Pedrinha et al., 2018; Tanaka et al., 2022).

The Barra Velha Formation host rock is composed mostly of in situ calcite shrub-dominated facies, spherulitic Mg-rich silicate argillites (commonly dissolved or substituted by dolomite or quartz), laminites, and reworked sediments (Terra et al., 2010; De Paula Faria et al., 2017; Herlinger et al., 2017; Arienti et al., 2018; Tosca and Wright, 2018; Lima and De Ros, 2019; Gomes et al., 2020; Hosa et al., 2020; Azerêdo et al., 2021; Carramal et al., 2022; Carvalho et al., 2022; Netto et al., 2022; Fragoso et al., 2023). These deposits formed during evaporitic lake conditions between 123 and 110 Ma (Moreira et al., 2007; Wright and Barnett, 2015; Farias et al., 2019; Wright, 2022), although their exact age is still a matter of debate (Tedeschi et al., 2017; Pietzsch et al., 2020; Sanjines et al., 2022; Lawson et al., 2023). Direct age measurements of calcitic host rock are recent and rare (e.g., Brito et al., 2024), and age is based primarily on ostracod and pollen biostratigraphy (e.g., Moura, 1972; Regali et al., 1974; Arai et al., 1989; Poropat and Colin, 2012; Pietzsch et al., 2018) or extrapolation of K-Ar ages from interbedded mafic rocks (e.g., Mizusaki et al., 1992; Moreira et al., 2007).

The Barra Velha Formation rocks have been described as fractured reservoirs in some locations (Corrêa et al., 2019; Fernández-Ibáñez et al., 2022a, b; Tanaka et al., 2022; Lupinacci et al., 2023; Wennberg et al., 2023). Hydrothermal alteration has been invoked to be associated with fracturing or faulting (Alvarenga et al., 2016; Souza et al., 2018; De Ros, 2021), and analogous examples can also be found in neighboring Macabu Formation in Campos Basin (Vieira de Luca et al., 2017; Tritlla et al., 2018, Lima and De Ros, 2019; Lima et al., 2020). Secondary porosity dominated by fractures and dissolution features impact well productivity (e.g., De Jesus et al., 2016, 2019; Corrêa et al., 2019; Vieira de Luca et al., 2019; Lima, 2020; Silva et al., 2021; Mejia et al., 2022; Mimoun and Fernández-Ibáñez, 2023). Host rock and fractures are commonly associated with several stages of silicification (e.g., Teboul et al., 2019; Sartorato et al., 2020; Basso et al., 2023). However, both the characterization of the diagenetic processes and their association with brittle structures remain poorly understood.

The analysis of diagenetic products, such as cements, in fractures can provide valuable information about how fracture networks were formed (i.e., structural diagenesis) (Laubach et al., 2010, 2019; Beaudoin et al., 2022). Petrographic studies, fluid inclusion microthermometry, and isotope geochemistry combined

with modern techniques such as laser ablation-inductively coupled plasma-mass spectrometry (LA-ICP-MS) and U-Pb geochronology of carbonate minerals (e.g., Roberts et al., 2020; Roberts and Holdsworth, 2022) provide means to characterize the environmental conditions and to date the age of fracture and fault formation (e.g., Hoareau et al., 2021; Corrêa et al., 2022; Muñoz-López et al., 2022; Aubert et al., 2023). Structural diagenetic analysis can be carried out on well rock cores or sidewall core samples, with the benefit of improving knowledge about the subsurface fracture network to constrain inputs to discrete fracture network models (e.g., Corrêa et al., 2019; Tanaka et al., 2022).

Published studies about the Barra Velha Formation suggest that fault damage zones (Chester and Logan, 1986; Caine et al., 1996) play an important role in fracture development and that some fractures are enlarged by dissolution leading to vuggy porosity (i.e., large open cavities in rock volume), although complete or partial porosity obliteration by cement also is common (e.g., Corrêa et al., 2019; Fernández-Ibáñez et al., 2022a, b; Wennberg et al., 2023). Available fracture studies of the area focus only on seismic or macroscopic description of the structures; therefore, fracture microscopic textures, their geochemical characteristics, and age are poorly understood. This lack of information commonly impedes subsurface interpreters in building accurate models. Such models should be constrained by a correct understanding of the brittle deformation and diagenetic processes in the pre-Salt oil fields.

Here, we describe textures of the host rock and brittle structures and interpret the geochemical environment and timing of several diagenetic products. To achieve this objective, we used structural core description, petrography, fluid inclusions analysis (microthermometry, bulk crush-leach, noble gas analysis), carbon and oxygen stable isotope analysis, and U-Pb geochronology of carbonates in cores from two wells drilled in the Barra Velha Formation. We reconstruct the timeline of diagenetic events linking brittle deformation and hydrothermal alteration that affected the Barra Velha Formation, documenting the operation of hydrothermal processes that ultimately impact reservoir quality.

GEOLOGIC CONTEXT

Santos Basin Geology

The Santos Basin is located at the southeastern Brazilian margin in the Atlantic Ocean (Figure 1). This margin was initially rifted apart from the Gondwana continent during the Berriasian (Campos Neto et al., 2007; França et al., 2007; Gontijo et al., 2007; Moreira et al., 2007; Rangel et al., 2007; Rodovalho et al., 2007; Silva et al., 2007; Winter et al., 2007; Chaboureau et al., 2013),

Daniel Stockli is a professor and the John F. and Carolyn C. Bookout Endowed Chair in Structural Geology at The University of Texas at Austin. He is an expert in geochronology and thermochronology applied to structural and tectonic processes. His research focuses on the timing and rates of both ductile and brittle deformation in orogenic zone, rifts, and continental margins.

LISA STOCKLI ~ *Department of Geological Sciences, The University of Texas at Austin, Austin, Texas; lstockli@jsg.utexas.edu*

Lisa Stockli has managed the UTChron laser ablation-inductively coupled plasma-mass spectrometry (LA-ICP-MS) laboratory in the Department of Earth and Planetary Sciences at The University of Texas at Austin for 12 years. She is an expert in U-Pb dating and has extensive experience with in situ and depth-profiling LA-ICP-MS dating techniques in minerals, including zircon, apatite, titanite, calcite, and garnet.

VOLKER LÜDERS ~ *GFZ German Research Centre for Geosciences, Potsdam, Germany; volker.lueders@gfz-potsdam.de*

Volker Lüders is a senior research scientist with GFZ German Research Center for Geosciences, Potsdam. He directed the fluid inclusion laboratory at the Helmholtz Centre Potsdam GFZ, Germany, from 1992 to 2023. He received his M.Sc. degree in geology from University of Göttingen, and his Ph.D. in geochemistry from the Free University Berlin. His fields of research are fluid inclusions, stable isotopes, and trace elements in magmatic, hydrothermal systems and sedimentary basins.

SAMUEL NIEDERMANN ~ *GFZ German Research Centre for Geosciences, Potsdam, Germany; samuel.niedermann@gfz-potsdam.de*

Samuel Niedermann studied physics at the University of Bern and earned his Ph.D. in 1990. He did postdoctoral research at the Department of Chemistry, University of California, San Diego, in 1991–1992. Since 1994, he has been a senior researcher and the head of the noble gas laboratory at the German Research Centre for Geosciences, Potsdam.

DAVID A. BANKS ~ *School of Earth and Environment, University of Leeds, Leeds, United Kingdom; d.banks@see.leeds.ac.uk*

David A. Banks is a principal research fellow at the University of Leeds, where he runs the Fluid Inclusion Laser Ablation ICP-MS Laboratory. His research focuses mainly on geochemistry, fluid inclusions, ore mineralization, and LA-ICP-MS analysis.

ACKNOWLEDGMENTS

We thank Rowan Martindale for allowing access to the Zeiss M2m microscope at The University of Texas at Austin paleontology laboratory. We thank Matheus Schirmbeck for assistance with the cathodoluminescence image acquisition and the Petrobras Research Center for allowing access to laboratory equipment and cores. We also thank Enzio Schnabel (GFZ) for performing the noble gas analyses. This paper benefited from early comments made by Bruno E. M. Lima and V. Paul Wright. We thank three anonymous reviewers who provided great contributions that significantly improved this paper. This study was funded by Petrobras S.A. and by grant DE-SC0022968 from the Chemical Sciences, Geosciences, and Biosciences Division, Office of Basic Energy Sciences, Office of Science, US Department of Energy. Our work on fractures is partly supported by the Fracture Research and Application Consortium at The University of Texas at Austin.

with its African counterpart at the Angolan Cabinda, Kwanza, and Namibe Basins. The original Gondwanan basement is composed of high-grade metamorphic and magmatic rocks that were formed in episodes of accretion and collision during the Brazilian-Pan-African Orogeny in the Neoproterozoic (Heilbron et al., 2008). These rocks constitute the basement under the Santos Basin and may have conditioned rifting tectonics due to previously existing structures, as shown in the nearby Campos Basin (north of Santos Basin) (Fetter, 2009; Strugale et al., 2021). A later change in the direction of rift opening from northwest to southeast to east to west may have caused oblique and transcurrent reactivations of older faults in the Santos and Campos Basins (e.g., Dehler et al., 2016; Savastano et al., 2017). The Santos Basin is a rift basin with oblique opening, mostly structured by extensional tectonics within a magma-poor passive margin (Zalán et al., 2011; Rigoti, 2015). Transfer zones are identified in some parts of the basin as causing local lateral movements that accommodate deformation (Dehler et al., 2016; Magnavita, 2021).

In the Santos Basin, the rifting history started with the propagation of the rift toward the southern Brazilian margin and the deposition of mafic volcanic rocks, the Camboriú Formation, mainly during the Hauterivian (Early Cretaceous) (Moreira et al., 2007). The sedimentary infill began in the Barremian (Early Cretaceous) with the deposition of a sequence of siliciclastic rocks, the Piçarras Formation, mostly composed of alluvial-lacustrine shales and stevensitic (i.e., variety of the clay mineral smectite) sandstones (e.g., Leite et al., 2020). By the end of the Barremian and the beginning of the Aptian (Jiquiá local age) (e.g., Moura, 1972; Pietzsch et al., 2018), new bioclastic carbonate rocks commonly composed of pelecypod shells formed most of the Itapema Formation, an important reservoir that also contains some of the main shaly source rocks deposited in the deepest parts of the lake. Most of the Itapema Formation reservoirs comprise bioclastic rudstones and grainstones, thought to have formed in lake islands, with constant freshwater input, enabling a suitable environment to foster life diversity (e.g., Sabato Ceraldi and Green, 2017; Mizuno et al., 2018; Muniz and Bosence, 2018; Pietzsch et al., 2018, 2020). This interpretation is supported by progradational features in seismic lines that suggest a relevant lacustrine bathymetric relief at this stage (e.g., Carlotto et al., 2017; Barnett et al., 2021). The top of the Jiquiá Stage is capped by the sub-Alagoas unconformity that separates the bioclastic Itapema Formation from the overlying Barra Velha Formation.

The Barra Velha Formation was deposited during the Aptian (Alagoas local age), where environmental conditions were very arid and the lake became underfilled (e.g., Moreira et al., 2007; Wright and Barnett, 2015; Tosca and Wright, 2018), forming unique chemical conditions that allowed the deposition of large amounts of lacustrine carbonate rocks that form the main

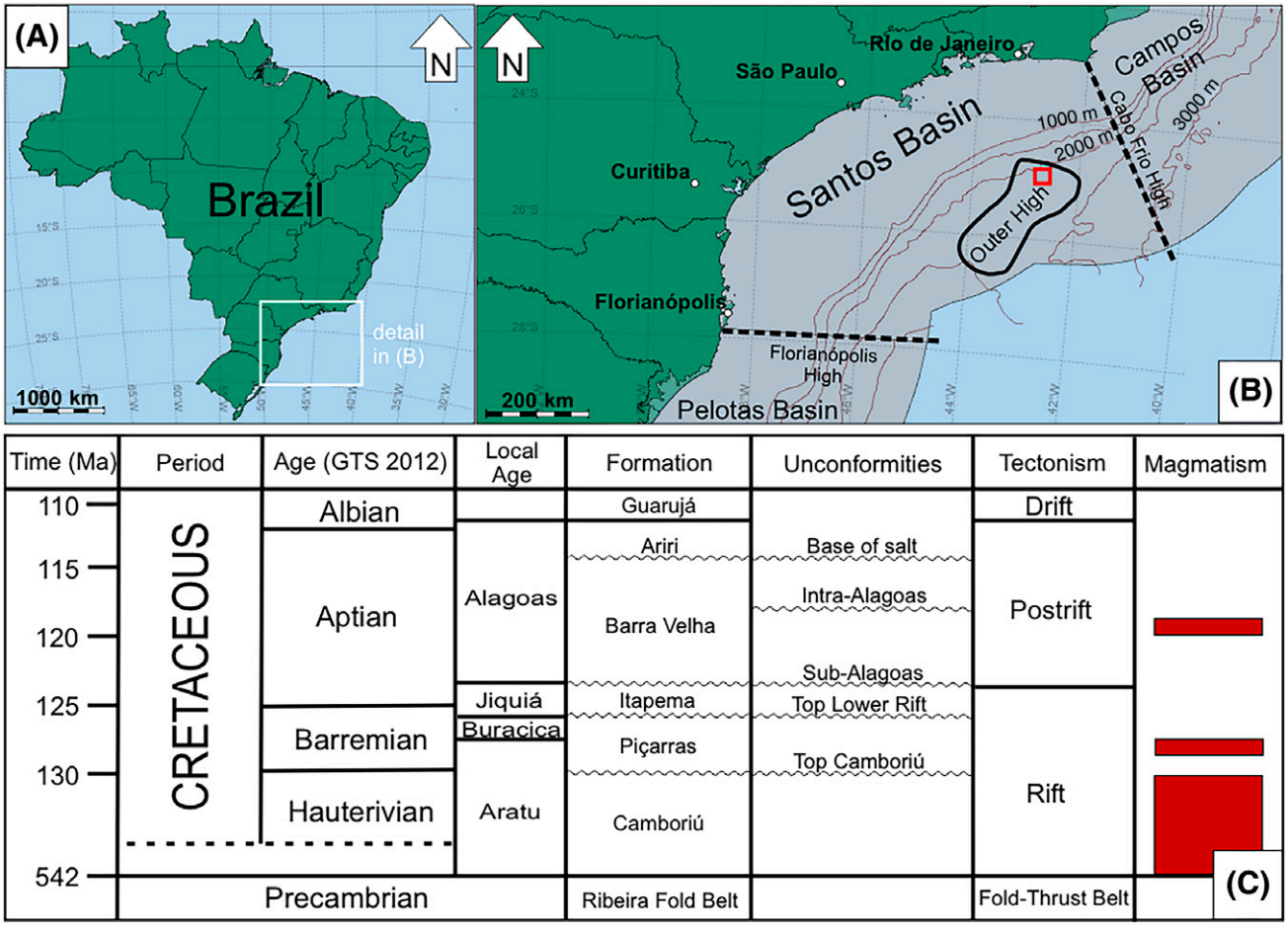

Figure 1. Santos Basin location and stratigraphic chart. (A) Map of Brazil with location of the Santos Basin at the southeastern coast of Brazil, inside the white square. Internal Brazilian state borderlines are in black. (B) Location of the studied oil field (red square) within the Santos Basin outer high (thick solid black line). The basin is limited by the Cabo Frio high on the northeast and the Florianópolis high on the southwest (dashed lines). (C) Stratigraphic chart of Santos Basin showing the position of the Barra Velha Formation, the main reservoir of the Brazilian pre-Salt fields. The Ariri Formation is formed by evaporites and is a regional seal for the oil fields within the Barra Velha Formation. Main magmatic events, tectonic phases, and unconformities are shown on the right side (modified from Moreira et al. [2007], Buckley et al. [2015], and Wright [2022]). GTS = geological time scale.

reservoir in the pre-Salt of the Santos Basin. The most common reservoir facies are in situ calcite shrub-dominated facies (shrubstone [Gomes et al., 2020]) and Mg-rich silicate argillites with spherulites (spherulitestone [Gomes et al., 2020]) that may show variable amounts of diagenetic alterations that can create secondary porosity. These shrubby and spherulitic calcite textures are thought to have formed in special conditions when the lake water was alkaline and supersaturated with respect to calcite, with the microbial contribution being a rare component, mostly linked to laminite facies (e.g., Terra et al., 2010; Souza et al., 2018; Lima and De Ros, 2019; Pietzsch et al., 2022). Laminites and grainstones can form cyclical deposits with silica beds (Wright and Barnett, 2015), due to variation in freshwater input and pH level. The lower Barra Velha section is capped by the intra-Alagoas unconformity that separates the less-structured upper section from the more-structured lower section, which is the same organization seen in most neighboring basins along the Brazilian southeastern coast (e.g., Strugale and Cartwright, 2022).

Fractures are commonly observed both in cores and image logs, frequently associated with vuggy porosity (Corrêa et al., 2019; Wennberg et al., 2023), and usually related to silicified zones (Lupinacci et al., 2023; Mendes et al., 2024). Fault zones show high fracture density and are important conduits for fluid flow (Fernández-Ibáñez et al., 2022b; Tanaka et al., 2022).

The Barra Velha Formation is overlain by the evaporites of the Ariri Formation, deposited with the emplacement of extremely arid environment and marine incursions (Moreira et al., 2007). The Ariri Formation acts as a regional seal for the pre-Salt accumulations. Later, the Santos Basin evolved into a passive-margin marine basin, as represented by sedimentary successions of the Camburi, Frade, and Itamambuca Groups (Moreira et al., 2007). Lastly, apart from the Camboriú Formation, at least four magmatic events that occurred in the basin during the Barremian, Aptian, Campanian, and Eocene have been recorded (Moreira et al., 2007).

The evolution of the Santos Basin is linked to other basins along the Brazilian and the Angolan coasts, which also have pre-Salt reservoirs like the Barra Velha Formation. To the north, the Santos Basin is separated from the Campos Basin by the Cabo Frio high. To the south, it is separated from the Pelotas Basin by the Florianópolis high, also thought to have impeded communication with seawater during most of the Early Cretaceous. Toward Africa, the Kwanza and Namibe Basins are the original continuation, now separated by the Atlantic Ocean (e.g., Moulin et al., 2010; Sabato Ceraldi and Green, 2017).

Well Data

The samples studied here originate from drill cores from two producing vertical wells in one oil field in the Barra Velha Formation. The wells were extensively cored, allowing us to describe the structures and to prepare thin and thick sections, rock chips, and rock powders for geochemical analysis.

Our analysis is focused within the limits of the Barra Velha Formation. Seismic lines show that both wells are positioned in mounded carbonate features (several hundred meters high), with chaotic seismic facies (Figure 2). It is also possible to see deep faults crossing the Barra Velha Formation, some of which reach the basement and the top of the Barra Velha Formation, where evaporites are deposited. The tops of these mounds are capped by an anhydrate layer. Both wells showed severe drilling mud loss during the drilling operation, indicating the presence of open conduits. Formation tests show permeability levels up to several darcies, which is much higher than matrix permeability, indicating an extramatrix component in the permeability (e.g., Fernández-Ibáñez et al., 2022a).

Well A has a total of 10.6 m of core length. Although we studied the entire cored section, most of our work focused on one representative part of ~4 m, where we could clearly observe intensive brittle deformation with vuggy fractures (e.g., Nelson, 2001) and cavities lined by euhedral quartz (i.e., quartz geodes). In addition to this core, we obtained a spherulitestone sample from a drilled plug, located deeper and ~250 m below the core position in well A, in the lower Barra Velha Formation, to be used

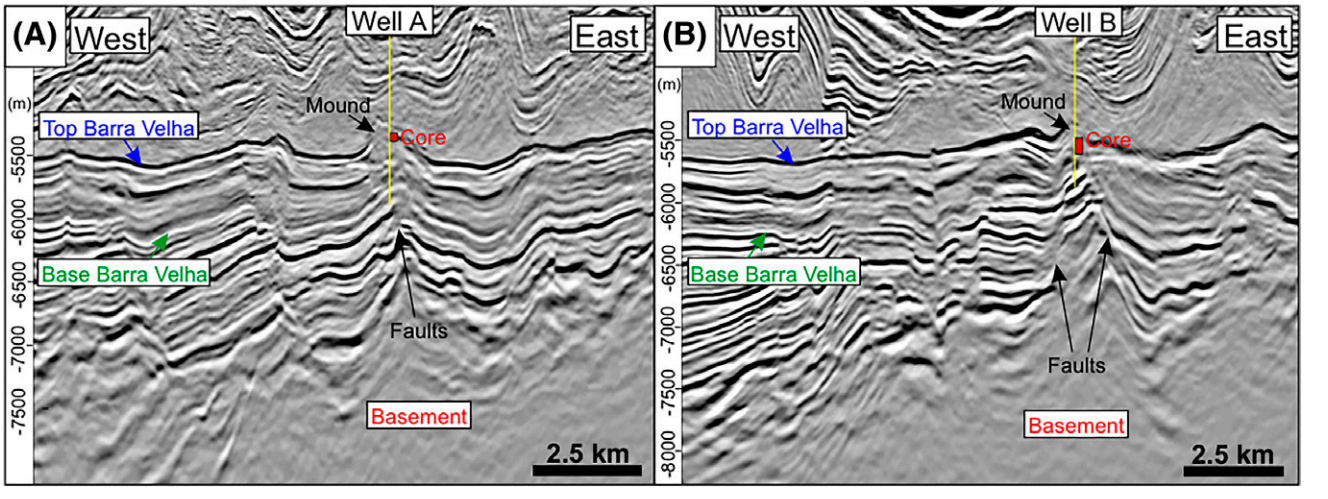

Figure 2. Seismic sections in depth showing the locations of wells A and B. Both wells were drilled in carbonate mounds that are rooted by deeply faulted basement and reservoir blocks. Well trace is in yellow; core positions are shown by red rectangles. (A) East-west seismic section with location of well A. (B) East-west seismic cross section with location of well B. Note faults displacing the top of the Barra Velha Formation.

specifically for petrography and geochronology. Well B has a total of 99.39 m of core length. Our studies focused on one interval of 15.8 m, where we observed intensive brecciation and faults.

METHODS

Structural Core Description

Core orientation was not available, and thus we measured dip angle variation, fracture width (i.e., total opening displacement) and apertures (i.e., preserved open part of the fracture) (Ortega et al., 2006; Bisdom et al., 2016; Wennberg et al., 2016). Since the wells are nearly vertical, the dip angles can be obtained directly from the core without angular corrections (e.g., Terzaghi correction). For macroscopic and microscopic descriptions of host rocks, we used the classification from Gomes et al. (2020) that is well suited for the rocks of the Barra Velha Formation.

The brittle structures in core can be divided into faults and opening-mode fractures having various degrees of mineral fill. We designated structures in core using the following nomenclature.

Fault: macroscopic shear planes with striation and associated breccia and cataclasis. Used for structures of unknown displacement, but likely greater than centimetric (Hancock, 1985).

Small displacement fault: fault showing centimetric or millimetric shear displacement (i.e., wall parallel movement) and cataclastic texture.

Collapse breccia: rock composed of clasts of host rock or of other breccias, commonly cemented, sometimes show geopetal infill and evidence of roof collapse (Shukla and Sharma, 2018).

Fault breccia: rock composed of clasts of host rock or of other breccias, commonly cemented and with angular fragments, found within fault zones (Shukla and Sharma, 2018).

Opening-mode fracture: general term for fractures showing wall perpendicular displacement, which can be filled with cement or not.

Vein: fully or partially cemented opening-mode fracture (Hancock, 1985).

Vuggy fracture: opening-mode fracture with dissolution features and aperture commonly larger than 1 cm (e.g., Nelson, 2001).

Wide vein: cemented opening-mode fractures with widths larger than 10 cm, with irregular walls, crack-seal texture, cementation by quartz and calcite, internal brecciation, geopetal infill, and vuggy pores.

Geode: vuggy pore (larger than 1 cm) or cavity coated by euhedral crystals.

Petrography

Some types of fractures were too small to be macroscopically visible in the cores and needed further investigation through microscopy. In total, we prepared 9 thin sections from the well A drill core and 23 thin sections from the well B drill core. We stained the thin sections using Alizarin Red S where we needed to differentiate calcite from dolomite (Friedman, 1959). Thin sections were analyzed using transmitted light in a Zeiss Imager A2m microscope, and several thin sections were imaged into a photomosaic using a Zeiss M2m microscope. We observed cement fabrics and crosscutting relationships to determine cement precipitation order.

Some thin sections were carbon coated and imaged using backscattered electron microscopy using a Zeiss Sigma high vacuum field emission scanning electron microscope with 5 to 7 kV. We used an energy-dispersive x-ray spectroscopy detector to obtain x-ray spectra with 15 kV from locations where mineral identification was dubious using only transmitted light petrography. We also acquired optical cathodoluminescence images from some samples to assess the degree of recrystallization. For this, we used a CITL MK5-2 cathodoluminescence device coupled into a Zeiss Scope.A1 microscope under a beam current of 200 μA and 10 kV.

Fluid Inclusion Microthermometry

Fluid inclusion petrography was conducted using a Zeiss microscope equipped with an ultraviolet (UV) epifluorescence light (UV metal halide light source and 4′,6-diamidino-2-phenylindole filter) and 50× and 100× objectives combined with auxiliary lenses of ×1.6 and ×2.5. Fluid inclusions were classified based on their textural and spatial distribution into primary and secondary fluid inclusion assemblages (FIAs), following the genetic classifications of Roedder (1984), Goldstein and Reynolds (1994), Goldstein (2001),

and Fall and Bodnar (2018). Microthermometry followed the procedures described in Goldstein and Reynolds (1994). For microthermometry, we used both a Fluid Inc.–adapted US Geological Survey–type gas-flow heating/freezing stage on an Olympus B ×41 microscope, and a Linkam THMS600 heating/freezing stage mounted on the Zeiss microscope. Both stages were calibrated using synthetic fluid inclusions (H_2O-CO_2 and pure H_2O with critical density), and data were obtained with precisions of ±0.1°C for both stages.

Bulk Crush-Leach

Bulk crush-leach analysis of fluid inclusions was carried out at the University of Leeds following the methodology described in detail by Banks et al. (2000) and Lüders et al. (2002). Samples of barite and quartz were crushed to 1- to 2-mm grain size, cleaned by boiling several times in 18.2 MΩ water, and dried before the analysis. Approximately 0.5–1 g purified sample material was manually crushed with an agate mortar and pestle. The resulting mineral powder was leached with 18.2 MΩ water and filtered through a 0.2-μm nylon filter before the analysis. Ion chromatography was used for the analysis of the anions Cl^- and Br^- in the leachate solutions. The cations Na^+, K^+, and Li^+ were measured using flame emission spectroscopy. The detection limits for the elements analyzed were as follows: Na = 20 ppb, K = 25 ppb, Li = 1 ppb, Cl = 20 ppb, and Br = 1 ppb. The average precision, as determined from a series of replicate analyses, is better than 10% relative standard deviation.

Noble Gas Analysis

Noble gas analysis was performed using samples of 0.18 to 1.02 g of hand-picked quartz and barite mineral separates. The samples were loaded into an ultra-high vacuum spindle crusher, which was pumped at room temperature for at least 24 hr to remove the atmospheric gases adsorbed on grain surfaces. For gas extraction, the samples were crushed under vacuum, and the gases released were admitted to the preparation line. Water was frozen in a dry ice–cooled trap, and other chemically active species were removed in Ti sponge and ZrAl getters. The noble gases were then separated from one another in a cryogenic adsorber, and noble gas concentrations and isotopic compositions were determined in a VG5400 noble gas mass spectrometer according to the procedures described by Niedermann et al. (1997) and Lüders and Niedermann (2010).

C and O Stable Isotope Analysis

We obtained C and O stable isotopic compositions from calcites at The University of Texas at Austin Bureau of Economic Geology stable isotope laboratory using rock powders collected with a microdrill from several locations in the cores. The powders were stored individually in clean glass vials for analysis. We cleaned the drill bit using water between each sample acquisition to avoid contamination. Aliquots of ~0.3 mg were analyzed for $\delta^{13}C$ and $\delta^{18}O$ using a Thermo Fisher Scientific GasBench II coupled to a Thermo Fisher Scientific MAT 253 isotope ratio mass spectrometer (Révész and Landwehr, 2002; Spötl and Vennemann, 2003). We reacted the samples in helium-flushed vials with H_3PO_4 at 50°C for 8 hr. Data were calibrated (values are reported in per mille Vienna Peedee belemnite [VPDB]) using calcite standards NBS-18 ($\delta^{18}O_{VPDB}$ = −23.0‰, $\delta^{13}C_{VPDB}$ = −5.0‰) and NBS-19 ($\delta^{18}O_{VPDB}$ = −2.3‰, $\delta^{13}C_{VPDB}$ = 1.95‰). Replicates of an internal carbonate standard were analyzed throughout the analytical session to account for analytical drift and precision, reaching an analytical precision of ±0.06‰ for $\delta^{13}C_{VPDB}$ and ±0.10‰ for $\delta^{18}O_{VPDB}$ routinely.

LA-ICP-MS U-Pb Geochronology

We analyzed calcite U-Pb geochronology at the UTChron laboratory at The University of Texas at Austin. The LA-ICP-MS system consists of a Photon-Machines Analyte G2 ArF excimer 193-nm laser, equipped with a two-volume HelEx sample cell, coupled to a Thermo Element 2 double-focusing magnetic sector ICP-MS. The helium carrier gas is mixed with argon before entering the ICP-MS. The analyses were conducted on polished thick sections (>120 μm thick) and thin sections (30 μm thick) in static spot mode. For the thick sections, we used a laser beam diameter of 110 μm, operated with an energy density of 3.82 J/cm^2 measured with an energy meter and a pulse rate of 10 Hz. For the thin sections, we used a laser beam diameter of 110 μm, operated with an energy density of 2.86 J/cm^2 and a pulse rate

of 8 Hz. The analysis followed the routine of 4 cleaning shots, 27 s of baseline data collection, 20 s of ablation, and 27 s of washout. The number of ablation shots varied depending on the section thickness and can vary between 150 and 300 shots.

We corrected elemental and isotopic fractionations by interspersed analysis of primary calcite reference material WC-1 ($^{206}Pb/^{238}U$ age 254.6 ± 6.4 Ma; Roberts et al., 2017). Analyses were made in repeating blocks of 2 standards, followed by 10 unknowns, with NIST614 measured periodically to monitor Pb isotopic fractionation. Age calculation was performed using Iolite version 3.7 (Paton et al., 2011) and VizualAge UcomPbine (Chew et al., 2014). A ^{207}Pb common Pb correction was applied to correct for common Pb in the primary reference material (WC-1 $^{207}Pb/^{206}Pb = 0.85$).

In each region of interest within the studied sections, at least 17 spots were ablated. Time-integrated data were exported as entire 20-s ablation windows if isotopically homogenous or broken up into 2 to 4 shorter ablation windows if exhibiting isotopic variation. The U-Pb data were plotted in Tera-Wasserburg diagrams and lower intercept ages calculated using IsoplotR (Vermeesch, 2018). We show errors for isotopic ratios and ages as 2σ absolute errors.

Chalcedony cement was ablated at several locations in one sample from well A to investigate uranium content, which had previously been identified as anomalously high in this interval by wire-line logs (Melani, 2019).

RESULTS

Brittle Deformation

We list below the visible structures in the core and organize them according to their relative age based on crosscutting and abutting relationships (Table 1). We show an individual scheme for the sequence of brittle structures found in each well.

Well A

Core Description—Well A shows a predominance of shrubstones and grainstones (~80%) with minor intervals of spherulitestones and laminites as host rock (Gomes et al., 2020). Silica beds intercalated with sediments are commonly fractured locally, with stratabound fractures (Odling et al., 1999) spanning the layer thickness (~2 cm) (Figure 3F). Fractures cut the host rock with dip angles between 42° and 90°, with an average dip angle of 78°; most are pure opening-mode fractures or show a small shear displacement. Some intervals of the core (~20 cm long) are incohesive and may represent intervals of intense fracturing. The predominant structural features are quartz-filled opening-mode fractures with irregular, corroded walls.

Table 1. Summary of Structures Described in Wells A and B

Well	Structure	Mineral Fill	Observation	Dip, °	Width, mm	Age
A	Vuggy fracture	Chalcedony/quartz/solid bitumen	Commonly vuggy	42–80	0.75–1.75, up to 40 (if vuggy)	Youngest
A	Opening-mode fracture	Dolomite (micro)	Apparent micritic precursor	–	–	–
A	Small displacement fault	Cataclastic calcite	Cataclastic texture	85–90	0.14	–
A	Opening-mode fracture	Quartz	Fractured silica layer/sometimes vuggy	Variable; 90 to bedding	–	Oldest
B	Vein	Quartz/barite/solid bitumen (micro)	Sometimes vuggy	20–90	1.4–12	Youngest
B	Fault (several generations)	Saddle dolomite (with quartz and barite)	Mineralized fault breccia	85	35 (fault core)	–
B	Wide vein	Calcite and quartz	Internally brecciated	65–72	100–120	–
B	Collapse breccias	Calcite and quartz	Radiaxial-fibrous calcite rims and microcrystalline infill	–	–	Oldest

Structures are organized relatively by age, with the youngest structures at the top.

Figure 3. Fracture and dissolution features observed in the core from well A. (A) Vuggy fracture (Vf) cutting the shrubstone host rock with alteration halo. Most primary pores of the host rock are filled with grayish quartz. Host rock is commonly observed with vuggy aspect. (B) The Vf crossing the core. Vugs are coated with up to 1-mm-sized euhedral quartz crystals. (C) The vuggy fractures filled with yellowish quartz (Yqtz) and shrubstone host rock cemented with grayish quartz (Gqtz). Sparse vugs or geodes filled by quartz crystals are observed in the host rock. (D) The vuggy fractures with centimeter-sized aperture coated by euhedral quartz. (E) Narrow small displacement fault (Sf) swarm, with cataclastic fill. (F) Silica layer bearing bed-perpendicular opening-mode fractures. (G) Silicified spherulitestone host rock and open Vf with euhedral quartz. This fracture is associated with centimeter-sized quartz geodes (Qtzg).

These fractures are interpreted to represent dissolution followed by quartz precipitation. Pitting causes opposite fracture walls to not match, so that the original fracture width cannot be observed any longer. Carbonate dissolution on fracture walls differentially enlarged opening displacement, hindering observation of the original fracture wall position.

In some cases, the pitting and thus dissolution along the fracture planes is so pervasive that the site of former fractures forms geodes with continuous vuggy cavities (i.e., vuggy fractures) that are commonly partially filled with euhedral quartz crystals (Figure 3A–D, G). Locally, we observed an alteration halo changing the color of the host rock around the fractures (Figure 3A). Narrow fractures are commonly completely cemented with quartz, whereas wider fractures of at least 1- to 2-cm width are mostly open. Pervasively cemented fractures linked

to geodes that still preserve porosity often can be observed (Figure 3C). Quartz fills the fracture width completely, except where aperture is preserved and so enlarged (approximately >1 cm) that vuggy pores are present. In this case, the vug is contained along the fracture plane (Figure 3D). Pore size in vugs is variable and can reach up to 3 cm width. Some fractures show yellowish quartz cement on the fracture walls and a second generation of grayish quartz cement in the fracture center. Host rock pores are commonly filled by the grayish quartz cement or show a vuggy texture (Figure 3A). We also observed swarms of older narrow (<1 mm) subvertical small displacement faults with cataclastic texture that are cut by younger vuggy fractures filled with quartz (Figure 3E).

Petrography—In some sections of well A, there is microscopic evidence of shear deformation, marked by small displacement faults showing fault breccias with cataclastic matrix (Figure 4E). These fault breccias have clasts of the host rock, and the presence of cataclasis is evidenced by different sizes of grains formed by chipping. They occur relatively early, because they are crosscut by later fractures filled by quartz cementation that is widespread in the samples from well A. Also early are opening-mode fractures filled with a micritic infill, intensely substituted by rhombohedral dolomite and that are crosscut by quartz veins (Figure 4F). The fractures with micritic infill differ from the small displacement faults because they are dolomitized and do not contain host rock clasts or breccias.

The vuggy fractures observed in well A also exist at the microscale and contain two phases of quartz cement. The first phase filling the quartz veins is a banded chalcedony, which corresponds to the yellowish quartz from the macroscopic observations. Chalcedony covers the fracture wall following an irregular contact with host rock (Figure 4A, B). In the center of the quartz veins, megaquartz (i.e., blocky or macrocrystalline quartz) cement fills the remaining fracture pore space. This fill can constitute from 10% to 50% of the fracture volume. In sections of the core where fracture aperture is wider than 1 to 2 mm, quartz cement has euhedral terminations, and porosity is still preserved. However, smaller pore sizes are usually completely cemented by quartz. A black material lacking crystalline habit can be found in some vuggy fractures and is interpreted as solid bitumen (Figure 4C).

Quartz-filled fractures contain fragments of the host rock. Both quartz cement phases overgrow broken pieces of host rock walls within the cemented fracture. The chalcedony cement phase is the first and thus coats broken pieces of host rock in larger proportions, showing a characteristic banding around host rock clast and tiny inclusions (Figure 4D). Locally, fractures that are only filled with megaquartz cut fractures filled with chalcedony, suggesting that megaquartz is a late mineralization phase contemporaneous with a later deformation event. In some cases, where fractures are filled with both quartz cement phases, broken pieces of chalcedony-coated host rock are rebrecciated and cemented in the fracture by megaquartz. A late phase of narrow (1 mm) quartz-filled opening-mode fractures crosscut all of the structures with regular sharp fracture walls.

The cathodoluminescence images from host rock depositional shrubs and spherulites show a consistent orange color through the crystals and small (0.1–0.2 mm), dark luminescence areas that do not seem to be relevant in volume (Figure 5A, B). At one of the samples from well A we detected consistent changes in cathodoluminescence (Figure 5C).

In one of the samples, we imaged two spherulites (Figure 5B, spherulite 1 at right, spherulite 2 at left) that show LA spots on the borders and in the center. The cathodoluminescence color shows a brighter color around the spots, suggesting that the LA may have affected the resulting color obtained from cathodoluminescence around the laser pits.

Sequence of Events—The first event observed is fractured silica layers bearing opening-mode fractures spanning bed thickness (Figure 6A). The following events are small displacement faults, with cataclastic texture usually having a high dip angle (>85°). Subsequently, opening-mode fractures cut the older structures, and show microcrystalline infill that is largely dolomitized (Figure 6B). The youngest observed structures are the vuggy fractures that are evidence of dissolution of fracture walls, followed by an initial chalcedony cementation that usually contain cemented pieces of broken fracture walls (Figure 6C). Megaquartz cementation follows, and some fractures are filled only by megaquartz. Solid bitumen can be found as the latest phase of fracture infill. In cases in which the fracture aperture is large (>1 cm), open pores are preserved within geodes.

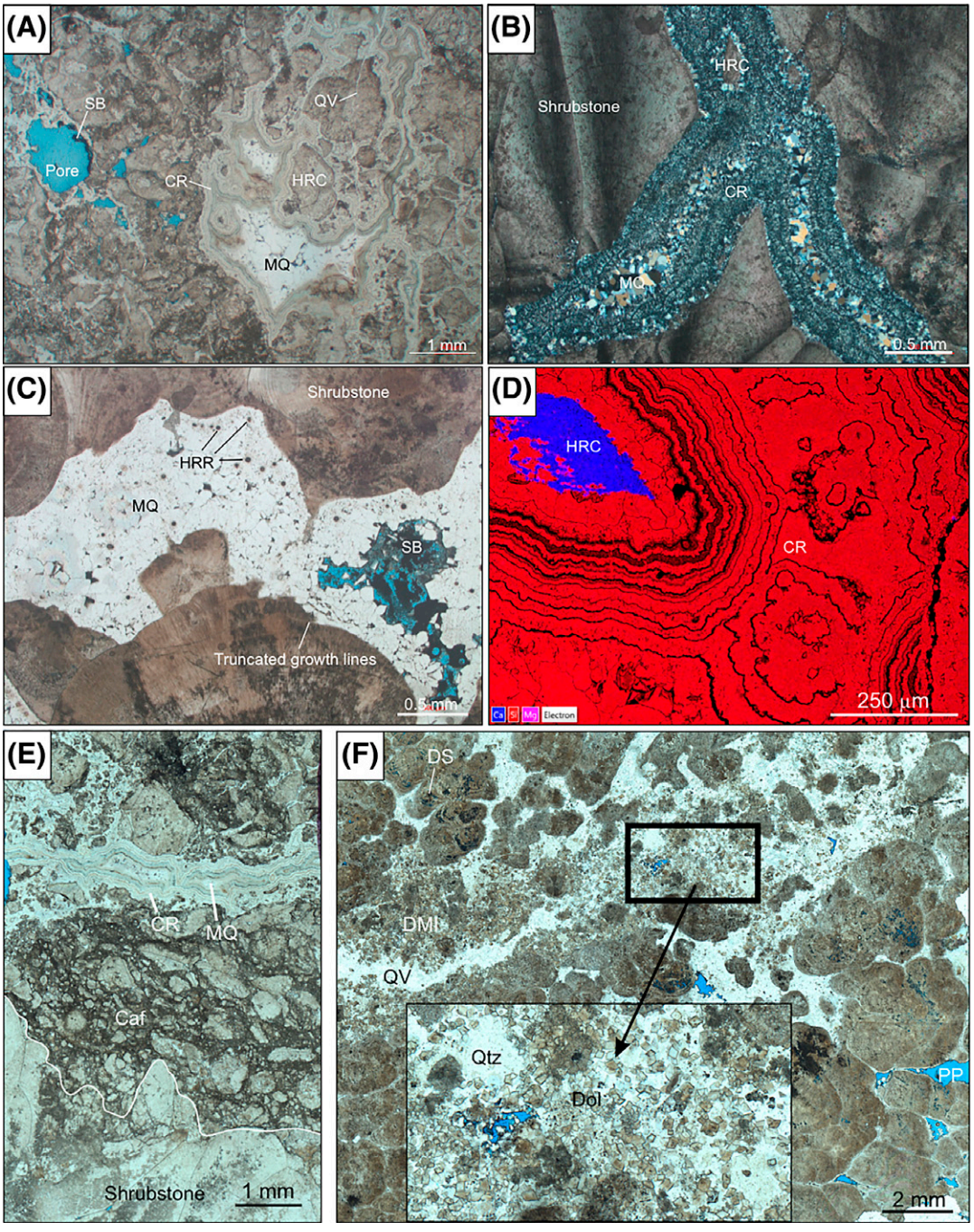

Figure 4. Photomicrographs of well A thin sections. (A) Quartz vein (QV) filled by chalcedony rims (CR) and megaquartz (MQ) in the center cutting a shrubstone host rock. Note irregular walls and the association with rounded clasts of host rock (HRC). Open porosity is secondary and associated with quartz cement and solid bitumen (SB). Younger QVs crosscut the older structures. Plane-parallel transmitted light. (B) Shrubstone with QV filled by CR, MQ, and HRC. Cross-polarized transmitted light. (C) Vuggy fracture filled with MQ and SB. Note irregular walls and truncated growth lines on shrubs, evidence of dissolution of fracture walls. Host-rock relicts (HRR) are seen in the form of small circular inclusions and often follow the fracture wall. Plane-parallel transmitted light. (D) Backscattered electron microscopy/energy-dispersive spectroscopy image of banded CR with a calcitic host rock clast (HRC) and banding around smaller inclusions. (E) Small displacement fault with cataclastic texture (Caf) is crosscut by a vein filled by CR and MQ. Plane-parallel transmitted light. (F) A QV crosscutting a shrubstone host rock. The vein crosscuts an older cavity filled with a dolomitized micritic infill (DMI). Primary porosity (PP) is preserved between shrubs and secondary porosity by shrub dissolution (DS) is common. The detail shows dolomite (Dol) and quartz (Qtz) filling the fracture. Plane-parallel transmitted light.

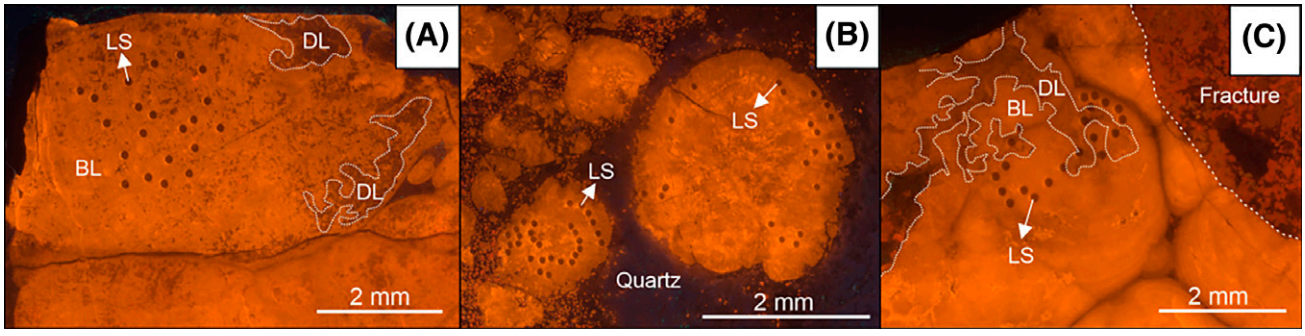

Figure 5. Cathodoluminescence images showing laser ablation spots (LS). (A) Calcite shrub in well A shows consistent bright orange luminescence (BL) with minor nonluminescent spots. Larger dark nonluminescent areas (DL) can be seen on the right side, away from the laser spots. (B) Calcite spherulite with consistent color around the rim and darker colors in the center. The LSs are at the rims of spherulite 1 (right/large) and in the center and at the rims of spherulite 2 (left/small). The Mg-rich clay matrix is seen substituted by quartz with bluish luminescence and orange luminescent dolomite. (C) Calcite shrub with probable recrystallization or alteration showing areas with DL and BL. Some LSs are in the dark areas. A fracture on the right side of the image is filled with dark orange dolomite.

Well B

Core Description—Well B shows a predominance of spherulitestones and laminites (~60%) as host rock, with smaller portions of shrubstone and grainstone. In several places, identification of the host rock type is hindered by brecciation, closely spaced fractures, and silicification. Several fractures cut the host rock with dip angles varying between 20° and 90° (Table 1). Wall offsets show that most fractures have pure opening-mode displacement and attitudes at a high angle to bedding. Locally, some of the fractures having a component of dilatational offset may demonstrate millimetric shear displacement (possible sheared opening-mode fractures). Depositional beds are commonly tilted and may assume extreme steep dip values of 70°. In some cases, bed dips are steep, and fractures are at a high angle to bed dip.

The predominant structural features in this core are collapse and fault breccias (Figure 7A, C). These appear in several core intervals and range from microscale to centimeter-sized clasts accounting for ~30% of the core. Brecciated intervals can comprise up to 2 m of continuous length of the core.

Collapse breccias have subrounded clasts that may suggest that carbonate corrosion occurred on borders and radiaxial-fibrous calcite rims around clasts due to cementation in an open pore space (Figure 7A). We observed clasts of host rock up

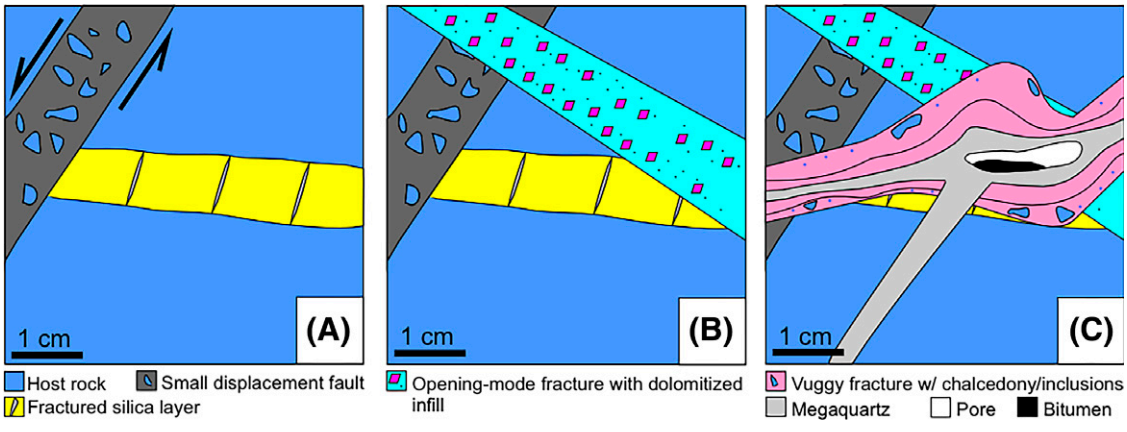

Figure 6. Sequence of brittle deformation events in well A based on crosscutting relationships. (A) Fractured silica layers and small displacement faults showing cataclastic texture and clasts of host rock within a dark matrix. (B) Opening-mode fracture filled with microcrystalline infill that is dolomitized. (C) Chalcedony and megaquartz veins showing irregular walls and quartz geodes, with preserved porosity. Fragments of host rock wall are cemented within chalcedony cement. Megaquartz cement can be found filling some fractures without the earlier chalcedony phase. Solid bitumen is commonly the final filling in fractures. Pore is commonly preserved where fracture widths are large.

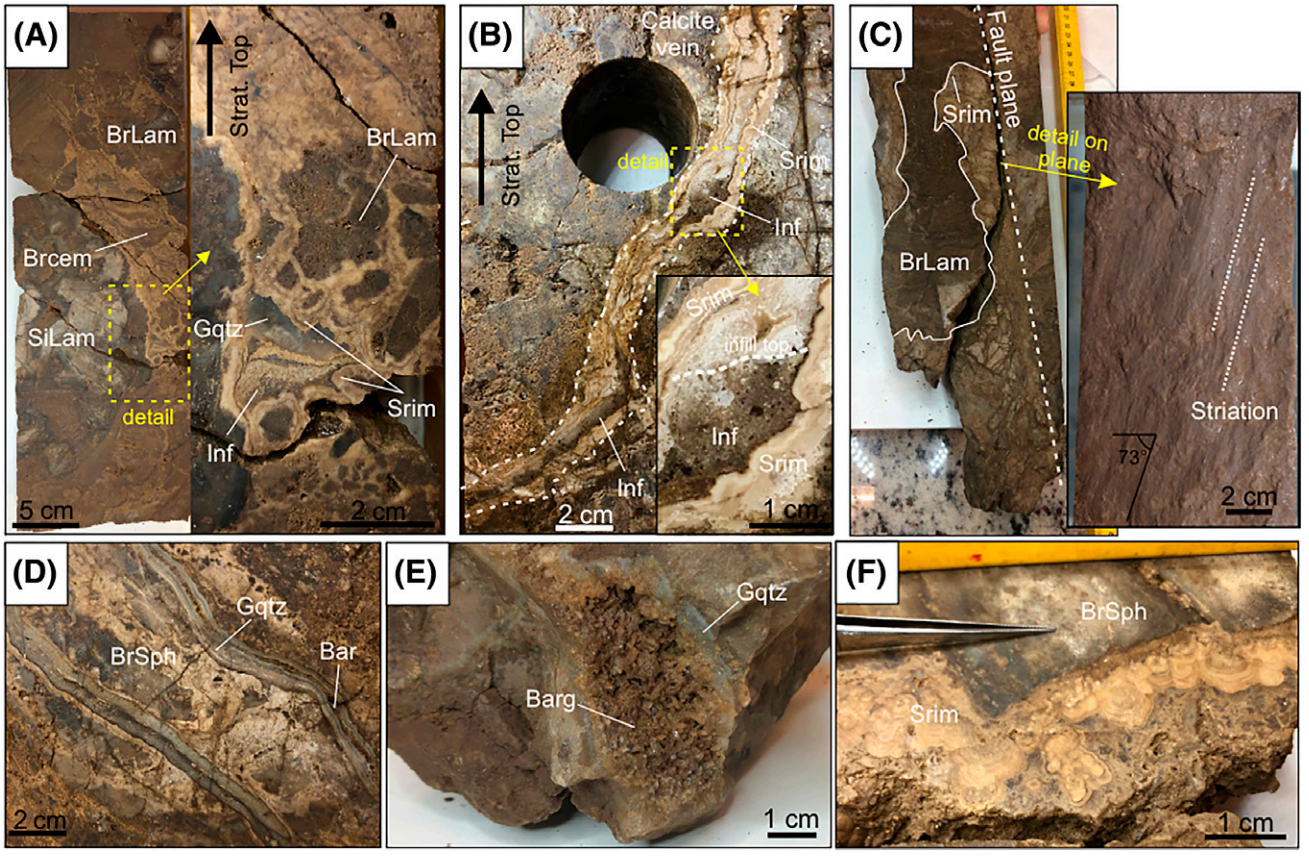

Figure 7. Fracture, fault, and collapse breccia features from well B. (A) Brecciated laminite host rock (BrLam). The collapse breccia is cemented with calcite (Brcem) and the laminite is silicified in some parts (SiLam). In the detail (inset), breccia clasts have radiaxial-fibrous calcite rims (Srim) and are deposited on the bottom of an irregular cavity. Collapse breccia pore is filled with a stratified infill material (Inf) on the bottom as a geopetal indicator and is cemented with grayish quartz (Gqtz). (B) Calcite vein with radiaxial-fibrous calcite rims and filled with fine Inf locked on the irregularities of the wall toward the bottom as a geopetal feature. (C) Fault plane cuts previously BrLam with radiaxial-fibrous calcite rims and showing oblique downdip striations. (D) The Gqtz and barite (Bar) veins cut brecciated spherulitestone (BrSph). (E) Barite geode (Barg) in a vuggy pore associated with quartz veins. Barite was deposited after Gqtz. (F) Early Srim deposited around a clast of BrSph. Strat. = stratigraphic.

to 10 cm wide rimmed by early calcite cement (Figure 7F, radiaxial-fibrous texture). In some cases, we observed a fine infill material associated with brecciated textures or veins that was deposited on the bottom of the structure, and we interpreted the infill material as geopetal feature and indicative of collapse (Figure 7A, B). The infill occurred after brecciation and formation of radiaxial-fibrous calcite cement, as shown by pore-filling order. Collapse breccia pores are mostly cemented by a last cement phase of gray quartz.

We also observed wide veins that are filled with several phases of calcite cement and quartz (Figure 8). These veins are distinct from other fractures described in the cores because they have large widths up to 12 cm, dipping ~65°–72° and have internal brecciated fabric cemented with both calcite and quartz. They appear to have textures compatible with repeated opening and sealing such as crack seal (Ramsay, 1980). These structures have several cement phases, dissolution textures, and crosscutting relations compatible with recracking. We also observed quartz geodes filling vuggy porosity within the wide veins, although pervasive cementation by calcite is common (Figure 8A, bottom detail). In general, these veins have irregular contact with the host rock and locally show geopetal infill and vertically rotated fragments of host rock bedding planes (Figure 8B).

A fault plane that crosscuts collapse breccias and the wide veins (Figure 7C) dips 85° and shows oblique-slip lineations with 73° of rake, suggesting normal-oblique movement. The minimum throw is at least 0.5 m based on core size, but the exact throw value is potentially larger because offset correlative beds are beyond the core limits. This fault is associated

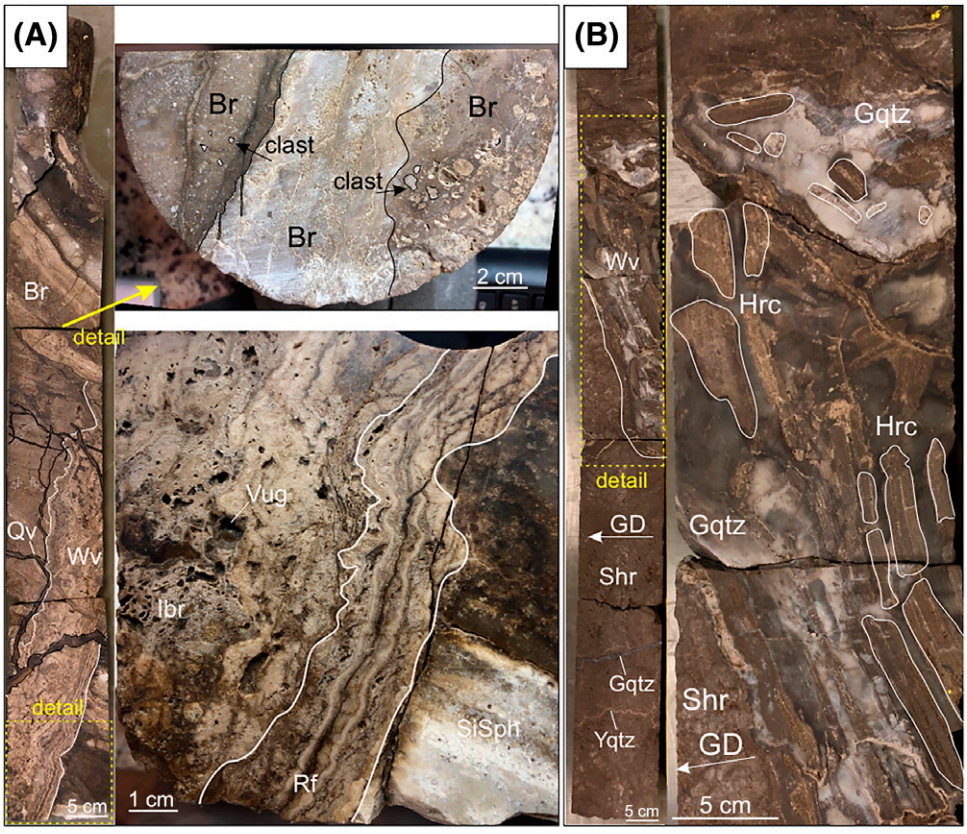

Figure 8. Wide brecciated crack-seal veins in well B. (A) Wide vein (Wv) with brecciated aspect and several phases of calcite cement. Contact with silicified spherulitestone (SiSph) host rock is irregular. Late quartz veins (Qv) cut wide calcite veins and host rock. Lower detail: Recracked fractures (Rf) formed by crack-seal and internal brecciation (IBr) appear to have been the predominant process. Upper detail: A breccia texture (Br) is observed just above the wide vein on the top of the core, showing rebrecciation evidence in the form of breccia clasts in younger breccias. (B) Wide brecciated vein with several clasts of host rock (Hrc) in the vertical position cemented with grayish quartz (Gqtz). On the top, the clasts lack organization. A shrubstone (Shr) is cut by the vein and shows horizontal shrub growth direction (GD). Yellowish quartz vein (Yqtz) cuts the shrubstone locally.

with swarms of narrow structures (<1 mm wide), with cataclastic internal structure that, based on their cataclastic texture, are possibly small displacement faults contemporaneous with the large fault and younger than the collapse breccias. Fault breccias can be composed of several different types of host rock clasts and rebrecciated breccias (breccia clasts within texturally younger breccia) that are cemented by calcite and quartz. Textural evidence of breccia clasts within fault breccia is compatible with recurrent brecciation. We observed clasts of older breccias within younger breccias, which is evidence of more than one brecciation episode (Figure 8A, top detail). These breccias appear to be organized in bands, and some of the clasts show a subrounded shape.

Narrower younger veins crosscut the wide veins and the host rock, dipping 20°–90°. These are often cemented by quartz or quartz plus barite (Figure 7D). It is common for these younger quartz veins to have variable dip angles and cut across previous veins (Figure 8A, Qv). Some quartz veins run parallel to the bedding in some locations. Barite mineralization occurred after quartz mineralization and fills remaining porosity in quartz veins or vugs, sometimes creating barite geodes when pores are large (>1 cm), with geodes showing preserved porosity even after cementation (Figure 7E).

Petrography—Asymmetric pore fillings occur as a geopetal feature at the bottom of pores and are made of microcrystalline calcite and microcrystalline quartz (Figure 9A, B). Microcrystalline calcite infill is commonly dolomitized and is crosscut by younger fractures filled with quartz. Calcite rims around breccia clasts and fractures from well B show radiaxial-fibrous texture (Figure 9A, D), and where present, geopetal microcrystalline calcite overlaps it.

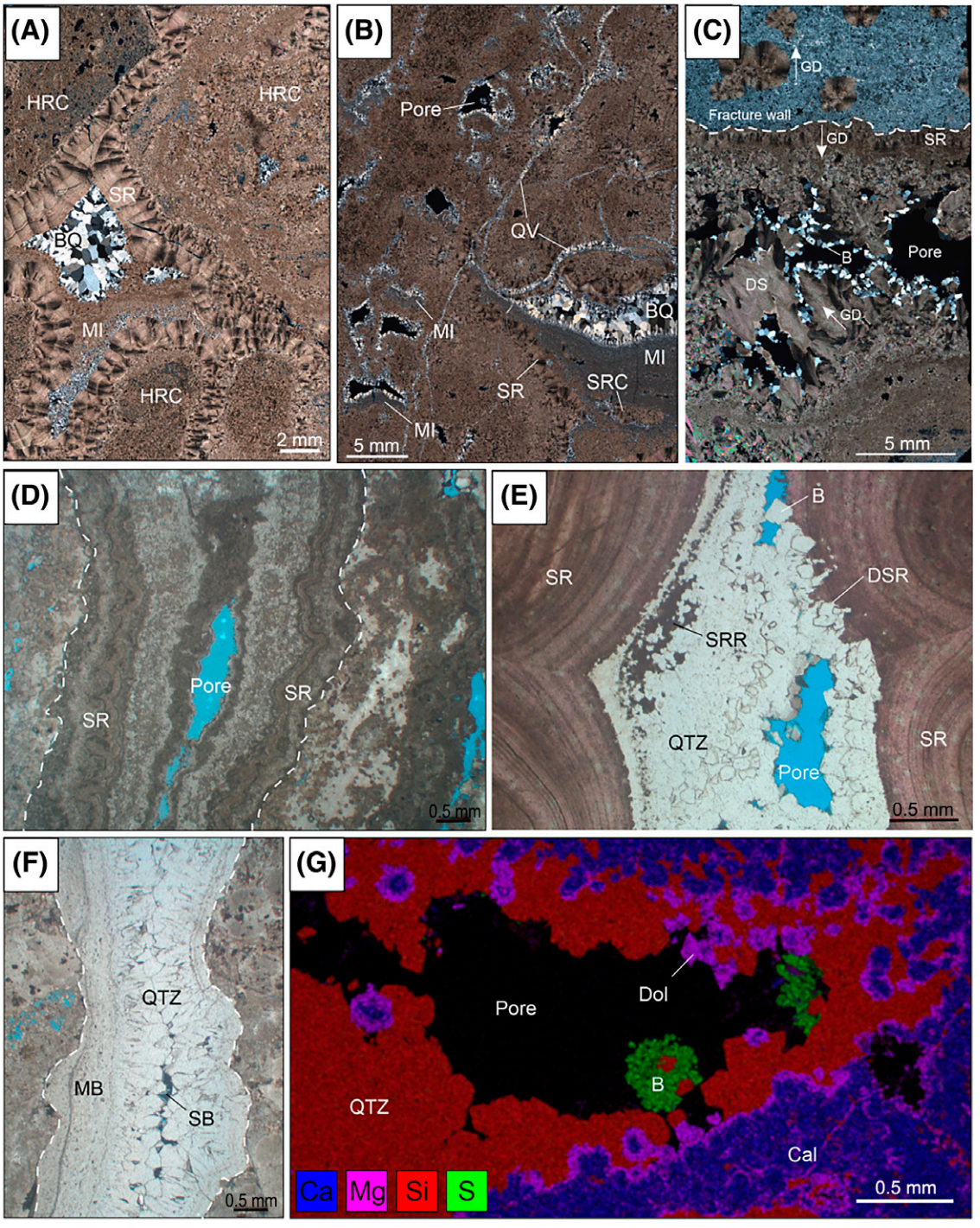

Figure 9. Photomicrographs from well B thin sections. (A) Host rock clasts (HRC) with radiaxial-fibrous calcite rims (SR). Breccia pores are filled by micritic infill (MI) forming a geopetal feature and megaquartz cement (BQ). (B) Vuggy pores and fractures cemented by quartz. Several pores have MI deposited at the bottom of the pore, followed by BQ. Quartz veins (QV) link vug networks and are cemented by the same quartz phase. Some vugs are rimmed by radiaxial-fibrous calcite (SR) and show clasts of radiaxial-fibrous calcite rim (SRC) floating in the MI. (C) Spherulitestone with a vuggy fracture filled with SR and barite (B). Spherulites were originally formed in a Mg-silicate clay matrix now substituted by quartz. The SR, dendritic calcite (DS), and spherulites show different growth directions (GD), marked by arrows. (D) Fracture filled by SR and showing preserved open aperture. (E) The SR showing dissolution features (DSR). Pore is filled by quartz (QTZ) and B. Radiaxial-fibrous calcite rim relicts (SRR) are preserved within QTZ cement. (F) The QTZ with solid bitumen (SB). Microbrecciation (MB) visible on the left wall. (G) Energy-dispersive x-ray spectroscopy map showing the presence of a calcitic host rock protolith (Cal), commonly substituted by dolomite (Dol) and cemented with QTZ and B.

Some quartz veins show scattered irregular pieces of fracture wall that we interpret to be dissolution features and relict of radiaxial-fibrous calcite rims partially dissolved and cemented by quartz (Figure 9E, SRR). Euhedral calcite is seen filling vuggy pores in host rock. Solid bitumen is commonly found filling remaining porosity in fractures (Figure 9F, SB). Dendritic calcite with variable growth directions fills vuggy fractures (Figure 9C). Barite precipitates on dendritic calcite or fill pores in combination with quartz cement and saddle dolomite in fault-related breccias (Figures 9G, 10D). Microbrecciation observed in some locations may be cataclastic, chemical wear, or hydraulic (Figure 9F, MB).

The fault surface observed in well B is cemented with minerals such as saddle dolomite, barite, and quartz (Figure 10D), which are exotic to the original calcitic host rock composition. The fault brecciated the host rock, and a quartz cement was deposited discontinuously between the clasts (Figure 10C). Large crystals of barite and saddle dolomite fill more than 50% of fault breccia pores. Shear dislocation is clearly seen in thin section (Figure 10B) and in core (Figure 10A) with associated brecciation.

Sequence of Events—The sequence of brittle deformation events in well B is shown in Figure 11. The brittle deformation sequence initiates with brecciation by collapse (Figure 11A). Collapse breccia clasts are rimmed by radiaxial-fibrous calcite. Pore space between clasts is infilled by a fine material deposited at the bottom, with silica filling the rest of the pores. Wide veins seem to be contemporaneous with collapse breccias and show crack-seal and internal brecciated texture. Younger fault-related breccias crosscut previous structures and show rebrecciation textures (Figure 11B). Microbrecciation is observed locally. Younger veins filled with barite and quartz crosscut all other older structures (Figure 11C). Locally, barite geodes are found where fracture widths are centimetric sized. Solid bitumen is found as the last phase filling fracture pores.

Fluid Inclusions

Fluid inclusions are hosted in quartz and barite cements (Figure 12; Table 2). The inclusions are two phase (liquid + vapor) and liquid rich at room temperature. A total of 68 inclusions were measured for total homogenization temperatures (T_h) reached by bubble disappearance. Unfortunately, we could not measure the eutectic temperature of any fluid inclusion, and in many cases final ice-melting temperature was not measured due to fluid inclusion small sizes.

Quartz-hosted fluid inclusions form both primary and secondary FIAs. Primary FIAs were found along quartz crystal growth zones or in small clusters within the nuclei of quartz crystals. The inclusions are usually rounded, but some have preserved rectangular shapes with sharp edges (Figure 12B). The T_h range from 73°C to 105°C, whereas ice-melting temperatures range from −17°C to −15.5°C, corresponding to fluid salinities ranging from 19 to 20 wt. % NaCl equivalent (Figure 12; Table 2).

Secondary FIAs comprise aqueous and oil inclusions found along microfractures or are dispersed in quartz crystals. The inclusions are rounded, with T_h ranging from 61°C to 107°C (Figure 12; Table 2).

Barite-hosted fluid inclusions also consist of both primary and secondary FIAs. Primary FIAs trapped aqueous and oil inclusions along barite crystal growth zones. The inclusions were mostly oval, with elongated shapes (Figure 12C, D), showing T_h ranging from 53°C to 74°C. Secondary FIAs were observed in fractures or isolated within the barite crystal. Usually, their shapes are oval or rounded, and they homogenize at temperatures ranging from 50°C to 58°C.

Overall, the T_h of quartz-hosted primary aqueous inclusion for well A range from 73°C to 105°C ($n = 34$), whereas in well B, the T_h of primary aqueous inclusions in quartz range from 54°C to 127°C ($n = 15$). In contrast, barite-hosted primary aqueous inclusions in well B show T_h ranging from 50°C to 80°C ($n = 8$). In comparison, the present-day temperature of the top interval of the Barra Velha Formation in the wells is ~70°C.

The bulk crush-leach analysis of the inclusions showed that noble gases have a heavy isotopic composition, with $^3He/^4He$ values of ~2.3 Ra—distinctly heavier than the air ratio $Ra = 1.39 \times 10^{-6}$. Halogen ratios (Na/Br and Cl/Br) show composition on the evaporitic trend for seawater (Figure 12E, F; Table 3).

O and C Isotopes

The $\delta^{18}O$ and $\delta^{13}C$ values (normalized to VPDB) of various carbonates range from 1.13‰ to 3.83‰, and from −1.29‰ to 2.19‰, respectively (Figure 13;

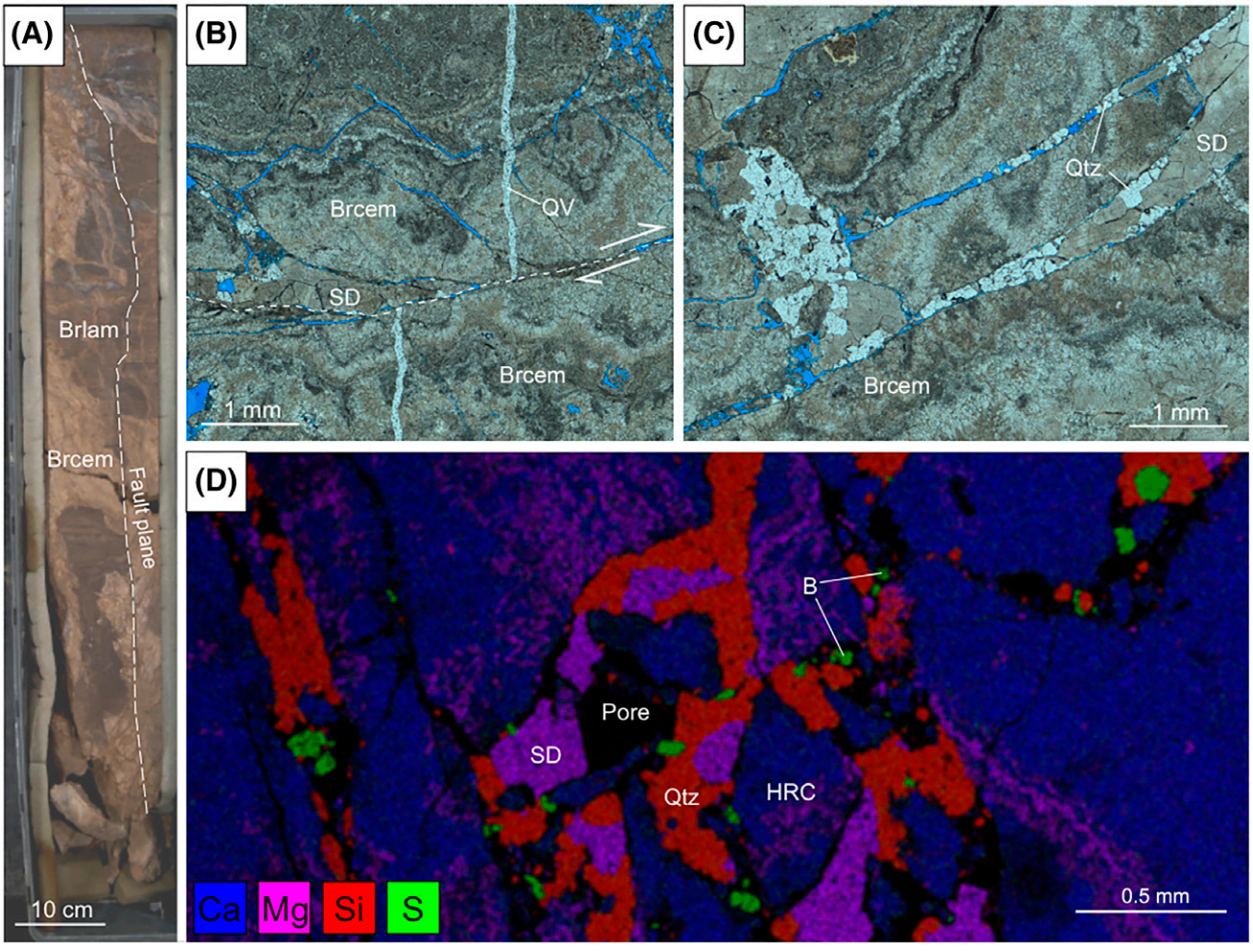

Figure 10. Photomicrographs of the normal-oblique fault zone in well B. (A) Core section where the fault was observed. It contains a brecciated laminate (Brlam) cemented with calcite (Brcem) and oblique striations on fault plane (see Figure 7C). (B) Plane-parallel transmitted light image showing quartz vein (QV) and Brcem sheared by the fault. The fault is mineralized with saddle dolomite (SD). (C) The Brcem filled with quartz (Qtz) and SD. (D) Energy-dispersive x-ray spectroscopy map showing porous fault breccia filled by Qtz, SD, and barite (B). HRC = host rock clast.

Table 4). The $\delta^{18}O$ composition is positive for studied samples. Variations in $\delta^{13}C$ are dependent on the host rock type and either show positive or negative values. For example, shrubstones in well A show the highest $\delta^{13}C$ values of up to 2.19‰, whereas spherulitestone has lower $\delta^{13}C$ values between 0.77‰ and 1.10‰, and laminite even shows negative $\delta^{13}C$ values in the range between −0.88‰ and −0.33‰. Radiaxial-fibrous calcite rims around collapse breccia clasts in well B also show negative $\delta^{13}C$ as low as −1.29‰. The microcrystalline calcite material infilling collapse breccia pores in well B has $\delta^{13}C$ values between 0.09‰ and 0.27‰. Data from previously published works are shown for comparison in the plot and suggest that our data plots on the high-end spectrum of $\delta^{18}O$ obtained for the Barra Velha Formation.

U-Pb Geochronology

We obtained 14 U-Pb ages for calcites and dolomite in host rock, breccias cements, and fractures and fault mineralizations from wells A and B (Table 5; Appendix). The oldest age obtained for a host rock is 116.6 ± 2.1 Ma, in a calcite spherulite (spherulite 1) from well A in an individual sample in the lower section of the Barra Velha Formation. Similar ages were obtained for host rock shrubs from the cored upper part of the Barra Velha Formation at 116.2 ± 2.8 Ma. These results are compatible with an Aptian age (i.e., 113.0–121.4 Ma) for the host rock. We measured U-Pb ages of spherulites at their centers and rims to test the difference in ages, being 116.6 ± 2.1 Ma (spherulite 1) and 113.9 ± 1.9 Ma at the rims

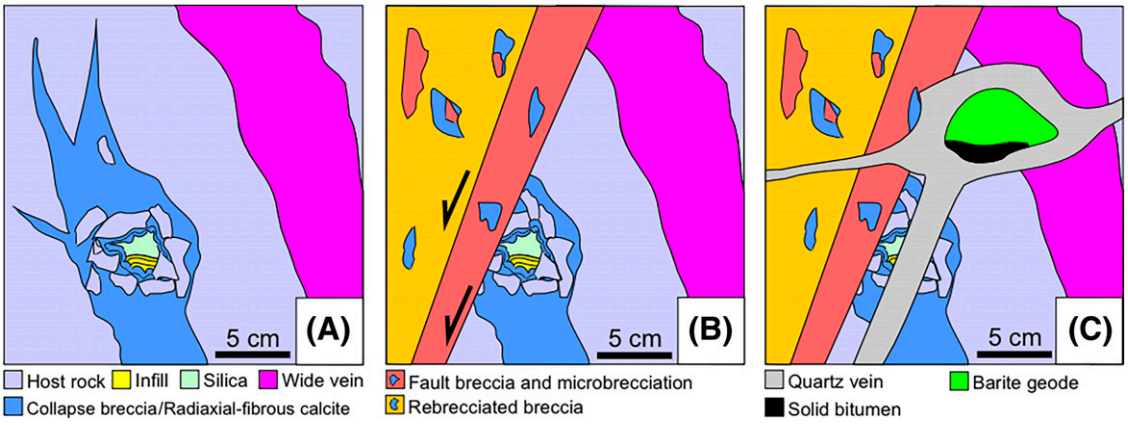

Figure 11. Sequence of brittle deformation events in well B based on crosscutting relationships. (A) Collapse breccia cemented by radiaxial-fibrous calcite rims around clasts. Breccia pores are filled by microcrystalline infill and silica. Wide veins also show internal brecciation and crack-seal texture. (B) Faulting, several generations of breccias and microbrecciation. Breccias have clasts from host rock and are commonly rebrecciated. (C) Quartz veins and barite geodes, which sometimes show solid bitumen fill.

(spherulite 2), and 114.7 ± 2.6 Ma at the center (spherulite 2). One sample in well A yields a younger age for a calcite shrub in host rock of 71.5 ± 5.7 Ma.

Dolomites that substitute infill geopetal material found in fractures show a very early age of 116.8 ± 1.7 Ma. Radiaxial-fibrous calcite rims around breccia clasts date to at least 108.7 ± 2.1 Ma, suggesting a difference in age to the host rock of 8 Ma. Microcrystalline calcite infill within breccia pores has a slightly younger age of 107.4 ± 2.3 Ma. Altered host rock clasts in breccias have an age of at least 101.9 ± 2.7 Ma, an age younger than the Aptian deposition that is interpreted to be due to alteration. Euhedral calcite cement found in well B host rock vugs has an age of 98.2 ± 5.2 Ma. Dolomite associated with the fault in well B was dated 95.1 ± 5.3 Ma.

At two locations in the chalcedony cement within the fractures of well A, we detected high amounts of uranium, reaching values of up to 2 ppm. Despite these local observations, high uranium content in chalcedony is unusual because its chemical composition does not include uranium either as a major component or as a minor substitution element.

DISCUSSION

Barra Velha Formation Age

Depositional Age and Uncertainties

Our host rock U-Pb ages are relevant to recent discussions about the age of the Barra Velha Formation. The Barra Velha Formation has been historically dated as Aptian by biostratigraphy (mostly ostracodes and pollen) or correlations with ^{40}Ar-^{39}Ar absolute ages from volcanic intrusions (Moreira et al., 2007).

Moreira et al. (2007) dated basalts contemporaneous to the Barra Velha Formation, obtaining an age of 117 Ma by the ^{40}Ar-^{39}Ar method, which is very close to the age we obtained for the host rock of the Barra Velha Formation (ca. 116 Ma). Louback et al. (2023) dated subaerial basalts in the Bacalhau oil field and obtained ages ranging from 109.9 ± 0.2 to 116.9 ± 0.2 Ma using the whole-rock ^{40}Ar-^{39}Ar dating method. Carbonate layers from the Barra Velha Formation are overlying these basalts, suggesting that the upper part of the Barra Velha Formation must have a maximum age of 116.9 Ma in this location. However, it is important to note that Moreira et al. (2007) did not provide the analytical data, hindering the assessment for the quality of the obtained age, and Louback et al. (2023) stated that their data are difficult to interpret because no age plateau exists.

However, recent studies based on planktonic foraminifera and correlation of δ^{13}C profiles of oceanic anoxic events in the Santos Basin and Tethyan sections constrained the overlying evaporite rock to be Barremian or lower Aptian (Tedeschi et al., 2017; Pietzsch et al., 2020; Sanjines et al., 2022), situating the Barra Velha Formation at a substantially older age than what studies based on U-Pb geochronology (Rochelle-Bates et al., 2022; Lawson et al., 2023) and current stratigraphic framework suggest (upper Aptian) (e.g., Moreira et al., 2007).

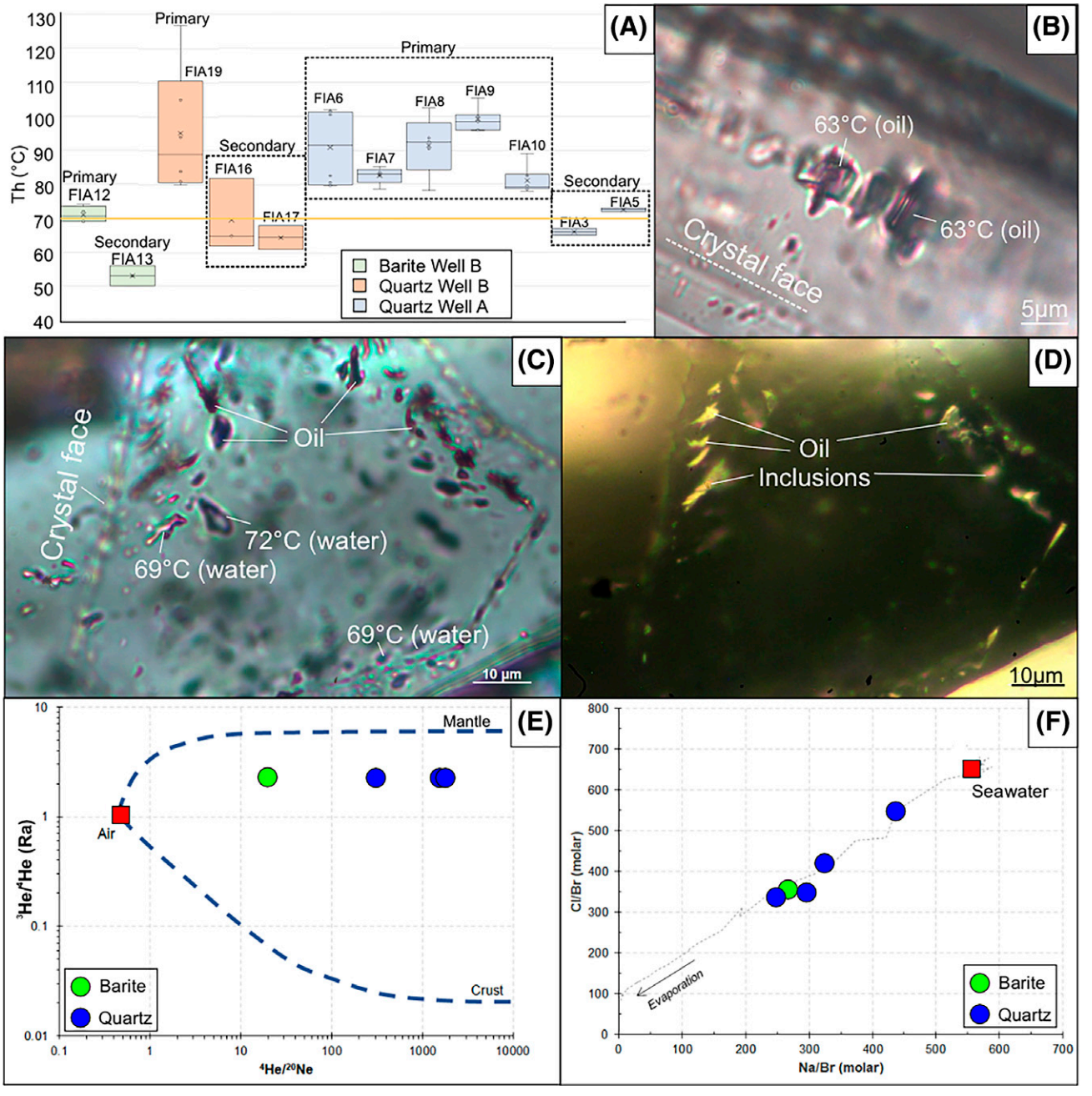

Figure 12. Fluid inclusion microthermometry and geochemical analysis from the Barra Velha Formation. (A) Boxplot showing homogenization temperatures (Th) of fluid inclusion assemblages (FIAs) hosted in barite and quartz cements. Yellow line shows temperature at Top Barra Velha Formation measured in the wells. (B) Primary oil inclusions in quartz in well B. (C) Primary inclusions of oil and water in barite cement filling vuggy porosity in well B. (D) Primary oil inclusions seen under ultraviolet light, showing yellowish fluorescence. (E) Graph of $^{3}He/^{4}He$ versus $^{4}He/^{20}Ne$. Air composition is shown by the red square. Mixing lines between air, crustal, and primordial He composition (mantle) are shown by dashed curves (Torgersen and Jenkins, 1982). (F) Graph of Cl/Br versus Na/Br. Seawater composition is shown by the red square. The dotted line shows seawater evaporation trend.

The U-Pb geochronology using LA-ICP-MS has only recently been used to date calcites from the Barra Velha Formation (Rochelle-Bates et al. 2022; Lawson et al., 2023; Brito et al., 2024). Rochelle-Bates et al. (2022) published the first U-Pb ages for the carbonates of the Barra Velha Formation. In their samples, they found ages to be consistently younger than the Aptian and concluded that the original depositional age was commonly erased by an Albian calcite recrystallization event, probably triggered by enhanced heat flow.

Table 2. Fluid Inclusion Microthermometry Data for the Barra Velha Formation, Santos Basin

Well	FIA	Mineral Host	Type	Fluid	T_h (°C)	T_m, ice (°C)
A	1	Quartz	Secondary	Aqueous	60	NA
A	2	Quartz	Primary	Aqueous	73	NA
A	3	Quartz	Secondary	Aqueous	67	NA
A	3	Quartz	Secondary	Aqueous	65	NA
A	4	Quartz	Secondary	Aqueous	107	NA
A	5	Quartz	Secondary	Aqueous	72	NA
A	5	Quartz	Secondary	Aqueous	73	NA
A	6	Quartz	Primary	Aqueous	81	−15.6
A	6	Quartz	Primary	Aqueous	80	−16
A	6	Quartz	Primary	Aqueous	83	NA
A	6	Quartz	Primary	Aqueous	80	NA
A	6	Quartz	Primary	Aqueous	101	−17
A	6	Quartz	Primary	Aqueous	102	−16.5
A	6	Quartz	Primary	Aqueous	102	NA
A	6	Quartz	Primary	Aqueous	101	−15.5
A	7	Quartz	Primary	Aqueous	85	−16.2
A	7	Quartz	Primary	Aqueous	83	−15.8
A	7	Quartz	Primary	Aqueous	84	−16
A	7	Quartz	Primary	Aqueous	83	NA
A	7	Quartz	Primary	Aqueous	79	−16
A	8	Quartz	Primary	Aqueous	78	NA
A	8	Quartz	Primary	Aqueous	93	NA
A	8	Quartz	Primary	Aqueous	94	−16.5
A	8	Quartz	Primary	Aqueous	91	NA
A	8	Quartz	Primary	Aqueous	103	−16.5
A	9	Quartz	Primary	Aqueous	100	NA
A	9	Quartz	Primary	Aqueous	105	−16
A	9	Quartz	Primary	Aqueous	101	−16.8
A	9	Quartz	Primary	Aqueous	96	−16.3
A	9	Quartz	Primary	Aqueous	99	−16.9
A	9	Quartz	Primary	Aqueous	99	−15.8
A	9	Quartz	Primary	Aqueous	96	NA
A	10	Quartz	Primary	Aqueous	80	−15.5
A	10	Quartz	Primary	Aqueous	78	NA
A	10	Quartz	Primary	Aqueous	79	NA
A	10	Quartz	Primary	Aqueous	79	−15.5
A	10	Quartz	Primary	Aqueous	79	−15.8
A	10	Quartz	Primary	Aqueous	83	NA
A	10	Quartz	Primary	Aqueous	83	−16.2
A	10	Quartz	Primary	Aqueous	89	−15.8
B	11	Barite	Primary	Aqueous	80	NA
B	12	Barite	Primary	Aqueous	69	NA
B	12	Barite	Primary	Aqueous	72	NA
B	12	Barite	Primary	Aqueous	69	NA
B	12	Barite	Primary	Aqueous	74	NA
B	13	Barite	Secondary	Oil	58	NA
B	13	Barite	Secondary	Oil	55	NA
B	13	Barite	Secondary	Aqueous	56	NA
B	13	Barite	Secondary	Aqueous	53	NA
B	13	Barite	Secondary	Aqueous	50	NA
B	14	Barite	Primary	Aqueous	53	NA
B	15	Barite	Primary	Oil	63	NA
B	15	Barite	Primary	Oil	63	NA
B	16	Quartz	Secondary	Aqueous	65	NA
B	16	Quartz	Secondary	Aqueous	82	NA
B	16	Quartz	Secondary	Aqueous	62	NA
B	16	Quartz	Secondary	Oil	69	NA
B	17	Quartz	Secondary	Aqueous	68	NA
B	17	Quartz	Secondary	Aqueous	61	NA
B	18	Quartz	Primary	Aqueous	86	NA
B	19	Quartz	Primary	Oil	60	NA
B	19	Quartz	Primary	Oil	54	NA
B	19	Quartz	Primary	Aqueous	81	NA
B	19	Quartz	Primary	Aqueous	84	NA
B	19	Quartz	Primary	Aqueous	105*	NA
B	19	Quartz	Primary	Aqueous	127*	NA
B	19	Quartz	Primary	Aqueous	80	NA
B	19	Quartz	Primary	Aqueous	94	NA

Abbreviations: FIA = fluid inclusion assemblage (sensu Goldstein, 2001); NA = not acquired; T_h = homogenization temperature; T_m = melting temperature.

*May represent temperatures affected by posttrapping modifications, such as stretching.

Lawson et al. (2023) reported petrographic, geochronologic, and isotopic results for two samples from different locations in the Santos Basin. They obtained ages for the Barra Velha Formation of 114.5 ± 4.7 and 109.7 ± 9.3 Ma based on the LA-ICP-MS method and 115.8 ± 1.6 Ma based on the isotope dissolution method. Reported $^{87}Sr/^{86}Sr$ ratios of 0.7141 and 0.7134 and clumped isotope temperatures lying between 60°C ±6°C and 45°C ±5°C are interpreted as not being representative of depositional conditions. However, the authors concluded that the combination of petrography and isotopic analysis suggested that these rocks have experienced only minor levels of early burial diagenesis and that the U-Pb ages obtained can be interpreted as depositional, with the Barra Velha Formation being deposited during the late Aptian.

Lastly, Brito et al. (2024) reported several ages from the Barra Velha Formation, ranging from 125 to 82 Ma. They identified dolomite cements with older ages (125 ± 3 to 122 ± 4 Ma) than primary calcite components in the host rock (116 ± 2 to 110 ± 2 Ma), suggesting that the carbonate host rocks did not

Table 3. Noble Gas and Halogen Geochemistry Analysis of Fluid Inclusions from the Barra Velha Formation

Well Name	Mineral	$^{3}He/^{4}He$ (Ra)	$^{4}He/^{20}Ne$	Na, ppb	K, ppb	Li, ppb	Cl, ppb	Br, ppb	Na/Br, M	Cl/Br, M
B	Barite	2.28 ± 0.04	19	1688	340	6	3466	22	266.5	355.1
B	Quartz	2.32 ± 0.11	1780	2154	190	8	4510	30	249.4	338.8
B	Quartz	2.32 ± 0.05	1538	1886	200	8	3654	15	436.8	549
B	Quartz	2.33 ± 0.05	306	1025	150	5	1862	12	296.7	349.7
B	Quartz	–	–	1124	155	5	2246	12	325.4	421.9

preserve their pristine U-Pb geochemical signature. The reset of U/Pb ratios may have been triggered by the gain of U or the loss of Pb during diagenesis and hydrothermal alteration.

Our U-Pb ages for host rock calcite shrubs and spherulites from well A range from 113.9 ± 1.9 to 116.6 ± 2.8 Ma, an age range similar to that reported by Lawson et al. (2023) and Brito et al. (2024) and compatible with a late Aptian age. The U-Pb calcite geochronology results can be affected by calcite recrystallization that can open the system and reset the U/Pb ratios. Thus, caution must be exercised in regions of the Barra Velha Formation that have been affected by intense diagenesis. Lima et al. (2020) showed negative $\delta^{18}O$ values between −5.70‰ and −1.93‰ for fascicular calcites in host rock shrubs of the Aptian Macabu Formation in Campos Basin, which suggests recrystallization, because it shows a lower isotopic ratio than positive primary evaporitic signatures. A similar process may occur in the Barra Velha Formation because they are analogous formations from neighboring basins. However, for our dated depositional features, both the shrub and the spherulite show only minor alterations and lack textural evidence for widespread recrystallization when observed under transmitted light and cathodoluminescence (Figure 5).

Because both ^{40}Ar-^{39}Ar and U-Pb ages are suitable for recording alteration ages, dedicated studies to assess the quality of these geochronometers within the conditions of the Barra Velha Formation must be developed to achieve a consensus for its

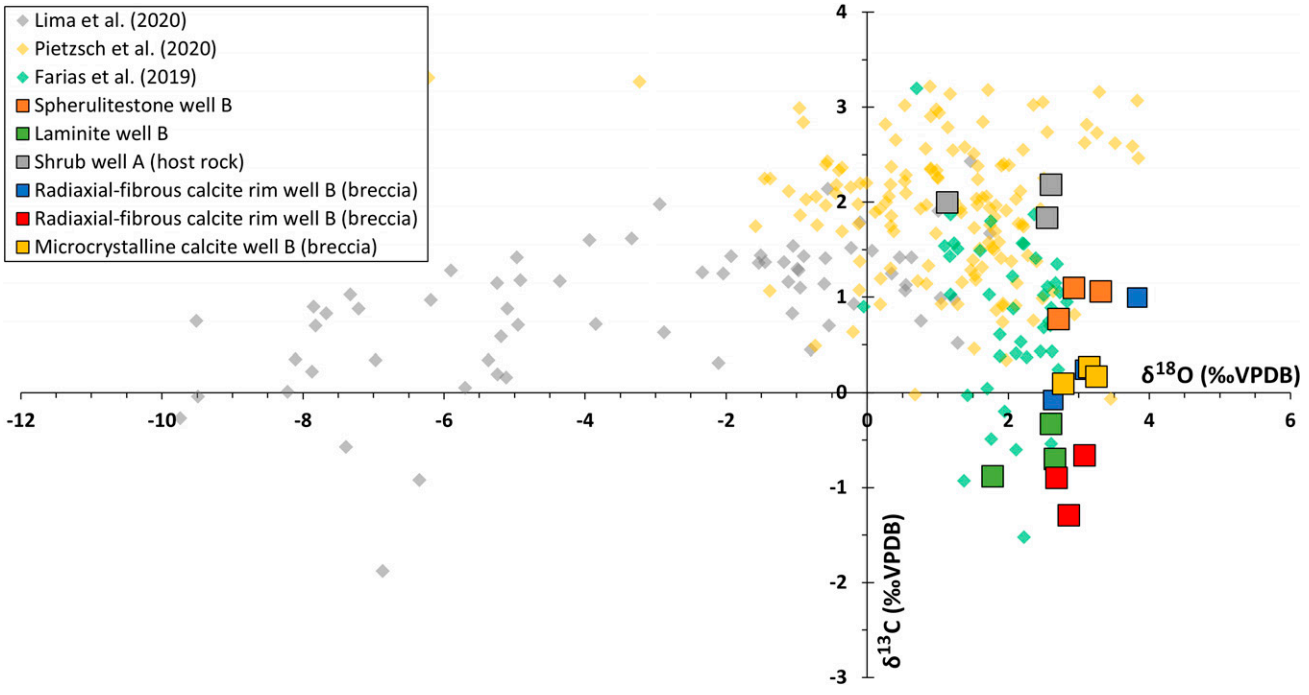

Figure 13. Carbonate isotope compositions (‰VPDB [Vienna Peedee belemnite]). All samples have positive $\delta^{18}O$, a common feature in evaporitic settings. Most samples also have $\delta^{13}C^{+}$, except for laminate host rock and radiaxial-fibrous calcite rims from collapse breccias. Data adapted from Farias et al. (2019), Lima et al. (2020), and Pietzsch et al. (2020) are shown for comparison.

Table 4. $\delta^{18}O$ And $\delta^{13}C$ Results Obtained from Well A and Well B for Target Mineral Features in the Barra Velha Formation

Well Name	$\delta^{13}C$ (‰ VPDB)	$\delta^{18}O$ (‰ VPDB)	Type
A	2.00	1.13	Shrubstone host rock
A	2.19	2.61	Shrubstone host rock
A	1.84	2.55	Shrubstone host rock
B	1.06	3.30	Spherulitestone host rock
B	0.77	2.71	Spherulitestone host rock
B	1.10	2.93	Spherulitestone host rock
B	−0.70	2.66	Laminite host rock
B	−0.33	2.61	Laminite host rock
B	−0.88	1.77	Laminite host rock
B	−0.08	2.64	Radiaxial-fibrous calcite rim (collapse breccia in spherulitestone)
B	0.24	3.09	Radiaxial-fibrous calcite rim (collapse breccia in spherulitestone)
B	0.99	3.83	Radiaxial-fibrous calcite rim (collapse breccia in spherulitestone)
B	−0.90	2.69	Radiaxial-fibrous calcite rim (collapse breccia in laminite)
B	−1.29	2.86	Radiaxial-fibrous calcite rim (collapse breccia in laminite)
B	−0.66	3.08	Radiaxial-fibrous calcite rim (collapse breccia in laminite)
B	0.27	3.15	Infill (collapse breccia in spherulitestone)
B	0.17	3.25	Infill (collapse breccia in spherulitestone)
B	0.09	2.78	Infill (collapse breccia in spherulitestone)

Abbreviation: VPDB = Vienna Peedee belemnite.

depositional age. Due to the lack of evidence for a widespread recrystallization episode in our samples, we infer that the ages we obtained are representative of the depositional age of the Barra Velha Formation host rock, although we recognize the risk of recrystallization or U/Pb reset affecting our samples because we did not have a $\delta^{18}O$ analysis on our host rock calcite shrub samples to assess its geochemical preservation.

Possibilities for Age Variation

It is important to note that the age obtained in the Barra Velha Formation may vary depending on the depth of the sample and distance from the evaporite rocks. The age we obtained for spherulites (113.9 to 116.6 Ma) is close to the age of the calcite shrub (116.2 Ma), although they are from different depths (~250 m [~820.2 ft] apart) and from different sections in the upper and lower Barra Velha Formation.

Table 5. U-Pb Calcite Geochronology Results for Target Mineral Features from the Barra Velha Formation

Well Name	Feature	Age, Ma	2σ Error, m.y.	MSWD	Number of Spots
A	Spherulite 1 rim (host rock)	116.6	2.1	1.4	26
A	Spherulite 2 center (host rock)	114.7	2.6	1.4	17
A	Spherulite 2 rim (host rock)	113.9	2	1.1	17
A	Shrub (host rock)	116.2	1.4	5.7	25
A	Shrub (recrystallized host rock)	71.5	5.7	4.2	25
A	Dolomite (substitution)	116.8	1.7	6.1	35
B	Radiaxial-fibrous calcite rim (collapse breccia)	108.7	2.1	1.4	28
B	Radiaxial-fibrous calcite rim (collapse breccia)	108	4.5	0.7	26
B	Radiaxial-fibrous calcite rim (collapse breccia)	105.8	4.2	1.2	32
B	Infill (collapse breccia)	107.4	2.3	1.8	20
B	Altered host rock	101.9	2.7	1.3	27
B	Altered host rock	97.7	4.2	10	26
B	Euhedral calcite (vug)	98.2	5.2	2.1	23
B	Saddle dolomite (fault breccia)	95.1	5.3	1.8	33

Abbreviation: MSWD = mean squared weighted deviation.

There are at least three explanations for this age similarity in different depths.

1. Widespread recrystallization of the Barra Velha host rock would reset U-Pb ratios and erase age differences to the same recrystallization age. This would make samples from different depths and with different depositional ages be of the same age after recrystallization, when analyzed using U-Pb geochronology.
2. Spherulites are typically depicted as diagenetic concretions (e.g., Lima and De Ros, 2019), grown in an early eodiagenetic environment. The fact that the spherulites grow during diagenesis may explain why the age is like that of the shrubs in the upper section, because they grow late in relation to actual host rock deposition. The spherulites in the lower sample could have been growing as an eodiagenetic concretion contemporaneously with the shrubs in the upper sample.
3. A rapid deposition rate would decrease the age variation between these two samples. The fact that the samples were obtained from a mounded carbonate in well A may suggest a faster deposition rate than the common Barra Velha Formation (not mounded). The deposition rate in carbonate mounds could be influenced by enriched fluids sourced by the underlying faults and hydrothermal vents, which could increase the deposition rate locally.

The difference in age between spherulite rim (spherulite 2) (113.9 ± 2.0 Ma) and center (114.7 ± 2.6 Ma) is small, suggesting that the process of nucleation and growth of spherulites is fast, considering that our obtained ages are depositional (or early diagenetic for spherulites). Two spatially separated spherulite rims (spherulites A and B) (Figure 11B; Table 5) differ by ~2.7 m.y., although the discrepancy comes close to the (2σ) age uncertainty (2.1 and 2.0 m.y., respectively). Further systematic high-resolution dating would be needed to test the hypothesis of diachronous episodic diagenetic/chemical reactions forming spherulites (e.g., Wright and Barnett, 2015).

We also found a younger age in host rock shrub from well A at 71.5 ± 5.7 Ma during the Maastrichtian (Late Cretaceous), probably related to recrystallization, and in altered host rock breccia clasts from well B at 97.7 ± 4.2 and 101.9 ± 2.7 Ma during the Cenomanian/Albian. In this case, the younger recrystallized shrub shows large areas with dark luminescence, suggesting that here a widespread recrystallization or alteration episode occurred, near a fracture (Figure 5C). Although the recrystallization episodes we found may be related to modifications related to burial, hydrothermal alteration, or volcanism, the reason can only be determined with additional geochemical and petrographic evidence.

Two of our recrystallization ages are close to those found by Rochelle-Bates et al. (2022) during the Albian. These results reinforce evidence for recrystallization in the Albian. However, this does not exclude younger recrystallization events that may have happened during the Maastrichtian, as shown by our sample dated at ca. 71 Ma. As we discuss, if recrystallization is related to discrete flow events and enhanced heat flow (possibly through faults triggered by hydrothermal alteration or magmatic events), then multiple spatially and temporally distinct recrystallizations may have occurred.

Another possible interpretation for this younger shrub age is formation by diagenetic fluids percolating the host rock. In well B, it is possible to identify dendritic calcite growing inside vugs with variable growth direction, indicating a younger diagenetic formation (Figure 9C, DS). In other parts of the Barra Velha Formation, different types of calcite textures can be associated with different processes of formation (Rodríguez-Berriguete et al., 2022), which may include diagenesis. In the core, we observed shrubstones with horizontal growth direction (Figure 8B), a position not usually described for depositional shrubs in the Barra Velha Formation. These different mechanisms of shrub formation would also create age discrepancies.

Brittle Structure and Hydrothermal Alteration

Structural Characterization

We observed in both wells the presence of brittle structures and bed tilting that showed that the Barra Velha Formation experienced substantial deformation during burial. We discuss below, based on the structural data observed in the core, that the genesis of the fractures could be associated with both burial and fault deformation.

Burial-related fractures usually have a regular geometric relationship perpendicular to bed interfaces

that act as a mechanical boundary. It is a common feature of burial fractures to be influenced by beds, usually resulting in bedding perpendicular opening-mode fractures that may show some degree of regular spacing (e.g., Narr and Suppe, 1991). Core fractures have a range of dip angles (20° to 90°), and most of them are opening-mode fractures. In some cases, it is possible to observe bed-perpendicular configurations (Figure 3F). Where the perpendicular orientation relative to bedding remains, varying fracture dips may be related to the bedding tilt that also may have tilted early fractures. We infer that part of the fracture population formed as bed-perpendicular opening-mode fractures in a burial setting. During subsequent deformation, some of these fractures were later rotated along with enclosed beds.

Deformation caused by fault zones is another possible reason for the formation of fractures in the Barra Velha Formation (Fernández-Ibáñez et al., 2022b, Wennberg et al., 2023, Mendes et al., 2024). The presence of faults in core (and on seismic profile) and high bedding dip angles (up to 70°) are compatible with fault deformation. The wide range of bed tilt values within cores could reflect fault displacement. A striated fault plane is present in the cored interval in well B. This fault shows a steep dip angle (85°) and a normal-oblique striation (73° of rake), suggesting a transcurrent component of motion that is compatible with the high angle of faults observed in seismic lines (Figure 2). These faults caused part of the brittle deformation observed in the reservoir and affected the evaporite section as well, as evidenced by the faulted Barra Velha Formation top (Figure 2). Fault zone architecture comprising a damage zone that envelops a fault core where slip is usually concentrated and creates cataclastic texture (e.g., Caine et al., 1996) may account for the presence of fault breccias in the cores. Many oblique fractures and small faults may be parts of damage zones surrounding faults or being part of a fault core, where cataclastic textures prevail.

In this interpretation, subsidiary small displacement faults with cataclastic fill such as those observed in core and petrography (Figure 3E, Sf) could be created by slip of a network of larger faults, like the faults imaged in seismic section (Figure 2). The narrow fractures observed in the core in micropetrography have cataclastic fill. These cataclastic zones are cut by later quartz veins (Figure 4E). This suggests the presence of shear deformation, probably linked to faults, during an early stage.

Brecciation Environment

The difference in age between radiaxial-fibrous calcite rims (Figure 7A) on the collapse breccia clasts (ca. 108 Ma) and spherulite and shrub in the host rocks (ca. 116 Ma) shows that the formation of these collapse breccias happened no more than approximately 8 m.y. after the deposition of the host rock. The process of brecciation is probably related to collapse of an open cavity that occurred in a shallow burial setting, as burial was slowly increasing during the sag phase of the basin in which the Barra Velha Formation was depositing (e.g., Moreira et al., 2007; Wright, 2022). Recent estimates for the deposition rate of the Barra Velha Formation range between 54 and 80 m/m.y. (Pietzsch et al., 2018; Farias et al., 2019). Considering the 8 m.y. of difference between radiaxial-fibrous calcite rims around breccia clasts and host rock age, the breccias would have been formed at a maximum burial depth range of 432 to 640 m, but possibly much shallower and younger because the age of the radiaxial-fibrous calcite rim is a maximum limit for the age of brecciation, which must have occurred before. The common presence of geopetal features formed by the infill of microcrystalline calcite and quartz in breccia pores and veins is evidence of the percolation of sediment through the fracture/breccia network or decantation of small broken fragments of the brecciation process in the pores, which also points toward a shallow burial environment and reinforces the interpretation of a collapse breccia (e.g., Shukla and Sharma, 2018).

Radiaxial-fibrous calcite forms, such as the ones coating the collapse breccia clasts, are usually interpreted as being related to supersaturation in calcite (e.g., Richter et al., 2011; Pietzsch et al., 2022), and geochemically, the radiaxial-fibrous calcite rims in the collapse breccias are like the host rock shrubs. The isotope data of radiaxial-fibrous calcite rims around collapse breccia clasts (Figure 13; Table 4) show positive $\delta^{18}O$ (2.64‰ to 3.83‰), suggesting deposition from evaporitic waters with composition similar to that of the host rock shrub (1.13‰ to 2.61‰). However, the $\delta^{13}C$ is lower than the shrubstone values and closer to the laminate host rock values, which may indicate some residence time of fluids in the subsurface in contact with laminites,

because these show a lower $\delta^{13}C$ ratio due to microbial influence (Souza et al., 2018). Thus, the presence of radiaxial-fibrous calcite rims in collapse breccias may be evidence of cementation by fluids with composition close to the evaporitic surficial lake waters that deposited the host rock and for a shallow brecciation during early burial (~400–600 m [~1312–1968.5 ft] of maximum depth).

The $\delta^{18}O$ fractionation from water to calcite depends on temperature, and thus the estimation $\delta^{18}O_{water}$ composition may be different from the obtained $\delta^{18}O_{calcite}$ composition. We estimated $\delta^{18}O_{SMOW\text{-}water}$ (standard mean ocean water [SMOW]) for the range of $\delta^{18}O_{VPDB\text{-}calcite}$ obtained in our study, using conversion equations in O'Neil et al. (1969) and 40°C of temperature. We obtained a range of $\delta^{18}O_{SMOW\text{-}water}$ between 7.5‰ and 10.3‰, which reinforces the interpretation of evaporitic origin for the parental fluids.

In well B, the textural evidence of collapse breccias rimmed by radiaxial-fibrous calcites includes filled cavities with cracks that propagated through the host rock and fallen clasts that deposited at the bottom of the cavities created by the brecciation (Figure 7A). These textures suggest that these collapse breccias probably initially formed by ascending fluids associated with chemical corrosion dissolving surrounding host rock or shallow karstification that opened a cavity, which was later collapsed and cemented during early burial.

Vent and Fault Conduits

Vents are commonly found along faults in lakes of rift basins and are usually associated with carbonate mounds (e.g., Renaut et al., 2013; Dekov et al., 2014; DeMott and Scholz, 2020; DeMott et al., 2021). Mercedes-Martín et al. (2019) proposed, based on chemical modeling, that vents actively controlled lake water composition with silica input during the deposition of the Barra Velha Formation, but the existence of vent conduits was never proved with rock data. Vital et al. (2023) suggested that carbonate towers within the Barra Velha Formation represent outbreak of geothermal fluids enriched in Ca^{2+} and HCO_3^- along deep-seated faults. Strugale et al. (2024) suggested that in the Campos Basin, deep-seated faults reactivated during the postrift sequence (i.e., contemporaneous with the Barra Velha Formation) may be controlling the ascension of hot fluids that triggered the formation of mounds and a syndepositional hydrothermal event (Barremian-Aptian diagenetic event), constrained by U-Pb ages, petrography, and fluid inclusion temperatures.

For the well B core, we described ~12-cm-wide veins showing a crack-seal texture that represents repeated fracture opening (Figure 8). The width of these veins is much larger than that of any other fracture found elsewhere in the reservoir, setting these structures apart from the other fractures. Large crack-seal veins are commonly found in fault zones (e.g., Bastesen and Braathen, 2010; Balsamo et al., 2019) and may be formed by cyclical variations in fluid pressure (Petit et al., 1999). The large width, internal brecciated fabrics, presence of vertically rotated fragments of host rock bedding, and crack-seal texture are also compatible with these veins being fluid escape structures enlarged by reactivation, usually caused by energetic fluid ascent and high pressure, the diagnostic features of fluid conduits. We interpret these structures to be hydrothermal vent conduits that were reactivated many times, allowing fluids to ascend to the surface in a hot springs setting. Such vents are commonly associated with spring mounds and hydrothermal overpressured fluid injection (e.g., Della Porta, 2015; Brogi et al., 2017), such as the ones observed in seismic line (Figure 2, mound). These vents may have been initiated by faults and may be part of a fracture network along a damage zone, later used by fluids as a recurrent path. The wide veins are cemented with calcite or quartz, suggesting that the composition of the vent fluids was variable. The pattern contrasts with the generally simpler mineral deposit sequences in some regional tectonic fractures in which ambient fluids and local diffusion may dominate precipitation (e.g., Laubach et al., 2019; Denny et al., 2020).

The presence of carbonate mounds in the Barra Velha Formation has previously been described (e.g., Buckley et al., 2015; Corrêa et al., 2019; Simo et al., 2019; Mendes et al., 2022; Zeller et al., 2022), but our observation is the first interpretation of vent conduits in cores, which we infer to have actively conducted ascending fluids, possibly using fault zones, to modify shallow portions of the Barra Velha Formation or to reach the surface, where it formed carbonate mounds. Although the upper part of the Barra Velha Formation historically has been depicted as a postrift or sag phase deposit (Moreira et al. 2007), some authors have

shown evidence of active tectonism synchronous to the upper Barra Velha Formation deposition (Karner and Gambôa, 2007; Adriano et al., 2022). Evidence from cored rock data showing soft sediment deformation structures triggered by early/syndepositional fault movements reinforce the interpretation of active faults during the deposition of the upper section of the Barra Velha Formation in some parts of the Santos Basin (Terra et al., 2024).

Farias et al. (2019) estimated calcite crystallization temperatures in the Barra Velha Formation using clumped isotope thermometry. The range of temperatures obtained varies from 46°C to 73°C, suggesting that calcite precipitated from hot springs. Although clumped isotope thermometry currently may suffer from calibration uncertainties, we believe that these temperatures support our interpretation of vents with hot fluids having occurred locally in the Barra Velha Formation. These vents probably formed part of the carbonate reservoir, through the deposition of spring mound carbonates (e.g., Della Porta, 2015), and could have contributed to early or postburial diagenetic and hydrothermal modifications. These vent-related features would be localized where fault zones allowed fluids to rise up toward shallow portions but would not exist where deep-reaching faults were not present, a situation in which the deposition of common alkaline-lake Barra Velha Formation facies would prevail without significant hydrothermal modifications and spring mound deposits. Even though the Barra Velha facies is usually described as alkaline-lake deposits (Wright and Barnett, 2015), recent analogues in the East African Rift and the Basin and Range (United States) show that these types of deposits coexist with localized spring mounds and travertine deposits rooted by fault zones that actively conduct uprising fluids (e.g., Renaut et al., 2013; Dekov et al., 2014; Guo and Chafetz, 2014; Della Porta, 2015).

We observed dendritic calcite growing in vuggy fractures in well B, followed by barite mineralization (Figure 9C). In this context, the dendritic shape is different from the host rock shrubs and radiaxial-fibrous calcite rims in collapse breccias, displaying more elongated shapes and varied growth direction. The dendritic calcite appear to be a phase of cement filling vugs. The occurrence of dendritic shape in calcites within the Barra Velha Formation has been described as associated with deposition in hydrothermal, travertine, or spring mound settings (Della Porta et al., 2017; Rodríguez-Berriguete et al., 2022). The dendritic shape may suggest proximity to vents or hot springs that would allow deposition of this distinct shape inside the vuggy pores.

Another interesting aspect is the horizontal shrub growth direction observed in the core of well B (Figure 8B). There are at least four interpretations for this feature.

1. This growth direction is primary, which would suggest growth in a mounded surface with inclination, other than the lake bottom.
2. The horizontal shrub is a rotated clast in a rudstone or collapse/sedimentary breccia. The clast could have been rotated during deposition and be cut by the wide vein later during burial.
3. The original shrubstone suffered hydraulic brecciation, which would imply an energetic fluid uprise, causing breakage and rotation.
4. The shrubstone was rotated during fault brecciation. However, we do not see evidence of cataclasis or intense fault deformation in this specific location.

The depositional ages obtained for the host rock within the carbonate mound in well A (116.2 ± 2.8 Ma) and for the evaporitic radiaxial-fibrous calcite rim cement within collapse breccias in well B (108.7–105.8 Ma) are close to or contemporaneous with the estimated age for the start of evaporite deposition and marine incursions in the Santos Basin at 113 Ma (Moreira et al., 2005). This implies that the hydrothermal vents may have been active, connected to the lake waters, and possibly feeding spring mounds contemporaneously with the deposition of the Ariri Formation.

Although there are controversial interpretations about the real topographic expression of the Barra Velha Formation mounds during deposition, observations in seismic lines indicate that the well A mounded feature is more than 400 m high. The pinnacle shape usually indicates a subaqueous environment that would allow the preservation of such geometry (Pentecost, 2005). Modern analogous subaqueous mounds can be seen in dry lakes such as the three United States lakes, Searles, Pyramid, and Mono, and Abbé Lac (Djibouti), with reliefs reaching more than 40 m high (e.g., Della Porta, 2015). However, there is no information about how much

of these modern mounds is under the surface, having been buried by younger lake sediments. Shallower regions on top of the pinnacles would allow preferential anhydrite accumulation, whereas deeper portions would be suitable for accumulating more soluble evaporites such as halite (e.g., Tucker, 1991).

Exotic Mineralogy and Fillings

The mineralogy including barite, saddle dolomite, and quartz found in the fractures and in fault breccias is evidence of the participation of external fluids because they are chemically exotic to the geochemistry of the lake, host rock, or burial waters (e.g., Griffith and Paytan, 2012). The barite mineralization found in faults and fractures is not an original part of the calcitic host rock chemical composition. The presence of the exotic barite phase implies that mineralization must have had a deep fluid source that interacted with magmatic or basement rocks to yield the necessary barium source, and that it most likely subsequently rose through faults where mixing with sulfate infiltrated by seawater precipitated the barite. This is also supported by the low Na/Br and Cl/Br ratios observed in fluid inclusions. Dissolution of the overlying evaporites (anhydrite) is another possible mechanism to obtain a sulfate source. Although not confirmed in our study, evaporite dissolution is a mechanism that has been described as occurring in other areas of the Brazilian pre-Salt (e.g., Lima et al., 2020). This mechanism is commonly found in Mississippi Valley–type barite mineral deposits (e.g., Hanor, 2000) and is described to have yielded barite mineralizations in related Cretaceous African basins by hydrothermal alteration (e.g., Oden et al., 2015).

The barite found in the fault zone in well B core was precipitated along with saddle dolomite (Figure 10D), a mineral described as a key indicator of hydrothermal mineralizations, due to its distinct shape formed by rapid precipitation rate at temperatures above 50°C (Davies and Smith, 2006). Considering the U-Pb age of 95 Ma obtained from the saddle dolomite, it can be assumed that the process of hydrothermal mineralization of the fault zone at well B must have occurred during the Cenomanian (93.9–100.5 Ma), close to this age or before, seawater infiltrated through the fracture network into the carbonate mounds within the Barra Velha Formation, providing a sulfate source for barite mineralization. Before the seawater incursions in the Santos Basin, barite had not precipitated due to the lack of necessary sulfur. This may explain why barite is a late cement phase in fractures and is not present in early cementation phases. The high salinity and ion composition plotting on seawater evaporitic trend obtained from fluid inclusions (Figure 12F) supports the hypothesis of deep hydrothermal fluids mixing with evaporated seawater to deposit quartz and barite cements.

The carbonate mounds observed in the Barra Velha Formation are hundreds of meters high, as observed by seismic evidence (Buckley et al., 2015; Barnett et al., 2021; Zeller et al., 2022). Due to their high topographic expression, these mounds may have been directly in contact with seawater incursions for a long time during the deposition of the Ariri Formation, allowing seawater to infiltrate down through the fracture network and participate in the diagenesis. They are also likely to have been exposed when the lake water level was low, causing erosion, dissolution, and fracturing by collapse (Wright, 2022).

Where evaporites formed an early effective seal on top of carbonates, most likely where mounds are not present, uprising fluids passing through faults were impeded to flow to upper formations and flowed mostly under the evaporites, predominantly affecting the pre-Salt sequence. Preferential hydrothermal alteration just below the evaporite deposits has been described in the Brazilian pre-Salt carbonates and is evidence of the evaporites acting as a seal for uprising hydrothermal fluids where carbonate mounds are not present (e.g., Lima et al., 2020).

The late megaquartz found in fractures is commonly associated with barite and has been described in other pre-Salt areas as being extraformational, hydrothermal, and hosting high-temperature fluid inclusions (Lapponi et al., 2019; Lima et al., 2020). Late quartz cementation has been described as being associated with finger-like silicification bodies that migrate laterally from fault zones (Basso et al., 2023). In addition to quartz, barite, and saddle dolomite, we found a late-stage solid bitumen filling fracture porosity and vugs. Solid bitumen is commonly found in hydrothermally altered carbonates (e.g., Lima and De Ros, 2019; Lima et al., 2020; Ukar et al., 2020). Although we do not have an absolute age for the bitumen found in our samples, similar bitumen-rich fractures are commonly found in the related African Namibe Basin in Angola, where they have been dated as 86.2 ± 2.4 Ma based on the U-Pb geochronology of associated calcite cement

(Rochelle-Bates et al., 2021). This age is in accordance with our description of the solid bitumen being a late phase with respect to barite, quartz, and saddle dolomite mineralization found in the fault zone. These considerations suggest that the exotic mineralogy found in fractures and fault breccias is most readily explained by the presence of widespread hydrothermal alteration directly interacting with infiltrating evaporated seawater affecting the brittle structures within carbonate mounds at the sites of wells A and B.

The Influence of Magmatism

Hydrothermal activity is compatible with what is known of the timing and pattern of magmatism in the Santos Basin. The deposition of sediments in the pre-Salt succession in the Santos Basin is intercalated with igneous rocks from several episodes of magmatism. The main magmatic activity at the South Atlantic started with an early peak at ca. 135 Ma and lasted until ca. 114 Ma in the Aptian (Szatmari and Milani, 2016; Gordon et al., 2023). Evidence suggesting contemporaneous volcanism with the Barra Velha Formation is commonly found in the pre-Salt reservoirs (e.g., Moreira et al., 2005; Thomaz Filho et al., 2008; Fornero et al., 2019; Louback et al., 2023). Fornero et al. (2019) described an interval of 400 m of volcanic rocks and basaltic subaerial flows covered by evaporites in a well in the Santos Basin. In some locations, these mafic rocks were deposited, showing pahoehoe textures (Fornero et al., 2019) typically associated with subaerial volcanic eruptions, which is evidence of the surface being actively fed by dykes or volcanoes at the time of the Barra Velha Formation deposition. Subaqueous volcanism in the Santos Basin is also evidenced by the presence of volcanic rocks rich in volcanic glass, which are formed by rapid quenching of the lava in the lake water (Zucchetti et al., 2015). The active volcanism can alter the lake water composition (e.g., Mercedes-Martín et al., 2019) and allow hot magmatic fluids to affect the host rock and deposit minerals. Our results show fluid inclusion in barite and quartz veins within the Barra Velha Formation that have coeval presence of hydrocarbons and high-salinity brines, with T_h higher than present-day temperature, which is evidence of hydrothermal origin.

The helium isotopic composition in fluid inclusions in barite and quartz is ~2 Ra, showing a substantial input of volatiles from mantle origin. Crustal $^3He/^4He$ ratios are typically ~0.01 Ra due to the predominance of radioactive elements such as uranium and thorium in the crust that decay to ^4He, whereas mantle sources preserve a high $^3He/^4He$ ratio of ~8 Ra (and even higher in plume settings), due to the presence of primordial ^3He and limited radioactive decay to ^4He (Torgersen and Jenkins, 1982). The high $^3He/^4He$ ratio of ~2 Ra found in our samples is thus evidence of a direct contribution from mantle fluids into the hydrothermal system that interacted with the Barra Velha Formation, depositing the quartz and barite cements in the fracture network.

As our chemical analysis showed, besides the presence of exotic cations such as barium, we do not see evidence of a major magmatic ionic contribution, because fluid inclusion ionic composition is very close to the seawater evaporitic trend, suggesting that most of the direct magmatic input was in the form of volatiles (i.e., gases, probably with CO_2) and interacted with seawater. The $^3He/^4He$ ratio of our samples is lower than the expected ratio for a "pure" mantle source, which may suggest some mixing with radioactive helium by interaction with fluids from crustal sources. A similar conclusion was reached by Szatmari and Milani (2016), Lima et al. (2020), and Pestilho et al. (2022), who also interpret influence from magmatic events or direct magmatic input by mantellic sources on the diagenesis observed in the Barra Velha Formation.

The magmatic events affecting the Santos Basin during the Cretaceous and Paleogene must have had a direct influence on the depositional style and the diagenesis by input of magmatic volatiles, exotic elements and heat during deposition, and burial of the Barra Velha Formation. Magmatism in conjunction with brittle deformation, which served as pathways for fluids, probably allowed the creation of geothermal anomalies, hydrothermal vents, and lacustrine spring mounds and the input of exotic elements, including large amounts of early silica cements in the host rock. While the Aptian magmatism must have influenced the depositional system, younger magmatic events during the drift phase of the Santos Basin (e.g., Gordon et al., 2023) probably controlled hydrothermal diagenesis identified by this study, such as the 95-Ma saddle dolomite and barite mineralization.

The high amounts of CO_2 mixed with hydrocarbons in this oil field could also have been sourced by

the mantle in the form of volatiles. A high CO_2 content in aqueous fluids can increase fluid acidity, which favors dissolution of the calcitic host rock. Such a mechanism could explain the common occurrence of vuggy fractures, large pores, and caves in the Barra Velha Formation. Further CO_2 input at a later stage probably mixed with the hydrocarbon charge, explaining the high CO_2 content dissolved in the reservoir oil and in the gas cap of nearby reservoirs (e.g., Gamboa et al., 2019).

Implications of High Uranium Concentrations

The uranium concentrations in chalcedony cement found in well A (up to 2 ppm) are unusual because quartz is not a uranium-bearing mineral. High uranium concentration intervals have been reported in the Barra Velha Formation, where fractures and mounded carbonates are present (Melani, 2019). A common source for high uranium peaks in gamma-ray logs can be organic matter; however, there are occurrences in the Barra Velha Formation in which thorium and potassium contents do not follow uranium increments as expected in organic matter–rich shales, meaning that the source of uranium may be something else (e.g., Melani, 2019). These unusual uranium variations within the Barra Velha Formation are not well understood, but we can hypothesize how the uranium is incorporated in chalcedony cement by at least two mechanisms.

1. The uranium was sourced by the host rock. Highly reactive dissolving fluids partially dissolved the rock that has a significant uranium content for carbonates (up to 9 ppm). Small inclusions of host rock still preserved inside the chalcedony may source the uranium measured in LA-ICP-MS (e.g., Figure 4C, HRR).
2. The uranium was sourced by hydrothermal fluids. In this case, the uranium may be in microscopic mineral inclusions that can hold uranium and are associated with the chalcedony.

Hydrothermal paragenesis with aluminum phosphate-sulfate minerals, such as svanbergite, was found as 1- to 100-μm sized inclusions in cements within the Brazilian pre-Salt carbonates (Lima et al., 2020; Strugale et al., 2024). These minerals are known to be commonly associated with uranium deposits (e.g., Gaboreau et al., 2005) and thus reinforce the hypothesis of hydrothermal uranium origin.

Conceptual Fracture Model

Here, we discuss the sequence of diagenetic events affecting the fracture network, the fracture distribution, and the mechanisms to preserve open fracture porosity.

Timeline of Diagenetic Events

Our investigation allowed us to determine the sequence of diagenetic events affecting the fracture network (Figures 14, 15). The diagenetic components within the Barra Velha Formation can be composed of several types of dolomites (microcrystalline, rhombohedral, anhedral, lamellar, saddle, blocky), calcite (cryptocrystalline, rim cement, coarse crystalline), and silica (chalcedony, microcrystalline, and macrocrystalline) (De Carvalho and Fernandes, 2021; Carramal et al., 2022; Carvalho et al., 2022; Brito et al., 2024; Gomes et al., 2025). Only some of the known diagenetic phases could be observed filling brittle structures in our samples, namely rhombohedral and saddle dolomites, chalcedony, and macrocrystalline/megaquartz. However, we were able to observe extra cement/filling phases usually not present in the host rock, namely radiaxial-fibrous and euhedral calcite cements, barite cements, and solid bitumen.

The timeline of events (Figure 14) is constrained by U-Pb ages or by petrography where geochronological data are missing. Our event chart considers the uncertainties of the U-Pb geochronology method by the width of the bar in the chart. Although the sequence observed here is well constrained locally, it may vary in other areas. Because a substantial part of the diagenesis here is linked to hydrothermal alteration, it can be susceptible to changes in the underlying rocks and variation in magmatism occurrence.

The overall sequence of structural diagenesis affecting the Barra Velha Formation in the studied area is the following.

1. Host rock composed mostly of shrubstones and spherulitestones was deposited at least ca. 116–113 Ma within mounded carbonates rooted by faults. Fractures were formed very early, and dolomitization affected the calcite that infiltrated inside the fractures. Faults acted since the beginning, evidenced by cataclastic textures within small displacement faults.
2. Early brecciation and hydrothermal vents were active at least ca. 108 Ma at a maximum burial

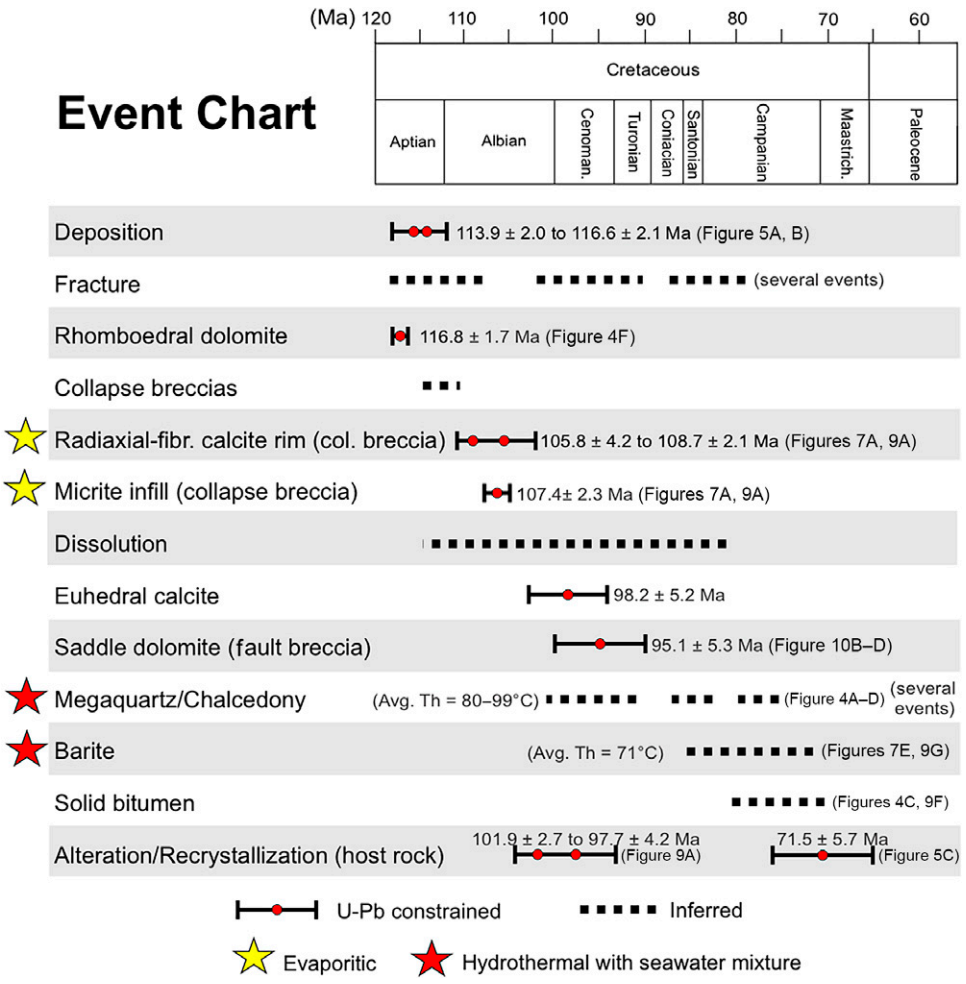

Figure 14. Chronology of diagenetic events in brittle structures. Event ages are constrained by U-Pb geochronology. We used petrography to infer relative age where geochronology was not available. Red circles: U-Pb estimated age. Black bars: U-Pb age uncertainty. Avg.Th: average homogenization temperature from fluid inclusions; Cenoman. = Cenomanian; col. = collapse; Fibr. = fibrous; Maastrich. = Maastrichtian.

depth of ~400 to 600 m. Large cavities in host rock collapsed. Radiaxial-fibrous calcite rims formed around collapse breccia clasts. Infiltration of microcrystalline material followed the brecciation. These collapsed cavities were probably formed by overpressurized and corrosive fluids, although meteoric dissolution is also possible. Fluids with evaporitic signature and supersaturated in calcite precipitated radiaxial-fibrous calcite rims. Evaporitic lake waters and seawater incursions infiltrated downward into the mounds through fractures. Wide veins formed with fluid escape structures.

3. Dissolution of host rock took place, probably aided by mantle-derived volatiles, including He and CO_2, creating vuggy pores and caves around faults and within the fracture network. Early vuggy pores were covered by euhedral calcite at ca. 98 Ma.
4. Oblique-normal faults and associated fault breccia were mineralized at least 95 Ma. Ascending hydrothermal fluids mineralized the fault zone, mostly with saddle dolomite.
5. With continuing dissolution, fractures were enlarged and formed a network of vuggy fractures. Large cavities formed quartz or barite geodes when mineralized. Chalcedony, quartz, and barite-filling fractures were deposited by hydrothermal fluids that interacted with basement, magmatic sources, and mixture with previously infiltrated seawater.
6. Solid bitumen filled open pores still connected to the overall fault and fracture network, representing the last phase of filling.

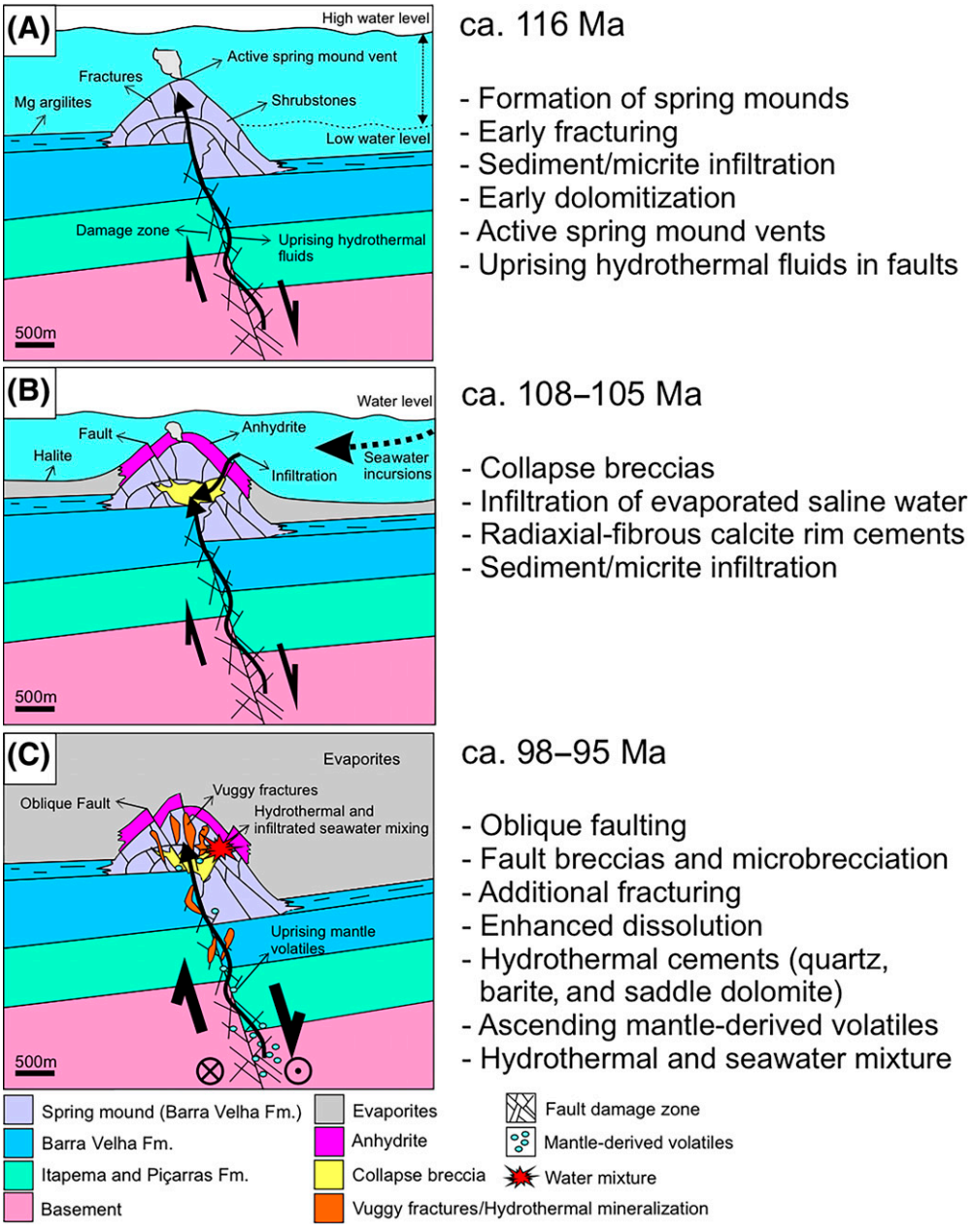

Figure 15. Stages of mound development, diagenetic and hydrothermal alterations, and brittle deformation. (A) Circa 116 Ma: formation of carbonate mounds, early fractures, microcrystalline infill and dolomitization. (B) Circa 105–108 Ma: collapse brecciation cemented by radiaxial-fibrous calcite with evaporitic geochemical signature. (C) Circa 98–95 Ma: oblique faulting, dissolution, and hydrothermal cementation mostly by quartz and barite. Solid bitumen migration and calcite recrystallization are younger events. Horizontal and vertical scales of features are purposely exaggerated for clarity. Fm. = Formation.

Preservation of Open Fractures

Fracture porosity is mostly seen preserved in fractures mineralized with quartz or barite. These fractures typically have irregular pitted fracture walls, suggesting that the fluids passing through caused dissolution of the calcitic host rock (Figures 3; 9C, G). The fluids that caused cementation in fractures are likely of hydrothermal origin, as indicated by elevated T_h values of fluid inclusions hosted in quartz and barite. The latter could be sourced from fluids that originated from outside of the Barra Velha Formation. Thus, fractures formed (either during regional burial or associated with faults) and were differentially widened by corrosive fluids, but they subsequently were partly filled with hydrothermal minerals. Preservation of porosity depends on how wide the fractures

are during dissolution and on the extent of later mineral infill.

The correlation of fault zone proximity and secondary porosity preservation has been identified in some pre-Salt areas. There is evidence of the importance of fault damage zones creating fracture porosity that may be further increased by dissolution, causing the formation of vuggy fractures (e.g., Figure 3B, D) and caves (De Jesus et al., 2016; Baqués et al., 2020; Fernández-Ibáñez et al., 2022a). Wennberg et al. (2021) described intervals of damage zones next to faults with high average fracture intensity of 14 fractures per meter based on image logs. These regions can have high porosity (>20%) and high permeability (>1 d) and are thought to be among the causes of excess permeability identified by well tests (e.g., Fernández-Ibáñez et al., 2022b). However, fractures with regular walls are usually pervasively cemented, most commonly with quartz (Figure 10B, QV). This suggests the importance of faults creating secondary porosity in the reservoir, and in areas where widespread dissolution occurred, porosity remained partially preserved in some proportion.

A curious feature commonly observed in vugs and fractures mineralized with quartz and barite is size-dependent mineralization. When fractures can be seen connected with vugs forming a network of

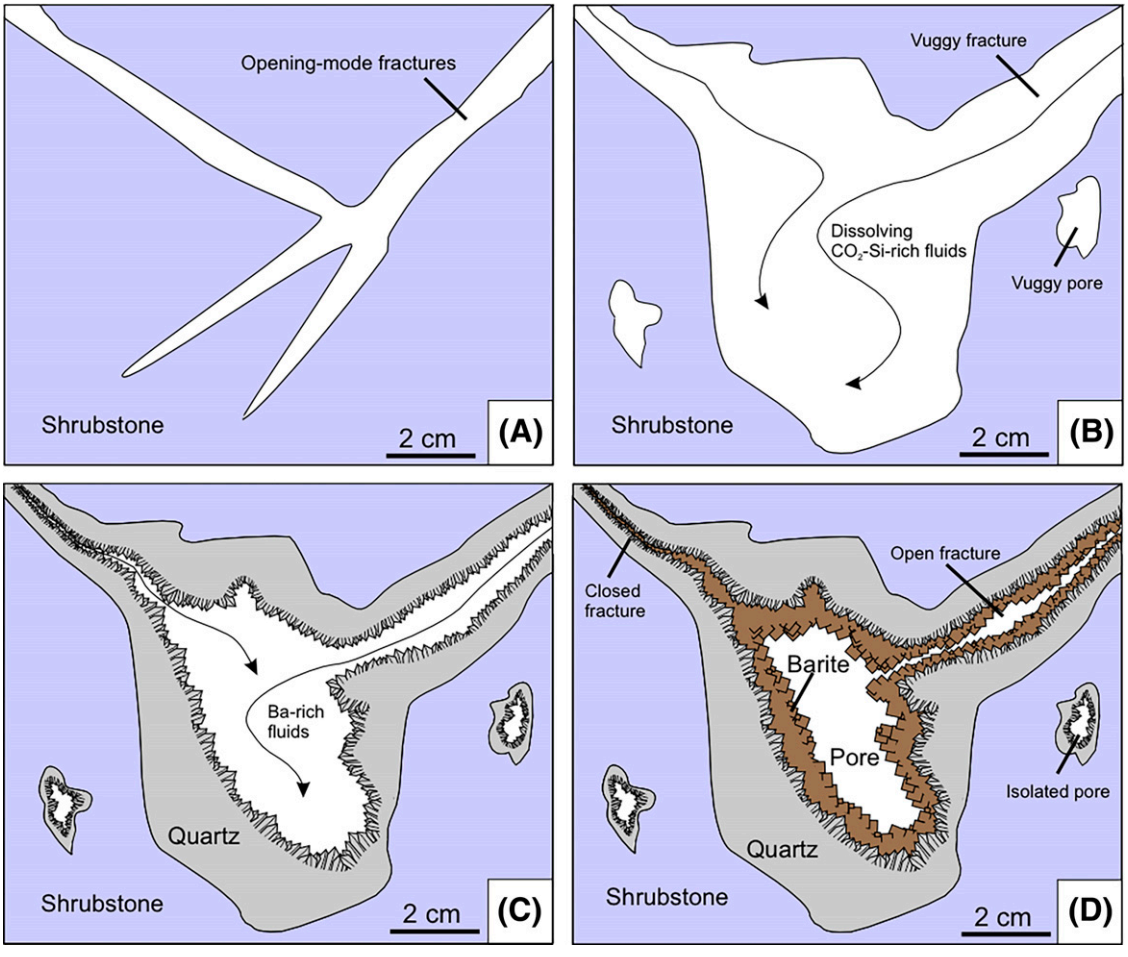

Figure 16. Mechanism to form and preserve mineralized vuggy fractures and vuggy pores. (A) Deformed host rock with opening-mode fractures showing straight walls. (B) Vuggy fracture enlarged by dissolving fluids rich in silica and mantle volatiles (CO_2 included) that promoted host rock dissolution. (C) Quartz covers vugs and fracture walls; narrow fractures are filled first, and large fractures are still open, leaving fluid pathways to Ba-rich fluids. (D) Barite covers the geode and vuggy fracture; remaining porosity is only preserved in large cavities forming geodes and the large vuggy fractures coated by euhedral cements, whereas narrow fractures are pervasively cemented, preventing new incoming fluid flow. Vuggy pores that became isolated from the pore network during quartz cementation do not show barite cementation.

fractures, narrow width fractures are pervasively cemented, but vuggy fractures or large cavities are still preserved, usually partially filled by euhedral quartz or barite in the form of a geode (e.g., Figure 7E).

A possible mechanism that can explain this preferential preservation of vuggy fracture porosity relative to quartz is the tendency for quartz to seal narrow fractures rapidly (Laubach, 2003; Lander and Laubach, 2015). This process has been proposed to explain porous, vuggy fault cores in sandstone (Laubach et al., 2014). However, where fluid transport governs quartz accumulation, wide conductive fractures may preferentially fill with quartz (Williams et al., 2015; Williams and Fagereng, 2022).

During the process of cementation, fractures and vugs were linked with one another and in contact with the same cementing fluid. However, as cementation took place, smaller parts of the network were closed first, with the crystal growth leaving only the larger pores preserved with partial fill. Notably large geodes (1–2 cm) with pristine quartz and barite crystals inside could only be preserved if these pores were isolated from the rest of the network because no other cement phase covered these euhedral crystals after they formed (Figure 16). Although geodes may have been linked to fractures and high-permeability pathways, the size-dependent fill that mainly closes small width fractures tends to isolate geode cavities. Once geodes are isolated from the rest of the fracture network, their contribution to permeability is likely zero, although their storage potential is mostly preserved. Later oil migration may have helped in the preservation of pristine crystals within geodes because the oil would prevent the deposition of minerals from aqueous solutions.

Based on these observations and inferences, we interpret that most of the preserved secondary porosity in fractures must have been interconnected with vuggy pores and was created by dissolving fluids sourced by the underlying faults. These fluids used the established damage zone around faults to flow through and dissolve fractures, creating in some parts vugs or even caves (e.g., De Jesus et al., 2016). When cementation took place, small fracture widths and pores filled first and clogged pathways to large cavities, creating pristine geodes and trapped porosity. Where large cavities are still connected, pathways are likely large enough to resist cementation ($\sim$1 cm or more).

CONCLUSIONS

In the Barra Velha Formation, our study of cores from two wells constrains the Aptian depositional age of the formation and documents the deformation of host rock by several phases of brecciation, faulting, and fracturing, which still preserve porosity.

Using U-Pb dating, we show that the Barra Velha Formation is at least approximately 116 m.y. old and that recrystallization affected some of the host rock components, yielding younger recrystallization ages (Albian and Maastrichtian) in some parts.

A shallow (400–600 m depth or less) collapse brecciation event affected the Barra Velha Formation at ca. 108 Ma. Isotopic geochemistry shows that the composition of radiaxial-fibrous calcite rims cementing breccias is evaporitic, suggesting that they were cemented by fluids with composition close to the evaporitic lake waters.

We provide the first description of wide veins mineralized with calcite and quartz and bearing crack-seal texture, internal brecciation, and fluid escape structures, which are indicative of hydrothermal vents or hot springs. Spring mounds or pinnacles observed in seismic and dendritic calcite growing in vuggy pores are additional evidence of vent-fed springs affecting depositional system and diagenesis.

Hydrothermal mineralization, including barite, saddle dolomite, quartz-filled breccias, veins, and vugs, are evidence of uprising hydrothermal fluids, rich in mantle volatiles, fed by the faults that interacted with infiltrated seawater and possibly basement. Fault mineralization occurred ca. 95 Ma, with saddle dolomite associated with fault breccias.

We describe a timeline of diagenetic events affecting the fracture network that is anchored by U-Pb dates. The fracture network experienced several episodes of cementation, probably linked to fluids ascending along a fault zone. Open porosity in fractures is preserved where neighboring narrow pathways to vuggy pores are clogged by cement or where dissolution was intense enough to create vuggy pores >1 cm or caverns that were not pervasively filled by barite or quartz cement. Solid bitumen is observed filling remaining open vuggy pores and fractures.

APPENDIX

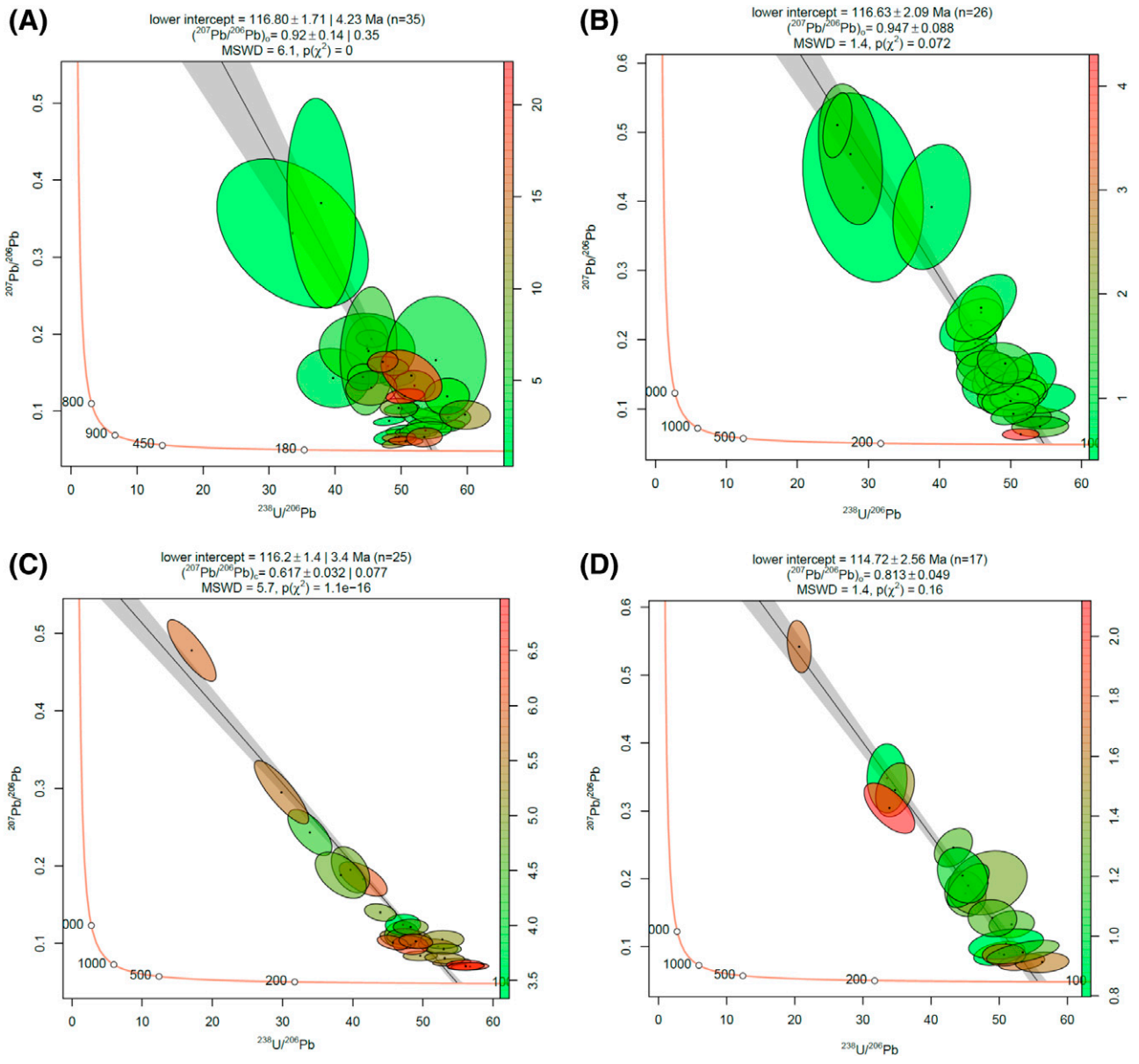

Figure 17. Tera-Wasserburg plots of the features dated with U-Pb. (A) Dolomite (substitution). (B) Spherulite 1 rim (host rock). (C) Shrub (host rock). (D) Spherulite 2 center (host rock). (E) Spherulite 2 rim (host rock). (F) Radiaxial-fibrous calcite rim (collapse breccia). (G) Radiaxial-fibrous calcite rim (collapse breccia). (H) Infill (collapse breccia). (I) Radiaxial-fibrous calcite rim (collapse breccia). (J) Altered host rock. (K) Euhedral calcite. (L) Altered host rock. (M) Saddle dolomite (fault breccia). (N) Shrub (recrystallized host rock). MSWD = mean squared weighted deviation.

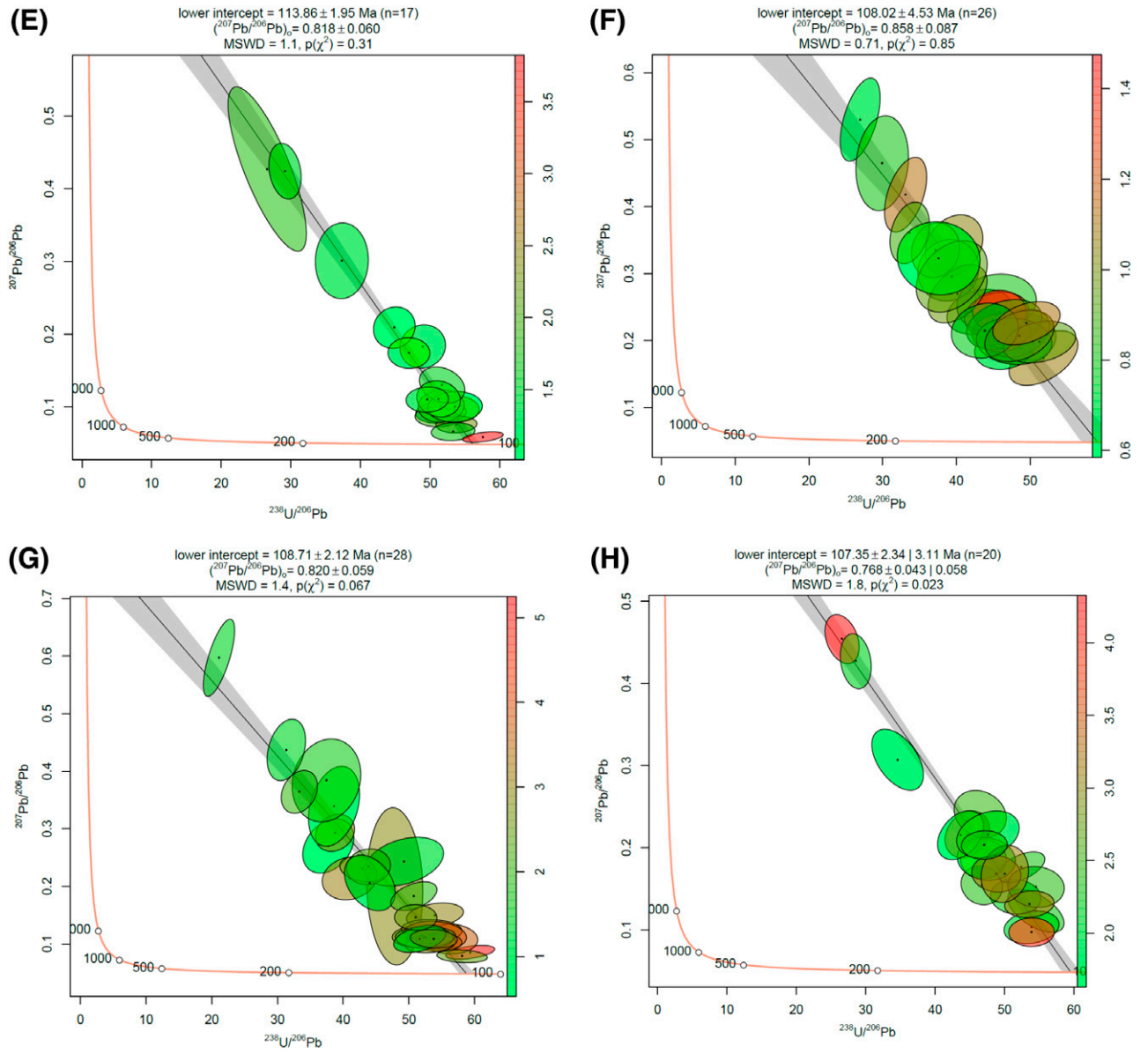

Figure 17. Continued

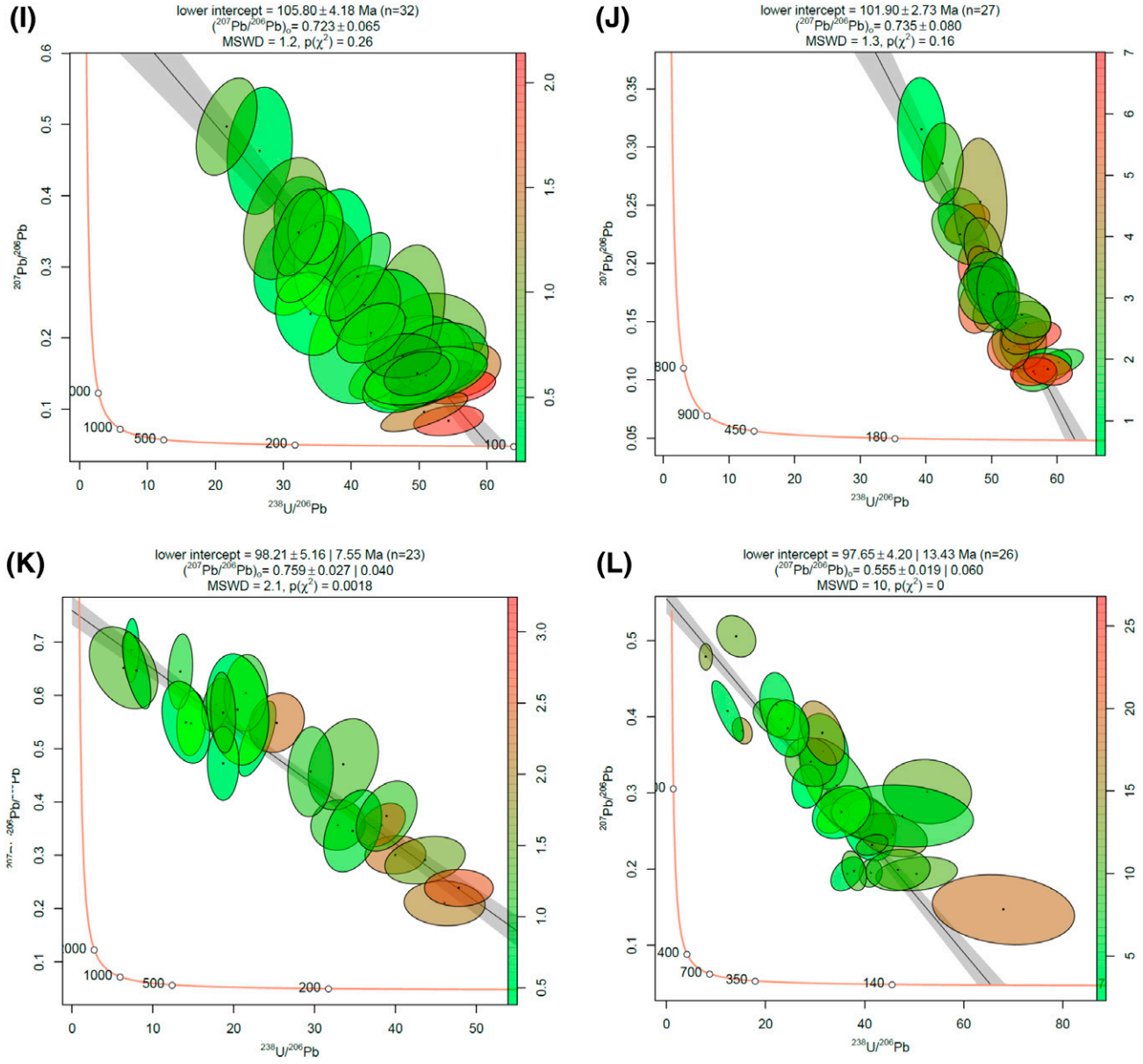

Figure 17. Continued

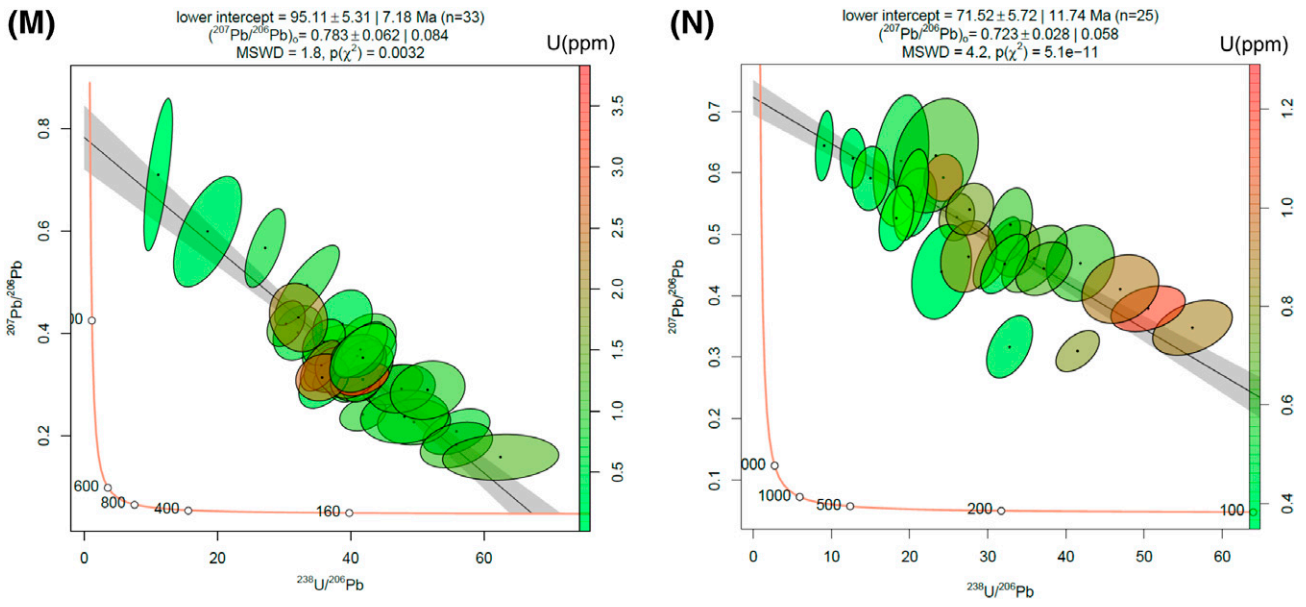

Figure 17. Continued

REFERENCES CITED

Adriano, M. S., J. P. Figueiredo, P. H. G. R. Coelho, and L. Borghi, 2022, Tectonic and stratigraphic evolution of the Santos Basin rift phase: New insights from seismic interpretation on Tupi oil field area: Journal of South American Earth Sciences, v. 116, 103842, 11 p., doi:10.1016/j.jsames.2022.103842.

Alvarenga, R. S., D. Iacopini, J. Kuchle, C. M. S. Scherer, and K. Goldberg, 2016, Seismic characteristics and distribution of hydrothermal vent complexes in the Cretaceous offshore rift section of the Campos Basin, offshore Brazil: Marine and Petroleum Geology, v. 74, p. 12–25, doi:10.1016/j.marpetgeo.2016.03.030.

Arai, M., A. T. Hashimoto, and N. Uesugui, 1989, Significado cronoestratigrafico da associacao microfloristica do Cretaceo Inferior do Brasil: Boletim de Geociencias da Petrobras, v. 3, p. 87–103.

Arienti, L. M., R. S. Souza, S. Viana, M. A. Cuglieri, R. P. Silva, S. Tonietto, L. De Paula, and J. A. Gil, 2018, Facies association, depositional systems, and paleophysiografic models of the Barra Velha Formation, pre-salt sequence–Santos Basin, Brazil (abs.): AAPG Annual Convention and Exhibition, Salt Lake City, Utah, May 20–23, 2018, accessed June 7, 2023, https://www.searchanddiscovery.com/abstracts/html/2018/ace2018/abstracts/2843310.html.

Aubert, I., H. Bitault, P. Léonide, F. Fournier, N. Godeau, J. Lamarche, P. Deschamp, R. S. M. Corrêa, and L. Marié, 2023, Effect of normal fault activity on carbonate reservoir diagenetic evolution (Urgonian facies, SE France): Marine and Petroleum Geology, v. 158, 106546, 19 p., doi:10.1016/j.marpetgeo.2023.106546.

Azerêdo, A. C., L. V. Duarte, and A. P. Silva, 2021, The challenging carbonates from the Pre-Salt reservoirs offshore Brazil: Facies, palaeoenvironment and diagenesis: Journal of South American Earth Sciences, v. 108, 103202, 23 p., doi:10.1016/j.jsames.2021.103202.

Balsamo, F., L. Clemenzi, F. Storti, J. Solum, and C. Taberner, 2019, Tectonic control on vein attributes and deformation intensity in fault damage zones affecting Natih platform carbonates, Jabal Qusaybah, north Oman: Journal of Structural Geology, v. 122, p. 38–57, doi:10.1016/j.jsg.2019.02.009.

Banks, D. A., G. Giuliani, B. W. Yardley, and A. Cheilletz, 2000, Emerald mineralisation in Colombia: Fluid chemistry and the role of brine mixing: Mineralium Deposita, v. 35, no. 8, p. 699–713, doi:10.1007/s001260050273.

Baqués, V., E. Ukar, S. E. Laubach, S. R. Forstner, and A. Fall, 2020, Fracture, dissolution, and cementation events in Ordovician carbonate reservoirs, Tarim Basin, NW China: Geofluids, v. 2020, 9037429, 28 p., doi:10.1155/2020/9037429.

Barnett, A. J., M. Obermaier, J. Amthor, M. Sharafodin, M. Bolton, D. Clarke, and R. Camara, 2021, Origin and significance of thick carbonate grainstone packages in nonmarine successions: A case study from the Barra Velha Formation, Santos Basin, Brazil, *in* M. R. Mello, P. O. Yilmaz, and B. J. Katz, eds., The supergiant Lower Cretaceous pre-salt petroleum systems of the Santos Basin, Brazil: AAPG Memoir 124, p. 155–174.

Basso, M., G. F. Chinelatto, A. M. P. Belila, L. C. Mendes, J. P. P. Souza, D. Stefanelli, A. C. Vidal, and J. F. Bueno, 2023, Characterization of silicification and dissolution zones by integrating borehole image logs and core samples: A case study of a well from the Brazilian pre-salt: Petroleum Geoscience, v. 29, no. 3, 21 p., doi:10.1144/petgeo2022-044.

Bastesen, E., and A. Braathen, 2010, Extensional faults in fine grained carbonates–Analysis of fault core lithology and thickness–displacement relationships: Journal of Structural Geology, v. 32, no. 11, p. 1609–1628, doi:10.1016/j.jsg.2010.09.008.

Beaudoin, N. E., O. Lacombe, G. Hoareau, and J. Callot, 2022, How the geochemistry of syn-kinematic calcite cement depicts past fluid flow and assists structural interpretations: A review of concepts and applications in orogenic forelands: Geological Magazine, v. 159, no. 11–12, p. 2157–2190, doi:https://doi.org/10.1017/S0016756822001327.

Bisdom, K., G. Bertotti, and H. M. Nick, 2016, The impact of in-situ stress and outcrop-based fracture geometry on hydraulic aperture and upscaled permeability in fractured reservoirs: Tectonophysics, v. 690, p. 63–75, doi:10.1016/j.tecto.2016.04.006.

Brito, J. P. S., R. V. Santos, G. O. Gonçalves, P. F. Barbosa, C. E. S. Cruz, C. A. Ushirobira, V. S. Souza, F. Richter, and C. J. Abreu, 2024, U-Pb dating of Barra Velha carbonates reveals the influence of Santos Basin sedimentary and tectonothermal history on pre-salt carbonate ages: Marine and Petroleum Geology, v. 168, 107035, 20 p., doi:10.1016/j.marpetgeo.2024.107035.

Brogi, A., E. Capezzuoli, S. Kele, M. O. Baykara, and C. C. Shen, 2017, Key travertine tectofacies for neotectonics and palaeoseismicity reconstruction: Effects of hydrothermal overpressured fluid injection: Journal of the Geological Society, v. 174, no. 4, p. 679–699, doi:10.1144/jgs2016-124.

Buckley, J. P., D. Bosence, and C. Elders, 2015, Tectonic setting and stratigraphic architecture of an Early Cretaceous lacustrine carbonate platform, Sugar Loaf High, Santos Basin, Brazil, *in* D. W. J. Bosence, K. A. Gibbons, D. P. Le Heron, W. A. Morgan, T. Pritchard, and B. A. Vining, eds., Microbial carbonates in space and time: Implications for global exploration and production: Geological Society, London, Special Publications 2015, v. 418, p. 175–191, doi:10.1144/SP418.13.

Caine, J. S., J. P. Evans, and C. B. Forster, 1996, Fault zone architecture and permeability structure: Geology, v. 24, no. 11, p. 1025–1028, doi:10.1130/0091-7613(1996)024<1025:FZAAPS>2.3.CO;2.

Campos Neto, O. P. d. A., W. S. Lima, and F. E. Gomes Cruz, 2007, Bacia de Sergipe-Alagoas: Boletim de Geociencias da Petrobras, v. 15, p. 405–415.

Carlotto, M. A., R. C. B. Silva, A. A. Yamato, W. L. Trindade, J. L. P. Moreira, R. A. R. Fernandes, O. J. S. Ribeiro, et al., 2017, Libra: A newborn giant in the Brazilian Pre-salt Province, *in* R. K. Merrill and C. A. Sternbach, eds., Giant fields of the decade 2000–2010: AAPG Memoir 113, p. 165–176.

Carminatti, M., J. Dias, and B. Wolff, 2009, From turbidites to carbonates: Breaking paradigms in deep waters: 2009 Offshore Technology Conference, Houston, Texas, May 4–7, 2009, OTC-20124-MS, 7 p., https://doi.org/10.4043/20124-MS.

Carramal, N. G., D. M. Oliveira, A. S. Cacela, M. A. Cuglieri, N. P. Rocha, S. M. Viana, S. L. V. Toledo, S. Pedrinha, and L. F. De Ros, 2022, Paleoenvironmental insights from the deposition and diagenesis of Aptian pre-salt magnesium silicates from the Lula Field, Santos Basin, Brazil: Journal of Sedimentary Research, v. 92, no. 1, p. 12–31, doi:10.2110/jsr.2020.139.

Carvalho, A. M. A., H. Youri, G. D. S. J. Olinto, C. N. Goulart, and C. Nathalie, 2022, Facies and diagenesis distribution in an Aptian pre-salt carbonate reservoir of the Santos Basin, offshore Brazil: A comprehensive quantitative approach: Marine and Petroleum Geology, v. 141, 105708, 25 p., doi:10.1016/j.marpetgeo.2022.105708.

Chaboureau, A. C., F. Guillocheau, C. Robin, S. Rohais, M. Moulin, and D. Aslanian, 2013, Paleogeographic evolution of the central segment of the South Atlantic during Early Cretaceous times: Paleotopographic and geodynamic implications: Tectonophysics, v. 604, p. 191–223, doi:10.1016/j.tecto.2012.08.025.

Chester, F. M., and J. M. Logan, 1986, Implications for mechanical properties of brittle faults from observations of the Punchbowl fault zone, California: Pure and Applied Geophysics, v. 124, no. 1–2, p. 79–106, doi:10.1007/BF00875720.

Chew, D. M., J. A. Petrus, and B. S. Kamber, 2014, U–Pb LA–ICPMS dating using accessory mineral standards with variable common Pb: Chemical Geology, v. 363, p. 185–199, doi:10.1016/j.chemgeo.2013.11.006.

Corrêa, R., C. Pereira, F. Cruz, S. Lisboa, M. Junior, V. Souza, C. Rocha, F. Araujo, and B. M. De Carvalho, 2019. Integrated seismic-log-core-test fracture characterization and modelling, Barra Velha Formation, Pre-salt of Santos Basin: AAPG Search and Discovery article 42425, accessed June 7, 2023, https://www.searchanddiscovery.com/pdfz/documents/2019/42425correa/ndx_correa.pdf.html.

Corrêa, R. S. M., E. Ukar, S. E. Laubach, I. Aubert, J. Lamarche, Q. Wang, D. F. Stockli, L. D. Stockli, and T. E. Larson, 2022, Episodic reactivation of carbonate fault zones with implications for permeability–An example from Provence, southeast France: Marine and Petroleum Geology, v. 145, 105905, 21 p., doi:10.1016/j.marpetgeo.2022.105905.

Davies, G. R., and L. B. Smith, 2006, Structurally controlled hydrothermal dolomite reservoir facies: An overview: AAPG Bulletin, v. 90, no. 11, p. 1641–1690, doi:10.1306/05220605164.

de Carvalho, M. D., and F. L. Fernandes, 2021, Pre-salt depositional system: Sedimentology, diagenesis, and reservoir quality of the Barra Velha Formation, as a result of the Santos Basin tectono-stratigraphic development, *in* M. R. Mello, P. O. Yilmaz, and B. J. Katz, eds., The supergiant Lower Cretaceous pre-salt petroleum systems of the Santos Basin, Brazil: AAPG Memoir 124, p. 121–154.

Dehler, N. M., L. P. Magnavita, L. C. Gomes, C. A. Rigoti, J. A. B. de Oliveira, M. V. Sant'Anna, and F. G. D. da Costa, 2016, The 'Helmut' geophysical anomaly: A regional left-lateral transtensional shear zone system connecting Santos and Campos basins, southeastern Brazil: Marine and Petroleum Geology, v. 72, p. 412–422, doi:10.1016/j.marpetgeo.2016.01.012.

de Jesus, C. M., A. L. M. Compan, J. R. P. Coêlho, A. E. de Sá Silveira, and M. Blauth, 2019, Evaluation of karst porosity morphological properties through borehole image logs–Correlation with dynamic reservoir properties from a presalt oil field: Offshore Technology Conference Brasil, Rio de Janeiro, Brazil, October 29–31, 2019, OTC-29722-MS, 16 p., doi:10.4043/29722-MS.

de Jesus, C. M., A. L. Martins Compan, and R. Surmas, 2016, Permeability estimation using ultrasonic borehole image logs in dual-porosity carbonate reservoirs: Petrophysics, v. 57, no. 6, p. 620–637.

Dekov, V. M., N. M. Egueh, G. D. Kamenov, G. Bayon, S. V. Lalonde, M. Schmidt, V. Liebetrau, et al., 2014, Hydrothermal carbonate chimneys from a continental rift (Afar Rift): Mineralogy, geochemistry, and mode of formation: Chemical Geology, v. 387, p. 87–100, doi:10.1016/j.chemgeo.2014.08.019.

Della Porta, G., 2015, Carbonate build-ups in lacustrine, hydrothermal and fluvial settings: comparing depositional geometry, fabric types and geochemical signature, *in* D. W. J. Bosence, K. A. Gibbons, D. P. Le Heron, W. A. Morgan, T. Pritchard, and B. A. Vining, eds., Microbial carbonates in space and time: Implications for global exploration and production: Geological Society, London, Special Publications 2015, v. 418, p. 17–68.

Della Porta, G., E. Capezzuoli, and A. De Bernardo, 2017, Facies character and depositional architecture of hydrothermal travertine slope aprons (Pleistocene, Acquasanta Terme, Central Italy): Marine and Petroleum Geology, v. 87, p. 171–187, doi:10.1016/j.marpetgeo.2017.03.014.

DeMott, L. M., and C. A. Scholz, 2020, Lacustrine carbonate tufa facies of Winnemucca Dry Lake Basin, Nevada, USA: Journal of Sedimentary Research, v. 90, no. 12, p. 1804–1828, doi:10.2110/jsr.2020.004.

DeMott, L. M., C. A. Scholz, and M. O. Awaleh, 2021, Lacustrine carbonate towers of Lake Abhe, Djibouti: Interplay of hydrologic and microbial processes: Sedimentary Geology, v. 424, 105983, 13 p., doi:10.1016/j.sedgeo.2021.105983.

Denny, A. C., A. Fall, I. J. Orland, J. W. Valley, P. Eichhubl, and S. E. Laubach, 2020, A history of pore water oxygen isotope evolution in the Cretaceous Travis Peak Formation in east Texas: GSA Bulletin, v. 132, no. 7–8, p. 1626–1638, doi:10.1130/B35291.1.

de Paula Faria, D. L., A. T. dos Reis, and O. G. de Souza, Jr., 2017, Three-dimensional stratigraphic-sedimentological forward modeling of an Aptian carbonate reservoir deposited during the sag stage in the Santos Basin, Brazil: Marine and Petroleum Geology, v. 88, p. 676–695, doi:10.1016/j.marpetgeo.2017.09.013.

de Ros, L. F., 2021, Syngenetic, diagenetic and hydrothermal processes in the pre-Salt sag section of Santos and Campos Basins: Second European Association of Geoscientists and Engineers Conference on Pre-Salt Reservoir, online, September 8–10, 2021, 5 p., doi:10.3997/2214-4609.202183007.

Fall, A., and R. J. Bodnar, 2018, How precisely can the temperature of a fluid event be constrained using fluid inclusions?: Economic Geology, v. 113, no. 8, p. 1817–1843, doi:10.5382/econgeo.2018.4614.

Farias, F., P. Szatmari, A. Bahniuk, and A. B. Franca, 2019, Evaporitic carbonates in the pre-salt of Santos Basin–Genesis and tectonic implications: Marine and Petroleum Geology, v. 105, p. 251–272, doi:10.1016/j.marpetgeo.2019.04.020.

Fernández-Ibáñez, F., G. D. Jones, J. G. Mimoun, M. G. Bowen, J. A. Simo, V. Marcon, and W. L. Esch, 2022a, Excess permeability in the Brazil pre-Salt: Nonmatrix types, concepts, diagnostic indicators, and reservoir implications: AAPG Bulletin, v. 106, no. 4, p. 701–738, doi:10.1306/10042120171.

Fernández-Ibáñez, F., A. Nolting, C. I. Breithaupt, B. Darby, J. Mimoun, and S. Henares, 2022b, The properties of faults in the Brazil pre-salt: A reservoir characterization perspective: Marine and Petroleum Geology, v. 146, 105955, 12 p., doi:10.1016/j.marpetgeo.2022.105955.

Fetter, M., 2009, The role of basement tectonic reactivation on the structural evolution of Campos Basin, offshore Brazil: Evidence from 3D seismic analysis and section restoration: Marine and Petroleum Geology, v. 26, no. 6, p. 873–886, doi:10.1016/j.marpetgeo.2008.06.005.

Fornero, S. A., G. M. Marins, J. T. Lobo, A. F. M. Freire, and E. F. de Lima, 2019, Characterization of subaerial volcanic facies using acoustic image logs: Lithofacies and logfacies of a lava-flow deposit in the Brazilian pre-salt, deepwater of Santos Basin: Marine and Petroleum Geology, v. 99, p. 156–174, doi:10.1016/j.marpetgeo.2018.09.029.

Fragoso, D. G. C., A. H. de Melo, L. A. Gonçalves, R. B. Bunevich, J. D. A. M. Araujo, T. C. da Costa, C. A. Pedrosa, and C. M. D. S. Scherer, 2023, High-resolution sequence stratigraphy applied to reservoir characterization of the Brazilian Cretaceous pre-salt section, Campos Basin: Guidelines for geological modeling and reservoir management: Marine and Petroleum Geology, v. 151, 106203, 25 p., doi:10.1016/j.marpetgeo.2023.106203.

França, R. L., A. C. Del Rey, C. V. Tagliari, J. R. Brandao, and P. d. R. Fontanelli, 2007, Bacia do Espirito Santo: Boletim de Geociencias da Petrobras, v. 15, p. 501–509.

Friedman, G. M., 1959, Identification of carbonate minerals by staining methods: Journal of Sedimentary Research, v. 29, no. 1, p. 87–97, doi:10.1306/74D70894-2B21-11D7-8648000102C1865D.

Gaboreau, S., D. Beaufort, P. Vieillard, P. Patrier, and P. Bruneton, 2005, Aluminum phosphate–sulfate minerals associated with Proterozoic unconformity-type uranium deposits in the East Alligator River Uranium Field, Northern Territories, Australia: The Canadian Mineralogist, v. 43, no. 2, p. 813–827, doi:10.2113/gscanmin.43.2.813.

Gamboa, L., A. Ferraz, R. Baptista, and E. V. S. Neto, 2019, Geotectonic controls on CO_2 formation and distribution processes in the Brazilian pre-salt basins: Geosciences, v. 9, no. 6, 252, 14 p., doi:10.3390/geosciences9060252.

Garland, J., J. Neilson, S. E. Laubach, and K. J. Whidden, 2012, Advances in carbonate exploration and reservoir analysis, *in* J. Garland, J. Neilson, S. E. Laubach, and K. J. Whidden, eds., Advances in carbonate exploration and

reservoir analysis: Geological Society, London, Special Publications 2012, v. 370, p. 1–15, doi:10.1144/SP370.15.
Goldstein, R. H., 2001, Fluid inclusions in sedimentary and diagenetic systems: Lithos, v. 55, no. 1–4, p. 159–193, doi:10.1016/S0024-4937(00)00044-X.
Goldstein, R. H., and T. J. Reynolds, 1994, Fluid inclusion microthermometry, *in* R. H. Goldstein and T. J. Reynolds, eds., Systematics of fluid inclusions in diagenetic minerals: Tulsa, Oklahoma, SEPM Short Course Notes 31, p. 87–121.
Gomes, J. P., R. B. Bunevich, L. R. Tedeschi, M. E. Tucker, and F. F. Whitaker, 2020, Facies classification and patterns of lacustrine carbonate deposition of the Barra Velha Formation, Santos Basin, Brazilian Pre-salt: Marine and Petroleum Geology, v. 113, 104176, 21 p., doi:10.1016/j.marpetgeo.2019.104176.
Gomes, J. P. B., R. B. Bunevich, A. C. L. Sartorato, L. R. Tedeschi, S. N. Tonietto, M. E. Tucker, and F. Whitaker, 2025, Early diagenetic evolution based on petrography and stable isotope analysis in the Barra Velha Formation of the Brazilian Pre-salt: The Depositional Record, v. 11, no. 1, p. 70–94, doi:10.1002/dep2.288.
Gontijo, G. A., P. d. S. Milhomem, J. M. Caixeta, I. S. S. Dupuy, and P. E. L. Menezes, 2007, Bacia de Almada: Boletim de Geociencias da Petrobras, v. 15, p. 463–473.
Gordon, A. C., W. U. Mohriak, N. Stanton, and A. C. Santos, 2023, Magmatic cycles in Santos Basin (SE Brazil): Tectonic control in the temporal-spatial distribution and geophysical signature: Journal of South American Earth Sciences, v. 121, 104111, 32 p., doi:10.1016/j.jsames.2022.104111.
Griffith, E. M., and A. Paytan, 2012, Barite in the ocean–Occurrence, geochemistry and palaeoceanographic applications: Sedimentology, v. 59, no. 6, p. 1817–1835, doi:10.1111/j.1365-3091.2012.01327.x.
Guo, X., and H. S. Chafetz, 2014, Trends in $\delta^{18}O$ and $\delta^{13}C$ values in lacustrine tufa mounds: Palaeohydrology of Searles Lake, California: Sedimentology, v. 61, no. 1, p. 221–237, doi:10.1111/sed.12085.
Hancock, P. L., 1985, Brittle microtectonics: Principles and practice: Journal of Structural Geology, v. 7, no. 3–4, p. 437–457, doi:10.1016/0191-8141(85)90048-3.
Hanor, J. S., 2000, Barite–celestine geochemistry and environments of formation: Reviews in Mineralogy and Geochemistry, v. 40, no. 1, p. 193–275, doi:10.2138/rmg.2000.40.4.
Heilbron, M., C. D. M. Valeriano, C. C. G. Tassinari, J. Almeida, M. Tupinamba, O. Siga, Jr., and R. Trouw, 2008, Correlation of Neoproterozoic terranes between the Ribeira Belt, SE Brazil and its African counterpart: Comparative tectonic evolution and open questions, *in* R. J. Pankhurst, R. A. J. Trouw, B. B. de Brito Neves, and M. J. de Wit, eds., West Gondwana: Pre-correlations across the South Atlantic region: Geological Society, London, Special Publications 2008, v. 294, p. 211–237.
Herlinger, R., Jr, E. E. Zambonato, and L. F. De Ros, 2017, Influence of diagenesis on the quality of Lower Cretaceous pre-salt lacustrine carbonate reservoirs from northern Campos Basin, offshore Brazil: Journal of Sedimentary Research, v. 87, no. 12, p. 1285–1313, doi:10.2110/jsr.2017.70.
Hoareau, G., N. Crognier, B. Lacroix, C. Aubourg, N. M. Roberts, N. Niemi, M. Branellec, N. Beaudoin, and I. S. Ruiz, 2021, Combination of Δ47 and U-Pb dating in tectonic calcite veins unravel the last pulses related to the Pyrenean Shortening (Spain): Earth and Planetary Science Letters, v. 553, 116636, 15 p., doi:10.1016/j.epsl.2020.116636.
Hosa, A., R. A. Wood, P. W. M. Corbett, R. S. de Souza, and E. Roemers, 2020, Modelling the impact of depositional and diagenetic processes on reservoir properties of the crystal-shrub limestones in the 'Pre-Salt' Barra Velha Formation, Santos Basin, Brazil: Marine and Petroleum Geology, v. 112, 104100, 10 p., doi:10.1016/j.marpetgeo.2019.104100.
Karner, G. D., and L. A. P. Gambôa, 2007, Timing and origin of the South Atlantic pre-salt sag basins and their capping evaporites, *in* B. C. Schreiber, S. Lugli, and M. Bąbel, eds., Evaporites through space and time: Geological Society, London, Special Publications 2007, v. 285, p. 15–35.
Lander, R. H., and S. E. Laubach, 2015, Insights into rates of fracture growth and sealing from a model for quartz cementation in fractured sandstones: GSA Bulletin, v. 127, no. 3–4, p. 516–538, doi:10.1130/B31092.1.
Lapponi, F., D. Hunt, and T. Dickson, 2019, Low and high temperature silica diagenesis in a giant pre-salt reservoir: BM-C-33, Campos Basin: Brazil: First European Association of Geoscientists and Engineers Workshop on Pre-Salt Reservoir: From Exploration to Production, Rio de Janeiro, Brazil, December 5–6, 2019, 4 p.
Laubach, S. E., 2003, Practical approaches to identifying sealed and open fractures: AAPG Bulletin, v. 87, no. 4, p. 561–579, doi:10.1306/11060201106.
Laubach, S. E., P. Eichhubl, P. Hargrove, M. A. Ellis, and J. N. Hooker, 2014, Fault core and damage zone fracture attributes vary along strike owing to interaction of fracture growth, quartz accumulation, and differing sandstone composition: Journal of Structural Geology, v. 68, Part A, p. 207–226, doi:10.1016/j.jsg.2014.08.007.
Laubach, S. E., P. Eichhubl, C. Hilgers, and R. H. Lander, 2010, Structural diagenesis: Journal of Structural Geology, v. 32, no. 12, p. 1866–1872, doi:10.1016/j.jsg.2010.10.001.
Laubach, S. E., R. H. Lander, L. J. Criscenti, L. M. Anovitz, J. L. Urai, R. M. Pollyea, J. N. Hooker, et al, 2019, The role of chemistry in fracture pattern development and opportunities to advance interpretations of geological materials: Reviews of Geophysics, v. 57, no. 3, p. 1065–1111, doi:10.1029/2019RG000671.
Lawson, M., J. Sitgreaves, T. Rasbury, K. Wooton, W. Esch, V. Marcon, S. Henares, et al., 2023, New age and lake chemistry constraints on the Aptian pre-salt carbonates of the central South Atlantic: GSA Bulletin, v. 135, no. 3–4, p. 595–607, doi:10.1130/B36378.1.
Leite, C. O. N., C. M. A. Silva, and L. F. De Ros, 2020, Depositional and diagenetic processes in the pre-salt rift section of a Santos Basin area, SE Brazil: Journal of Sedimentary Research, v. 90, no. 6, p. 584–608, doi:10.2110/jsr.2020.27.

Lima, B. E. M., 2020, Impacto da alteração hidrotermal na qualidade dos reservatórios carbonáticos do pré-sal no norte da bacia de campos, Ph.D. thesis, Universidade Federal do Rio Grande do Sul, Porto Alegre, Brazil, 313 p.

Lima, B. E. M., and L. F. de Ros, 2019, Deposition, diagenetic and hydrothermal processes in the Aptian Pre-Salt lacustrine carbonate reservoirs of the northern Campos Basin, offshore Brazil: Sedimentary Geology, v. 383, p. 55–81, doi:10.1016/j.sedgeo.2019.01.006.

Lima, B. E. M., L. R. Tedeschi, A. L. S. Pestilho, R. V. Santos, J. C. Vazquez, J. V. P. Guzzo, and L. F. De Ros, 2020, Deep-burial hydrothermal alteration of the Pre-Salt carbonate reservoirs from northern Campos Basin, offshore Brazil: Evidence from petrography, fluid inclusions, Sr, C and O isotopes: Marine and Petroleum Geology, v. 113, 104143, 25 p., doi:10.1016/j.marpetgeo.2019.104143.

Louback, V. S., S. de Castro Valente, C. N. de Almeida, J. Ross, and L. Borghi, 2023, Aptian flood basalts in Bacalhau oil and gas field: Petrogenesis and geodynamics of post-rift tholeiites in the pre-salt sequence of Santos Basin, Brazil: Contributions to Mineralogy and Petrology, v. 178, no. 3, 15, 25 p., doi:10.1007/s00410-023-01995-0.

Lüders, V., D. A. Banks, and P. Halbach, 2002, Extreme Cl/Br and δ^{37}Cl isotope fractionation in fluids of modern submarine hydrothermal systems: Mineralium Deposita, v. 37, no. 8, p. 765–771, doi:10.1007/s00126-002-0309-0.

Lüders, V., and S. Niedermann, 2010, Helium isotope composition of fluid inclusions hosted in massive sulfides from modern submarine hydrothermal systems: Economic Geology, v. 105, no. 2, p. 443–449, doi:10.2113/gsecongeo.105.2.443.

Lupinacci, W. M., T. Y. A. Fatah, M. C. do Carmo, A. F. M. Freire, and L. A. P. Gamboa, 2023, Controls of fracturing on porosity in pre-salt carbonate reservoirs: Energy Geoscience, v. 4, no. 2, p. 100146, doi:10.1016/j.engeos.2022.100146.

Magnavita, L., 2021, Arquitetura tectônica e cinemática do rifte do SE (com ênfase em Santos). Webinar Luciano Magnavita, accessed March 19, 2021, https://youtu.be/gLY9Ernt7zE.

Mejia, C., D. Roehl, J. Rueda, and F. Fonseca, 2022, Geomechanical effects of natural fractures on fluid flow in a pre-salt field: Journal of Natural Gas Science and Engineering, v. 107, 104772, 17 p., doi:10.1016/j.jngse.2022.104772.

Melani, L. H., 2019, Borehole based sedimentary cyclicity and structural analysis: Applications for reservoir characterization studies in the post- and presalt carbonates of Santos and Campos basins, SE Brazil, Ph.D. thesis, Universidade Estadual de Campinas, Campinas, Brazil, 104 p.

Mendes, L. D. C., M. Basso, J. V. Morales, G. F. Chinelatto, J. M. Blanco, U. M. Correia, J. P. Ponte, et al., 2024, The influence of major faults and fractures on the development of non-matrix porosity system in a pre-salt carbonate reservoir, Santos Basin – Brazil: Journal of Structural Geology, v. 189, 105271, 20 p., doi:10.1016/j.jsg.2024.105271.

Mendes, L. D. C., U. M. Correia, O. R. Cunha, F. M. Oliveira, and A. C. Vidal, 2022, Topological analysis of fault network in naturally fractured reservoirs: A case study from the pre-salt section of the Santos Basin, Brazil: Journal of Structural Geology, v. 159, 104597, 16 p., doi:10.1016/j.jsg.2022.104597.

Mercedes-Martín, R., C. Ayora, J. Tritlla, and M. Sánchez-Román, 2019, The hydrochemical evolution of alkaline volcanic lakes: A model to understand the South Atlantic pre-salt mineral assemblages: Earth-Science Reviews, v. 198, 102938, 19 p., doi:10.1016/j.earscirev.2019.102938.

Mimoun, J. G., and F. Fernández-Ibáñez, 2023, Carbonate excess permeability in pressure transient analysis: A catalog of diagnostic signatures from the Brazil Pre-Salt: Journal of Petroleum Science and Engineering, v. 220, 111173, 15 p., doi:10.1016/j.petrol.2022.111173.

Mizuno, T. A., A. M. P. Mizusaki, and R. Lykawka, 2018, Facies and paleoenvironments of the Coqueiros Formation (Lower Cretaceous, Campos Basin): A high frequency stratigraphic model to support pre-salt "coquinas" reservoir development in the Brazilian continental margin: Journal of South American Earth Sciences, v. 88, p. 107–117, doi:10.1016/j.jsames.2018.07.007.

Mizusaki, A. M. P., R. Petrini, P. Bellieni, P. Comin-Chiaramonti, J. Dias, A. De Min, and E. M. Piccirillo, 1992, Basalt magmatism along the passive continental margin of SE Brazil (Campos Basin): Contributions to Mineralogy and Petrology, v. 111, no. 2, p. 143–160, doi:10.1007/BF00348948.

Moreira, J. L. P., C. A. Esteves, J. J. G. Rodrigues, and C. S. D. Vasconcelos, 2005, Magmatismo, sedimentacao e estratigrafia da porcao norte da Bacia de Santos: Boletim de Geociencias da Petrobras, v. 14, p. 161–170.

Moreira, J. L. P., C. V. Madeira, J. A. Gil, and M. A. P. Machado, 2007, Bacia de Santos: Boletim de Geociencias da Petrobras, v. 15, no. 2, p. 531–549.

Moulin, M., D. Aslanian, and P. Unternehr, 2010, A new starting point for the South and Equatorial Atlantic Ocean: Earth-Science Reviews, v. 98, no. 1–2, p. 1–37, doi:10.1016/j.earscirev.2009.08.001.

Moura, J. A., 1972, Algumas especies e subespecies novas de ostracodes da bacia Reconcavo/Tucano: Boletim Tecnico da Petrobras, v. 15, p. 245–263.

Muniz, M. C., and D. W. J. Bosence, 2018, Lacustrine carbonate platforms: Facies, cycles, and tectonosedimentary models for the presalt Lagoa Feia Group (Lower Cretaceous), Campos Basin, Brazil: AAPG Bulletin, v. 102, no. 12, p. 2569–2597, doi:10.1306/0511181620617087.

Muñoz-López, D., D. Cruset, J. Vergés, I. Cantarero, A. Benedicto, X. Mangenot, R. Albert, A. Gerdes, A. Beranoaguirre, and A. Travé, 2022, Spatio-temporal variation of fluid flow behavior along a fold: The Bóixols-Sant Corneli anticline (Southern Pyrenees) from U–Pb dating and structural, petrographic and geochemical constraints: Marine and Petroleum Geology, v. 143, 105788, 22 p., doi:10.1016/j.marpetgeo.2022.105788.

Narr, W., D. S. Schechter, and L. B. Thompson, 2006, Naturally fractured reservoir characterization: Richardson, Texas, Society of Petroleum Engineers, 115 p.

Narr, W., and J. Suppe, 1991, Joint spacing in sedimentary rocks: Journal of Structural Geology, v. 13, no. 9, p. 1037–1048, doi:10.1016/0191-8141(91)90055-N.

Nelson, R., 2001, Geologic analysis of naturally fractured reservoirs: New York, Elsevier, 352 p.

Netto, P. R., M. Pozo, M. D. da Silva, M. E. B. Gomes, A. Mexias, C. W. Ramnani, Y. Parizek-Silva, L. Borghi, and A. D. M. Rios-Netto, 2022, Paleoenvironmental implications of authigenic magnesian clay formation sequences in the Barra Velha Formation (Santos Basin, Brazil): Minerals, v. 12, no. 2, 200, 20 p., doi:10.3390/min12020200.

Niedermann, S., W. Bach, and J. Erzinger, 1997, Noble gas evidence for a lower mantle component in MORBs from the southern East Pacific Rise: Decoupling of helium and neon isotope systematics: Geochimica et Cosmochimica Acta, v. 61, no. 13, p. 2697–2715, doi:10.1016/S0016-7037(97)00102-6.

Oden, M. I., E. U. Egeh, and E. A. Amah, 2015, The Ikom-Mamfe basin, Nigeria: A study of fracture and mineral vein lineament trends and Cretaceous deformations: Journal of African Earth Sciences, v. 101, p. 35–41, doi:10.1016/j.jafrearsci.2014.09.002.

Odling, N. E., P. Gillespie, B. Bourgine, C. Castaing, J. P. Chiles, N. P. Christensen, E. Fillion, et al., 1999, Variations in fracture system geometry and their implications for fluid flow in fractures hydrocarbon reservoirs: Petroleum Geoscience, v. 5, no. 4, p. 373–384, doi:10.1144/petgeo.5.4.373.

O'Neil, J. R., R. N. Clayton, and T. K. Mayeda, 1969, Oxygen isotope fractionation in divalent metal carbonates: The Journal of Chemical Physics, v. 51, no. 12, p. 5547–5558, doi:10.1063/1.1671982.

Ortega, O. J., R. A. Marrett, and S. E. Laubach, 2006, A scale-independent approach to fracture intensity and average spacing measurement: AAPG Bulletin, v. 90, no. 2, p. 193–208, doi:10.1306/08250505059.

Paton, C., J. Hellstrom, B. Paul, J. Woodhead, and J. Hergt, 2011, Iolite: Freeware for the visualisation and processing of mass spectrometric data: Journal of Analytical Atomic Spectrometry, v. 26, no. 12, p. 2508–2518, doi:10.1039/c1ja10172b.

Pedrinha, S., V. Artagão, T. P. Moreira, L. C. S. Freitas, E. Richter, and B. T. Santos, 2018, Reservoir geology aspects of Lula supergiant field, Santos Basin–Brazilian pre-Salt province (abs.): 2018 AAPG Annual Convention and Exhibition: Salt Lake City, Utah, May 20–23, 2018, accessed May 1, 2025, https://www.searchanddiscovery.com/abstracts/html/2018/ace2018/abstracts/2854470.html.

Pentecost, A., 2005, Travertine: Springer Science & Business Media, 460 p.

Pestilho, A. L., D. C. D. Filho, V. Lüders, I. O. Carmo, A. E. S. Dias, L. R. Tedeschi, B. R. B. M. Carvalho, E. T. Moraes, D. M. Ibanez, and G. Garcia, 2022, Evidence of deep-sourced volatiles in the diagenetic evolution of the Aptian carbonates of Santos Basin, Brazil: Pan-American Current Research on Fluid Inclusions, Edmonton, Alberta, Canada, September 1–3, 2022, p. 43–44.

Petit, J. P., C. A. Wibberley, and G. Ruiz, 1999, 'Crack–seal', slip: A new fault valve mechanism?: Journal of Structural Geology, v. 21, no. 8–9, p. 1199–1207, doi:10.1016/S0191-8141(99)00038-3.

Pietzsch, R., D. M. Oliveira, L. R. Tedeschi, J. V. Q. Neto, M. F. Figueiredo, J. C. Vazquez, and R. S. de Souza, 2018, Palaeohydrology of the Lower Cretaceous pre-salt lacustrine system, from rift to post-rift phase, Santos Basin, Brazil: Palaeogeography, Palaeoclimatology, Palaeoecology, v. 507, p. 60–80, doi:10.1016/j.palaeo.2018.06.043.

Pietzsch, R., L. R. Tedeschi, D. M. Oliveira, C. W. D. dos Anjos, J. C. Vazquez, and M. F. Figueiredo, 2020, Environmental conditions of deposition of the Lower Cretaceous lacustrine carbonates of the Barra Velha Formation, Santos Basin (Brazil), based on stable carbon and oxygen isotopes: A continental record of pCO_2 during the onset of the Oceanic Anoxic Event 1a (OAE 1a) interval?: Chemical Geology, v. 535, 119457, 23 p., doi:10.1016/j.chemgeo.2019.119457.

Pietzsch, R., N. J. Tosca, J. P. Gomes, S. Roest-Ellis, A. C. L. Sartorato, and S. N. Tonietto, 2022, The role of phosphate on non-skeletal carbonate production in a Cretaceous alkaline lake: Geochimica et Cosmochimica Acta, v. 317, p. 365–394, doi:10.1016/j.gca.2021.09.032.

Poropat, S. F., and J. P. Colin, 2012, Early Cretaceous ostracod biostratigraphy of eastern Brazil and western Africa: An overview: Gondwana Research, v. 22, no. 3–4, p. 772–798, doi:10.1016/j.gr.2012.06.002.

Ramsay, J. G., 1980, The crack–seal mechanism of rock deformation: Nature, v. 284, no. 5752, p. 135–139, doi:10.1038/284135a0.

Rangel, H. D., J. L. F. Oliveira, and J. M. Caixeta, 2007, Bacia de Jequitinhonha: Boletim de Geociencias da Petrobras, v. 15, p. 475–483.

Regali, M. S. P., N. Uesugui, and A. S. Santos, 1974, Palinologia dos sedimentos Mesocenozoicos do Brasil (I): Boletim Técnico da Petrobras, v. 17, p. 177–191.

Renaut, R. W., R. B. Owen, B. Jones, J. J. Tiercelin, C. Tarits, J. K. Ego, and K. O. Konhauser, 2013, Impact of lake-level changes on the formation of thermogene travertine in continental rifts: Evidence from Lake Bogoria, Kenya Rift Valley: Sedimentology, v. 60, no. 2, p. 428–468, doi:10.1111/j.1365-3091.2012.01347.x.

Révész, K. M., and J. M. Landwehr, 2002, $\delta^{13}C$ and $\delta^{18}O$ isotopic composition of $CaCO_3$ measured by continuous flow isotope ratio mass spectrometry: Statistical evaluation and verification by application to Devils Hole Core DH-11 calcite: Rapid Communications in Mass Spectrometry, v. 16, no. 22, p. 2102–2114, doi:10.1002/rcm.833.

Richter, D. K., R. D. Neuser, J. Schreuer, H. Gies, and A. Immenhauser, 2011, Radiaxial-fibrous calcites: A new look at an old problem: Sedimentary Geology, v. 239, no. 1–2, p. 23–36, doi:10.1016/j.sedgeo.2011.06.003.

Rigoti, C. A., 2015, Evolução tectônica da Bacia de Santos com ênfase na geometria crustal: Interpretação integrada

de dados de sísmica de reflexão e refração, gravimetria e magnetometria, Master's dissertation, Universidade do Estado do Rio de Janeiro, Rio de Janeiro, Brazil, 135 p.

Roberts, N. M., K. Drost, M. S. Horstwood, D. J. Condon, D. Chew, H. Drake, A. E. Milodowski, et al., 2020, Laser ablation inductively coupled plasma mass spectrometry (LA-ICP-MS) U–Pb carbonate geochronology: Strategies, progress, and limitations: Geochronology, v. 2, no. 1, p. 33–61, doi:10.5194/gchron-2-33-2020.

Roberts, N. M., and R. E. Holdsworth, 2022, Timescales of faulting through calcite geochronology: A review: Journal of Structural Geology, v. 158, 104578, 12 p., doi:10.1016/j.jsg.2022.104578.

Roberts, N. M., E. T. Rasbury, R. R. Parrish, C. J. Smith, M. S. Horstwood, and D. J. Condon, 2017, A calcite reference material for LA-ICP-MS U-Pb geochronology: Geochemistry, Geophysics, Geosystems, v. 18, no. 7, p. 2807–2814, doi:10.1002/2016GC006784.

Rochelle-Bates, N., N. M. W. Roberts, I. Sharp, U. Freitag, K. Verwer, A. Halton, E. Fiordalisi, et al., 2021, Geochronology of volcanically associated hydrocarbon charge in the pre-salt carbonates of the Namibe Basin, Angola: Geology, v. 49, no. 3, p. 335–340, doi:10.1130/G48019.1.

Rochelle-Bates, N., R. Wood, S. Schröder, and N. M. Roberts, 2022, In situ U–Pb geochronology of Pre-Salt carbonates reveals links between diagenesis and regional tectonics: Terra Nova, v. 34, no. 4, p. 271–277, doi:10.1111/ter.12586.

Rodovalho, N., R. C. Gontijo, C. F. Santos, and P. d. S. Milhomem, 2007, Bacia de Cumuruxatiba: Boletim de Geociencias da Petrobras, v. 15, p. 485–491.

Rodríguez-Berriguete, Á., P. F. Dal' Bo, B. Valle, and L. Borghi, 2022, When distinction matters: Carbonate shrubs from the Aptian Barra Velha Formation of Brazilian's Pre-salt: Sedimentary Geology, v. 440, 106236, 15 p., doi:10.1016/j.sedgeo.2022.106236.

Roedder, E., 1984, Fluid inclusions: Mineralogical Society of America Reviews in Mineralogy 12, 646 p.

Sabato Ceraldi, T., and D. Green, 2017, Evolution of the South Atlantic lacustrine deposits in response to Early Cretaceous rifting, subsidence and lake hydrology, *in* T. Sabato Ceraldi, R. A. Hodgkinson, and G. Backe, eds., Petroleum geoscience of the West Africa margin: Geological Society, London, Special Publications 2017, v. 438, p. 77–98.

Sanjines, A. E. S., M. C. Viviers, D. S. Costa, G. D. S. dos Anjos Zerfass, G. Beurlen, and O. Strohschoen, Jr., 2022, Planktonic foraminifera from the Aptian section of the Southeastern Brazilian Atlantic margin: Cretaceous Research, v. 134, 105141, 16 p., doi:10.1016/j.cretres.2022.105141.

Sartorato, A. C. L., S. N. Tonietto, and E. Pereira, 2020, Silicification and dissolution features in the Brazilian Pre-Salt Barra Velha Formation: Impacts in the reservoir quality and insights for 3D geological modeling: Rio Oil and Gas Expo and Conference, Rio de Janeiro, Brazil, September 21–24, 2020, 2 p., doi:10.48072/2525-7579.rog.2020.068.

Savastano, V. L. M., R. da Silva Schmitt, M. N. C. de Araújo, and L. C. Inocêncio, 2017, Rift brittle deformation of SE-Brazilian continental margin: Kinematic analysis of onshore structures relative to the transfer and accommodation zones of southern Campos Basin: Journal of Structural Geology, v. 94, p. 136–153, doi:10.1016/j.jsg.2016.11.012.

Shukla, M. K., and A. Sharma, 2018, A brief review on breccia: It's contrasting origin and diagnostic signatures: Solid Earth Sciences, v. 3, no. 2, p. 50–59, doi:10.1016/j.sesci.2018.03.001.

Silva, O. B., J. M. Caixeta, P. d. S. Milhomem, and M. D. Kosin, 2007, Bacia do Reconcavo. Boletim de Geociencias da Petrobras, v. 15, p. 423–431.

Silva, V., A. Moliterno, C. H. Araujo, F. Pimentel, J. R. Melo, C. Falcao, and T. Pessoa, 2021, Buzios drainage strategy: A combination of reservoir characterization, risks mitigation and unique contract features: Offshore Technology Conference, Virtual and Houston, Texas, August 16–19, 2021, OTC-31170-MS, 20 p., doi:10.4043/31170-MS.

Simo, T., J. Sitgreaves, E. Smith, U. Bayram, and J. Stewart, 2019, Styles of pre-salt carbonate platforms, Brazil Santos Basin: AAPG Annual Convention and Exhibition, San Antonio, Texas, May 19–22, 2019, accessed May 1, 2025, https://www.searchanddiscovery.com/abstracts/html/2019/ace2019/abstracts/1645.html.

Souza, R. S., L. M. Arienti, S. M. Viana, L. C. Falcão, M. A. Cuglieri, R. P. Silva Filho, C. O. Leite, et al., 2018, Petrology of the hydrothermal and evaporitic continental Cretaceous (Aptian) pre-salt carbonates and associated rocks, South Atlantic Santos Basin, offshore Brazil: AAPG Annual Convention and Exhibition, Salt Lake City, Utah, May 20–23, 2018, accessed June 7, 2023, https://www.searchanddiscovery.com/abstracts/html/2018/ace2018/abstracts/2835691.html.

Spötl, C., and T. W. Vennemann, 2003, Continuous-flow isotope ratio mass spectrometric analysis of carbonate minerals: Rapid Communications in Mass Spectrometry, v. 17, no. 9, p. 1004–1006, doi:10.1002/rcm.1010.

Strugale, M., and J. Cartwright, 2022, Tectono-stratigraphic evolution of the rift and post-rift systems in the northern Campos Basin, offshore Brazil: Basin Research, v. 34, no. 5, p. 1655–1687, doi:10.1111/bre.12674.

Strugale, M., R. da Silva Schmitt, and J. Cartwright, 2021, Basement geology and its controls on the nucleation and growth of rift faults in the northern Campos Basin, offshore Brazil: Basin Research, v. 33, no. 3, p. 1906–1933, doi:10.1111/bre.12540.

Strugale, M., B. E. M. Lima, C. Day, J. Omma, J. Rushton, J. P. R. Olivito, J. Bouch, L. Robb, N. Roberts, and J. Cartwright, 2024, Diagenetic products, settings and evolution of the pre-Salt succession in the northern Campos Basin, Brazil, *in* J. Garland, A. J. Barnett, T. P. Burchette, and V. P. Wright, eds., Carbonate reservoirs: Applying current knowledge to future energy needs: Geological Society, London, Special Publications 2024, v. 548, SP548-2021.

Szatmari, P., and E. J. Milani, 2016, Tectonic control of the oil-rich large igneous-carbonate-salt province of the South Atlantic rift: Marine and Petroleum Geology, v. 77, p. 567–596, doi:10.1016/j.marpetgeo.2016.06.004.

Tanaka, A. P. B., J. P. G. Borges, G. C. de Matos, M. T. R. Campos, B. M. Cunha, R. B. de Souza, J. N. M. Caldeira, T. A. S. Oliveira, D. R. Marçon, and A. P. M. Lima, 2022, Fault-related fracture modeling in a pre-salt lacustrine carbonate reservoir from Santos Basin, offshore Brazil: Predicting preferential fluid flow paths using 3D geological and flow simulation models: Marine and Petroleum Geology, v. 135, 105392, 7 p., doi:10.1016/j.marpetgeo.2021.105392.

Teboul, P. A., C. Durlet, J. P. Girard, L. Dubois, G. San Miguel, A. Virgone, E. C. Gaucher, and G. Camoin, 2019, Diversity and origin of quartz cements in continental carbonates: Example from the Lower Cretaceous rift deposits of the South Atlantic margin: Applied Geochemistry, v. 100, p. 22–41, doi:10.1016/j.apgeochem.2018.10.019.

Tedeschi, L. R., H. C. Jenkyns, S. A. Robinson, A. E. Sanjinés, M. C. Viviers, C. M. Quintaes, and J. C. Vazquez, 2017, New age constraints on Aptian evaporites and carbonates from the South Atlantic: Implications for Oceanic Anoxic Event 1a: Geology, v. 45, no. 6, p. 543–546, doi:10.1130/G38886.1.

Terra, G. J. S., A. R. Spadini, A. B. Franca, C. L. Sombra, E. E. Zambonato, L. C. S. Juschacks, L. M. Arienti, et al., 2010, Classificação de rochas carbonáticas aplicável às bacias sedimentares brasileiras: Boletim de Geociências da Petrobras, v. 18, p. 9–29, doi:10.70369/1vwy1g06.

Terra, S. A., A. Ribeiro, M. V. Mafia, F. Nepomuceno, D. R. L. da Silva, and L. Borghi, 2024, Deformational structures in the lower Barra Velha formation, Aptian, Atapu field, Santos Basin: Journal of South American Earth Sciences, v. 136, 104816, doi:10.1016/j.jsames.2024.104816.

Thomaz Filho, A., A. M. P. Mizusaki, and L. Antonioli, 2008, Magmatismo nas bacias sedimentares brasileiras e sua influência na geologia do petróleo: Revista Brasileira de Geociências, v. 38, no. 2, p. 128–137, doi:10.25249/0375-7536.2008382S128137.

Torgersen, T., and W. J. Jenkins, 1982, Helium isotopes in geothermal systems: Iceland, The Geysers, Raft River and Steamboat Springs: Geochimica et Cosmochimica Acta, v. 46, no. 5, p. 739–748, doi:10.1016/0016-7037(82)90025-4.

Tosca, N. J., and V. P. Wright, 2018, Diagenetic pathways linked to labile Mg-clays in lacustrine carbonate reservoirs: A model for the origin of secondary porosity in the Cretaceous pre-salt Barra Velha Formation, offshore Brazil, *in* P. J. Armitage, A. R. Butcher, J. M. Churchill, A. E. Csoma, C. Hollis, R. H. Lander, J. E. Omma, and R. H. Worden, eds., Reservoir quality of clastic and carbonate rocks: Analysis, modelling and prediction: Geological Society, London, Special Publications 2018, v. 435, p. 33–46.

Tritlla, J., M. Esteban, R. Loma, A. Mattos, V. Sánchez, C. Boix, and G. Levresse, 2018, Carbonates that are no more: Silicified pre-salt oil reservoirs in Campos Basin (Brazil): AAPG Annual Convention and Exhibition, Salt Lake City, Utah, May 20–23, 2018, accessed May 1, 2025, https://www.searchanddiscovery.com/abstracts/html/2018/ace2018/abstracts/2841018.html.

Tucker, M. E., 1991, Sequence stratigraphy of carbonate-evaporite basins: Models and application to the Upper Permian (Zechstein) of northeast England and adjoining North Sea: Journal of the Geological Society, v. 148, no. 6, p. 1019–1036, doi:10.1144/gsjgs.148.6.1019.

Ukar, E., V. Baqués, S. E. Laubach, and R. Marrett, 2020, The nature and origins of decameter-scale porosity in Ordovician carbonate rocks, Halahatang oilfield, Tarim Basin, China: Journal of the Geological Society, v. 177, no. 5, p. 1074–1091, doi:10.1144/jgs2019-156.

Vermeesch, P., 2018, IsoplotR: A free and open toolbox for geochronology: Geoscience Frontiers, v. 9, no. 5, p. 1479–1493, doi:10.1016/j.gsf.2018.04.001.

Vieira de Luca, P. H. V., H. Matias, J. Carballo, D. Sineva, G. A. Pimentel, J. Tritlla, M. Esteban, et al., 2017, Breaking barriers and paradigms in presalt exploration: The Pão de Açúcar discovery (offshore Brazil), *in* R. K. Merrill and C. A. Sternbach, eds., Giant fields of the decade 2000–2010: AAPG Memoir 113, p. 177–194.

Vieira de Luca, P. V., A. Waldum, A. S. Chandler, D. Hunt, O. P. Wennberg, G. McQuenn, D. Hulme, et al., 2019, Porosity characterization of complex silicified carbonates reservoirs of BM-C-33: First European Association of Geoscientists and Engineers Workshop on Pre-Salt Reservoir: From Exploration to Production, Rio de Janeiro, Brazil, December 5–6, 2019, 5 p.

Vital, J. C. S., M. V. B. Ade, R. Morelatto, and W. M. Lupinacci, 2023, Compartmentalization and stratigraphic-structural trapping in pre-salt carbonate reservoirs of the Santos Basin: A case study in the Iara complex: Marine and Petroleum Geology, v. 151, 106163, 28 p., doi:10.1016/j.marpetgeo.2023.106163.

Wennberg, O. P., G. Casini, S. Jonoud, and D. C. Peacock, 2016, The characteristics of open fractures in carbonate reservoirs and their impact on fluid flow: A discussion: Petroleum Geoscience, v. 22, no. 1, p. 91–104, doi:10.1144/petgeo2015-003.

Wennberg, O. P., G. McQueen, P. V. de Luca, F. Lapponi, D. Hunt, A. S. Chandler, A. Waldum, G. Nery Camargo, E. Castro, and L. Loures, 2021, Open fractures in pre-salt silicified carbonate reservoirs in block BM-C-33, the Outer Campos Basin, offshore Brazil: Petroleum Geoscience, v. 27, no. 4, petgeo 2020–125, 16 p., doi:10.1144/petgeo2020-125.

Wennberg, O. P., F. D. O. Ramalho, M. V. Mafia, F. Lapponi, A. S. Chandler, L. G. Cartesio, and D. W. Hunt, 2023, The characteristics of natural open fractures in acoustic borehole image logs from the pre-salt Barra Velha Formation, Santos Basin, Brazil: Journal of Structural Geology, v. 167, 104794, 20 p., doi:10.1016/j.jsg.2023.104794.

Williams, R. T., and Å. Fagereng, 2022, The role of quartz cementation in the seismic cycle: A critical review: Reviews of Geophysics, v. 60, no. 1, e2021RG000768, 35 p., doi:10.1029/2021RG000768.

Williams, R. T., J. R. Farver, C. M. Onasch, and D. F. Winslow, 2015, An experimental investigation of the role of microfracture surfaces in controlling quartz precipitation

rate: Applications to fault zone diagenesis: Journal of Structural Geology, v. 74, p. 24–30, doi:10.1016/j.jsg.2015.02.011.

Winter, W. R., R. J. Jahnert, and A. B. França, 2007, Bacia de Campos. Boletim de Geociências da Petrobras, v. 15, no. 2, p. 511–529.

Wright, V. P., 2022, The mantle, CO_2 and the giant Aptian chemogenic lacustrine carbonate factory of the South Atlantic: Some carbonates are made, not born: Sedimentology, v. 69, no. 1, p. 47–73, doi:10.1111/sed.12835.

Wright, V. P., and A. J. Barnett, 2015, An abiotic model for the development of textures in some South Atlantic early Cretaceous lacustrine carbonates, *in* D. W. J. Bosence, K. A. Gibbons, D. P. Le Heron, W. A. Morgan, T. Pritchard, and B. A. Vining, eds., Microbial carbonates in space and time: Implications for global exploration and production: Geological Society, London, Special Publications 2015, v. 418, p. 209–219, doi:10.1144/SP418.3.

Zalán, P. V., M. D. C. G. Severino, C. A. Rigoti, L. P. Magnavita, J. A. B. Oliveira, and A. R. Vianna, 2011, An entirely new 3D-view of the crustal and mantle structure of a South Atlantic passive margin–Santos, Campos and Espírito Santo Basins: Brazil (abs.): AAPG Annual Conference and Exhibition: Making the Next Giant Leap in Geosciences, Houston, Texas, April 10–13, 2011, accessed June 7, 2023, https://www.searchanddiscovery.com/abstracts/html/2011/annual/abstracts/Zalan.html.

Zeller, M., D. W. Hunt, A. S. Chandler, L. E. Gomis-Cartesio, C. Aizprua, and O. P. Wennberg, 2022, En-Échelon fault-controlled ridge mounds in the Barra Velha Formation–Quantitative conceptual analogs for field development: Third European Association of Geoscientists and Engineers Conference on Pre-Salt Reservoirs, Rio de Janeiro, Brazil, November 23–25, 2022, 6 p., doi:10.3997/2214-4609.202288003.

Zucchetti, M., J. Costa, and I. de Oliveira Carmo, 2015, Vulcanismo subaquoso nas bacias marginais brasileiras, Simpósio de Vulcanismo e Ambientes Associados: Sao Paulo, Brazil, August 2–5, 2015.